Investigations towards the development of a novel multimodal fibre optic sensor for oil and gas applications.

JOHNY, J.

2019

Investigations towards the development of a novel multimodal fibre optic sensor for oil and gas applications

Jincy Johny

A thesis submitted in partial fulfilment of the requirements for the award of

Doctor of Philosophy

at

School of Engineering
Robert Gordon University
Aberdeen, UK

August 2019

Supervised by: Dr Radhakrishna Prabhu
Dr Wai Keung Fung

Acknowledgement

Firstly, I would like to express my sincere gratitude to my principal supervisor Dr. Radhakrishna Prabhu for his continuous support throughout my PhD journey and for his patience and motivation which helped me sail through my difficult times. His guidance and immense knowledge greatly helped me in developing my research and experimental skills.

I am also thankful to my second supervisor, Dr. Wai Keung Fung for all his support, insightful comments and encouragement.

Besides my supervisors, I would like to thank senior researcher, Dr. Kaushalkumar Bhavsar for his positive advices and suggestions. My sincere appreciation also goes to Ms. Jade Summer for her support with the theoretical investigations of the mechanical cantilever systems. I take this opportunity to thank Mr. Vivek Viswambharan as well, for his support during my initial days in Robert Gordon University.

Nobody has been more important to me in the journey of this research than my family. I would like to specially thank my beloved husband Charles, my little daughter Cailyn, my parents and my in-laws, whose love and support are with me in whatever I pursue.

Last but not the least, I am thankful to Lord Jesus and Mother Mary for the divine blessing and guidance where ever I go and whatever I do.

List of Publications

Journal Publications

- **Johny J**, Prabhu R, Fung WK. Investigation of structural parameter dependence of confinement losses in PCF–FBG sensor for oil and gas sensing applications. Optical and Quantum Electronics. 2016 Apr 1;48(4):252.
- **Johny J**, Prabhu R, Fung WK. Numerical Investigation of Nanostructured Silica PCFs for Sensing Applications. JOM. 2017 May 3:1-6.

Conference Publications

- **Johny J**, Prabhu R, Fung WK, Watson J. Investigation of positioning of FBG sensors for smart monitoring of oil and gas subsea structures. In OCEANS 2016-Shanghai 2016 Apr 10 (pp. 1-4). IEEE.
- **Johny J**, Prabhu R, Fung WK. Computational study of nanostructured composite materials for photonic crystal fibre sensors. In IOP Conference Series: Materials Science and Engineering 2017 May (Vol. 195, No. 1, p. 012012). IOP Publishing.
- **Johny J**, Summers J, Bhavsar K, Joseph GP, Fung WK, Prabhu R. Theoretical investigation of positional influence of FBG sensors for structural health monitoring of offshore structures. In OCEANS 2017-Aberdeen 2017 Jun 19 (pp. 1-5). IEEE.
- **Johny J**, Smith T, Bhavsar K, Prabhu R. Design of optical fibre based highly sensitive acoustic sensor for underwater applications. In OCEANS 2017-Aberdeen 2017 Jun 19 (pp. 1-5). IEEE.
- **Johny J**, Bhavsar K, Officer S, Adams M, Prabhu R. Waveguide-based machine-readable fluorescence security feature for border control and security applications. In Counterterrorism, Crime Fighting, Forensics, and Surveillance Technologies II 2018 Oct 8 (Vol. 10802, p. 1080209). International Society for Optics and Photonics.

Conference/Symposium/Workshop

- **Johny J**, Prabhu R, Fung WK. "Preliminary Analysis of Fibre Bragg Grating Sensor for Oil and Gas Applications," IDEAS Poster Symposium, Robert Gordon University, Aberdeen, UK, December 2014 (Poster).
- **Johny J**, Prabhu R, Fung WK. Investigation of Confinement Losses in Photonic Crystal Fibre. Optical Wave and Waveguide Theory and Numerical Modelling (OWTNM 2015), City University London, UK, April 2015 (Poster).
- **Johny J**, Prabhu R, Fung WK. Investigations on the Electro-Optic Tuning Characteristics of Liquid Crystal PCF for Sensing Applications. 2019 Scotland and North of England Electrochemistry Symposium, University of Edinburgh, UK, April 2019 (Poster).

Papers in preparation

- **Johny J**, Officer S, Fung WK, Prabhu R. **Fluorescence lifetime assisted enhanced security feature in travel documents for border control and security applications**. Counterterrorism, Crime Fighting, Forensics, and Surveillance Technologies III conference, SPIE Security + Defence International Symposium, Strasbourg, France, 9 - 12 September 2019 (Paper Accepted).
- **Johny J**, Prabhu R, Fung WK. Investigations on rare earth doped nanostructured silica composite materials for fluorescence-based fiber optic sensors. Journal of Materials – JOM 2019.

Other Publications

- Bhavsar K, **Johny J** and Prabhu R, Optical Fibre-Based Sensors for MRI-Guided Medical Applications, EPSRC UK Image-Guided Therapies Network+ Meeting, Edinburgh, UK, Nov 9, 2016 (Poster).
- Bhavsar K, Viswambaran V, **Johny J**, Kailasnath M, Melzer A, Prabhu R. Development of a ring cavity-based fibre optic sensor for MR-compatible medical sensing applications. In IOP Conference Series: Materials Science and Engineering 2019 Mar (Vol. 499, No. 1, p. 012013). IOP publishing.
- Bhavsar K, **Johny J**, Prabhu R and Melzer A, Design of a multifunctional microstructured optical fibre-based sensor for minimally invasive medical

applications, IOP optics in clinical practice IV, Nottingham, UK, Mar 22, 2018 (Poster).

- Jesna GK, Joseph O, **Johny J**, Prabhu R, Praveen BM, Chandrappa KG. Electrochemical Generation of Zn_2SnO_4 Photocatalyst for Degradation of Methylene Blue Effluent. 2019 Scotland and North of England Electrochemistry Symposium, University of Edinburgh, UK, April 2019 (Poster).
- Joseph O, **Johny J**, Devalla S, Radhakrishnan P, Prabhu R. Photonic efficiency enhancement of photocatalytic reactors through periodic illumination of TiO2 nanopowders. International Conference on Advanced Materials - ICAM 2019, Nirmalagiri College, Kannur, India, 12^{th} -14^{th} June 2019 (Paper).
- Prabhu R, **Johny J**, Bhavsar K, Amos S. Optical sensors and sensory materials for applications in Medical to Environmental monitoring. International Conference on Advanced Materials - ICAM 2019, Nirmalagiri College, Kannur, India, 12^{th} -14^{th} June 2019.

Abstract

Oil and gas (O&G) explorations are moving into deeper zones of earth, causing serious safety concerns. Hence, sensing of critical multiple parameters like high pressure, high temperature (HPHT), chemicals, etc., are required at longer distances. Traditional electrical sensors operate less effectively under these extreme environmental conditions and are susceptible to electromagnetic interference (EMI). Compared to electrical sensors, fibre optic sensors offer several advantages like immunity to EMI, electrical isolation, ability to operate in harsh environmental conditions and freedom from corrosion. Existing optical fibre sensors in the O&G industry, based on step index single mode fibres (SMF) offers limited performance, as it operates within a narrow wavelength window. A novel, photonic crystal fibre (PCF) based, multimodal sensor configuration utilising multi-wavelength approach is proposed for the first time for the O&G applications. This thesis reports computational and experimental investigations on the new multimodal sensing methodology, integrating both optical phase-change and spectral-change based approaches, needed for multi-parameter sensing. It includes investigations to improve the signal-to-noise ratio (SNR) by enhancing the signal intensity attained through structural, material and positional optimisations of the sensors.

Waveguide related, computational investigations on PCF were carried out on different fibre optic core-cladding structures, material infiltrations and material doping to improve the signal intensity from the multimodal sensors for better SNR. COMSOL Multiphysics simulations indicated that structural and material modifications of the PCF have significant effects on light propagation characteristics. Modifying the geometrical parameters and microstructuring the fibre core and cladding improved the propagation characteristics of the PCF. Studies carried out on liquid crystal PCF (LCPCF) identified its enhanced mode confinement characteristics and wavelength tenability (from visible to near infrared) features which can be utilised for multi-wavelength applications. Enhancing core refractive index of the PCF improved the electric field confinements and thereby the signal intensity. Doping rare earth elements into the PCF core increases its refractive index and also provides additional spectroscopic features (photoluminescence and Raman), leading to a scope for multi-point, multimodal sensors.

Investigations were carried out on PCF-FBG (Fibre Bragg grating) hybrid configuration, analysing their capabilities for optical phase-change based, multi-point, multi-parameter sensing. Computational investigations were carried out using MATLAB software, to study the effect of various fibre grating parameters. These studies helped in improving understanding of the FBG reflectivity-bandwidth characteristics, for tuning the number of sensors that can be accommodated within the same sensing fibre and enhancing the reflected signal for improved SNR. A new approach of FBG sensor positioning has been experimentally evaluated, to improve its strain sensitivity for structural health monitoring (SHM) of O&G structures. Further, experimental investigations were carried out on FBGs for sensing multiple parameters like temperature, strain (both tensile and compressive) and acoustic signals.

Various spectroscopic investigations were carried out to identify the scope of rare earth doping within the PCF for photoluminescence and Raman spectroscopy based multimodal sensors. Rare earth doped glasses (Tb, Dy, Yb, Er, Ce and Ho) were developed using melt-quench approach and excitation- photoluminescence emission studies were carried out. The studies identified that photoluminescence signal intensity increases with rare earth concentration upto an optimum value and it can be further improved by tuning the excitation source characteristics. Photoluminescence based temperature studies were carried out using the rare earth doped glasses to identify their suitability for O&G high temperature conditions. Raman spectroscopic investigations were carried out on rare earth (Tb) doped glasses developed using both melt-quench and sol-gel based approaches. Effect of 785 nm laser excitation on Raman signatures and suitability of rare earth doped materials for fibre-based Raman distributed temperature sensing (DTS) were studied.

Finally, a novel multimodal fibre optic sensor configuration consisting of rare earth doped photonic crystal fibre integrating Bragg gratings, operating in multiple wavelength regimes in a multiplexed fashion is proposed for the O&G applications. The integrated sensor combination expected to overcome the limitations of existing sensors with regards to SNR, sensing range and multimodal sensing capability.

Table of Contents

List of Figures

List of Tables

List of Abbreviations

Abbreviation	Description
AI	Artificial Intelligence
BSG	Borosilicate Glass
Ce	Cerium
CMN	Common Mode Noises
dB	Decibels
DTS	Distributed Temperature Sensing
Dy	Dysprosium
EDXA	Energy Dispersive X-Ray Analysis
EMI	Electromagnetic Interference
Er	Erbium
FBG	Fibre Bragg Grating
FEM	Finite Element Method
FSM	Fundamental Space Filling Mode
Ho	Holmium
HPHT	High Pressure High Temperature
HSE	Health, Safety and Environment
HSN	Hsu- Nielsen
IR	Infrared
LCPCF	Liquid Crystal PCF
MFD	Mode Field Diameter

MIR	mid-IR
MM	Multi-Mode
M-TIR	Modified Total Internal Reflection
Nd	Neodymium
NIR	Near Infrared
O&G	Oil and Gas
OFDR	Optical Frequency Domain Reflectometry
ORL	Optical Return Loss
OSA	Optical Spectrum Analysers
OTDR	Optical Time Domain Reflectometry
PBG	Photonic Bandgap
PCF	Photonic Crystal Fibres
PDE	Partial Differential Equations
PID	Proportional Integral Derivative
PLB	Pencil Lead Break
PML	Perfectly Matched Layer
RIN	Relative Intensity Noise
SEM	Scanning Electron Microscopy
SGG	Sol-Gel Glass
SM	Single Mode
SMF	Single Mode Fibre
SNR	Signal to Noise Ratio
Tb	Terbium

TDM	Time-Division Multiplexing
UV	Ultraviolet
VIS	Visible
Yb	Ytterbium
ZBSG	Zinc Borosilicate Glass

Nomenclatures

Symbol	Description
L_c	Confinement or Leakage Loss
$\mathrm{n_{eff}}$	Effective Refractive Index
λ	Propagating Wavelength
$\mathrm{A_{eff}}$	Effective Mode Area
$\mathrm{E(x,y)}$	Optical Mode Field Distribution
k_n	Correction Factor
W	Spot Size
E	Electric Field
H	Magnetic Field
D	Electric Flux Densities
B	Magnetic Flux Densities
J	Current Density
ρ	Charge Density
β	Propagation Constant
θ_c	Critical Angle
$\mathrm{n_1}$	Core Refractive Index
$\mathrm{n_2}$	Cladding Refractive Index
k_0	Free Space Wave Number
Λ	Hole Spacing
d	Diameter

v	Fringe Visibility
λ_b	Bragg Reflected Wavelength
Λ_g	Period of the Grating
R	Amplitude of Forward Propagating Mode
S	Amplitude of Counter Propagating Mode
δ'	Tuning Parameter
σ	DC (Demi Coupling) Coefficient
k	AC (Associated Coupling) Coefficient
λ_d	Design Wavelength of FBG
$d\lambda_d/dz$	Rate of Change of Design Wavelength with Respect to Grating Position
Δn_{eff}	Change in Effective Refractive Index
i	Transfer Matrix
Δz	Length of ith Uniform Section
$\hat{\sigma}$	Local Values in the ith Section
Z	Position of the Grating
L_g	Grating Length
a_{eff}	Apodization Parameter
α	Raised-Cosine Parameter or Roll-off Factor
N	Number of Gratings
ΔT	Change in Temperature
ρ_e	Photo-Elastic Coefficient
$\Delta\varepsilon$	Variation in Strain Value

F	Axial Force
A	Cross Sectional Area of the Cantilever Beam
ε	Strain
L	Original Length of the Cantilever Beam
E	Young's Modulus
I	Second Moment of Area
m	Rectangular Cross-Sectional Area
b	Breadth of Rectangular Cross-Sectional Area
h	Height of Rectangular Cross-Sectional Area
δ	Deflection
F	Applied Force
$\bar{\nu}$	Raman Shift
T_i	i^{th} Time Window
RE_n	n^{th} Rare Earth Element
λ_n	Reflected Wavelength from n^{th} FBG
T	Time period

1. INTRODUCTION

1.1 Background and Motivations

Sensors and sensing data are vital elements in the oil and gas (O&G) industry. In recent years, O&G exploration and production has been moving into unconventional depths (more than 3 km) in order to meet the growing demand for energy [1]. This results in harsh and extreme operating conditions, which is reflected by critical parameters like temperature, pressure, strain, etc. Therefore, reliable sensors which are able to continuously monitor current down-hole conditions have become very important in managing O&G reservoirs and wells [2]. For efficient O&G resource management and enhanced oil and gas recovery, real-time and dynamic monitoring technologies are required [3-4]. In order to satisfy this need, multi-point or distributed and multimodal simultaneous measurements will be advantageous for drilling and O&G production monitoring.

Exploration and production process monitoring helps to prevent or detect health and safety issues and to significantly enhance O&G production [5]. Detecting and forecasting the conditions of the well at earlier stages have considerable impact on Health, Safety and Environment (HSE), risk management, well control and cost control strategies [6]. It enables the oil well technicians and managers to take correct decisions in a timely manner [7]. Continuous sensing and monitoring of unstable parameters like high temperature, pressure, strain etc., are required in the O&G sector in order to protect and safeguard their valuable assets operating in the harshest and most challenging environments.

Current O&G sensing techniques are mainly based on electrical sensors, which have many constraints when used in adverse environmental conditions [8]. These electrical sensors offer limited performance down-hole and are unreliable for real-time remote monitoring and control. Unfortunately, O&G reservoirs exhibit some of the harshest and least accessible environments on earth [9-10]. Increasing exploration depth results in High Pressure High Temperature (HPHT) field conditions., which corresponds to temperatures above 205 °C /400 °F and pressures more than 138 MPa/ 20,000 psi [11-12]. In such hostile habitat, conventional sensors either experience failure or they operate poorly. This occurs mainly due to their inability to withstand high temperature and pressure, as well as corrosive and erosive environmental conditions, found within the oil wells. Other limitations of traditional electrical gauges include limited sensing range, single point sensing capability and their inability to give continuous monitoring which make them unsuitable for oil well real-time monitoring applications. In addition, their poor Signal to Noise Ratio (SNR) due to electromagnetic interference (EMI) and their considerable size makes them highly undesirable for in-well applications [13]. On this account, improved technologies are to be developed to retrieve well information, in order to safely maximize oil productivity and reduce exploration and production cost, especially in present situation of reduced crude oil prices.

Fibre-optic sensing technology can overcome the aforementioned limitations of their electrical counterparts, mainly due to their small size, electrical isolation, corrosion resistance, immunity to EMI and capability to operate in extreme environmental conditions [14-15]. The small size of fibre-optic sensors facilitates them to be safely employed over longer distances with little or no future maintenance [16]. Moreover, they have reduced risk of failure when

exposed to water or other reservoir and pipeline fluids and also, they do not have any electrical power requirements at the sensor head [17]. Another important advantage of fibre sensor is that, the same optical fibre can handle dual functions. It can act as the sensing element for physical parameter measurement as well as the transmission medium for the sensed signal. This feature helps in the monitoring and sensing of different O&G critical parameters from remote locations [18]. Furthermore, by exploiting the wavelength multiplexing capability of optical fibre, multi-point or distributed and multimodal simultaneous measurements can be easily accomplished on the same fibre [19]. Considering all these advantages, optical fibre sensing technology offers an attractive alternative to traditional electrical sensing technology for permanent monitoring of oil well reservoirs.

The goal of this research is to explore optical fibre-based sensing technologies that can significantly boost the performance and withstand extreme conditions prevalent in offshore O&G environment. Sensing in O&G sector involves measurement of different parameters like pressure, temperature, vibration, flow and acoustics. Sensing should be done throughout all stages of O&G production, which means that the sensor should be active on the surface, along the pipeline and even in the down-hole. The measurements are to be taken throughout the well, from the surface to the total depth of the oil well reservoir [2]. Figure 1.1 shows the various stages where sensors are required in O&G industry.

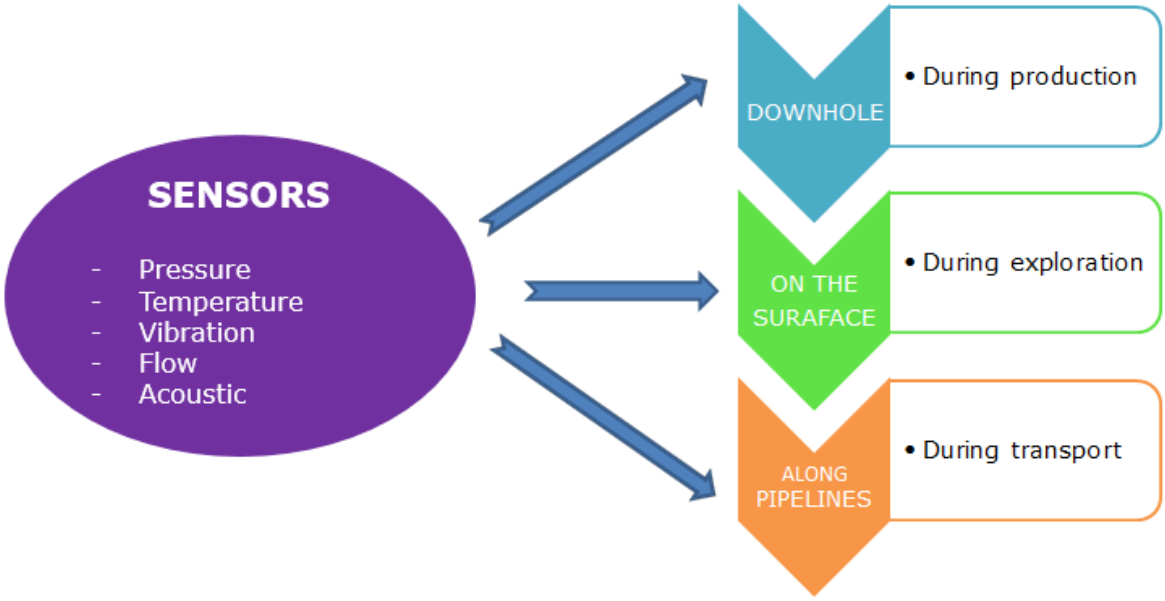

Figure 1.1 Sensor requirements in O&G industry

The elemental part of optical sensor design is the identification of the key technology which best suits the needs of the O&G industry. There are different optical sensing methodologies, but the selection needs to be done considering the down-hole environmental conditions, level of sensitivity and accuracy required in physical parameter measurements

1.2 Research Gap

Although considerable studies have been done in the field of analytical, experimental and numerical aspects of various optical fibre sensors, a feasible and effective sensing technique for accommodating all needs of oil industry is yet to be devised [20-21].

Considering the O&G extreme environmental conditions and increasing exploration depth, there is an urgent need for a greater number of reliable sensors down-hole for sensing different critical parameters like temperature, pressure, vibration, etc. Existing fibre optic sensors in the O&G industry are based on step index single mode fibres (SMF) which offers limited performance for multi-parameter sensing, as it operates within a narrow wavelength region.

Another important factor limiting the performance of these sensors in the harsh environment is its low SNR. A typical remote fibre optic sensing system consisting of an FBG (fibre Bragg grating) sensor located 150 km far away from the monitoring station offered only a SNR of 1 dB (decibels) [22]. Multi-parameter sensing also induces problem like cross-sensitivities which also affects the overall SNR of the sensing system. Hence, the new sensing technique should be competent to perform multi-parameter sensing at multiple locations with enhanced SNR and improved sensitivity.

The project will be focused on integration of multiple optical sensing approaches on the same platform for multi-point, multi-parameter sensing. The new photonic crystal fibre (PCF) based, multimodal sensor configuration will utilise a multi-wavelength approach, to overcome the challenges of current fibre optic sensors operating in a single wavelength window. PCFs flexibility in modifying their structural and material properties offer the multimodal sensors with optimum characteristics and newer sensing capabilities.

1.3 Research Aim and Objectives

The aim of the research is to investigate a novel multimodal fibre optic sensor configuration for multi-parameter sensing and SNR improvement through signal intensity enhancement. To accomplish this goal, the project will involve specific objectives to investigate the multi-wavelength, multimodal sensing capability and signal intensity improvement through different structural and material property optimisations of the fibre sensor.

The first objective is to identify a suitable fibre optic sensing technology, satisfying the sensing requirements of O&G industry for HPHT field conditions. Therefore, various computational and experimental investigations to understand

the feasibility of the identified fibre optic sensing technique for long distance, multi-point multi-parameter sensing will be carried out.

The second objective is to mathematically model and simulate the new fibre optic sensor configuration and investigate the influence of various structural parameters, material infiltrations and material doping on the electric field intensities, to enhance the sensor's SNR for achieving longer sensing range and signal propagation distance. Furthermore, the effect of sensor positioning and fibre grating parameters for improved SNR and multi-point multi-parameter sensing capabilities will be investigated.

The third objective is to develop rare earth doped glass materials using suitable fabrication techniques and carry out different spectroscopic investigations in order to characterise its suitability for O&G multimodal fibre optic sensing applications. Furthermore, the effect of doping concentration and different source excitation signals will be examined to understand its influence on the signal intensity from the sensor.

The fourth objective is to investigate the suitability of the developed rare earth doped sensors for O&G distributed temperature sensing (DTS) applications. Moreover, analysis of the effect of rare earth doping on the signal intensity of the sensor, which will contribute to the overall SNR improvement of the fibre optic sensor configuration.

The last objective is to propose a multimodal fibre optic sensor configuration combining features of FBG, PCF and rare earth doping; extracting their atomic, molecular and vibro-rotational characteristics for improved sensing (multimodal) in the O&G industry.

1.4 Thesis Organisation

The thesis consists of eight chapters accommodating relevant results and discussions based on the set of objectives of the research project. Chapter 1 provides the motivation, scope and objectives of the research work carried out. A brief review on the sensing and condition monitoring scenario and the sensing requirements of O&G industry has been discussed. Following this, the objectives and methodology used in the research work is included.

Chapter 2 comprises of the literature review carried out on different fibre optic sensing technologies. The review looks into appropriate techniques required for long distance multi-point multimodal fibre optic sensor configuration as needed by the oil industry. The literature review also focusses on different possibilities to enhance the performance of the fibre optic sensors for O&G application.

Chapter 3 includes different theoretical investigations carried out on fibre optic core-cladding structural optimisations, material infiltrations and material doping to enhance electric field confinements and thereby improve SNR for long distance, remote O&G sensing applications. Investigations have been carried out to analyse the structural parameter dependence and material properties influence on various propagation characteristics of the PCF. The specialised microstructure of PCF enables stronger light confinements within the core, facilitating long distance light propagation.

Chapter 4 consists of the theoretical and experimental investigations carried out on FBG sensors for enhancing its SNR, undertaking different approaches like FBG reflectivity-bandwidth optimisation and FBG sensor positioning. Fibre grating parameters were tuned, to incorporate multiple FBG sensors on the same optical fibre with minimal signal crosstalk and enhanced reflectivity for improved SNR. Furthermore, a new approach of FBG sensor positioning has

been investigated to improve FBG strain sensitivity for structural health monitoring of O&G structures.

Chapters 5 and 6 report various spectroscopic investigations carried out on rare earth doped glass materials required for rare earth-FBG multi-parameter sensor. Different rare earth doped glasses were fabricated, to analyse specific material doping implications and the effect of different source or excitation signals on the output signal intensity, in order to optimise the SNR of the sensor. Absorption, photoluminescence and Raman spectroscopic investigations were carried out on the synthesised rare earth doped glass materials to identify their suitability for multiparameter and distributed fibre optic sensing for O&G applications. Photoluminescence and Raman based temperature sensing has been demonstrated using the prepared rare earth doped glass materials.

Chapter 7 includes the final proposed configuration of the novel multimodal fibre optic sensor consisting of rare earth doped microstructured-FBG sensor and its associated instrumentation to overcome the technical difficulties and challenges of the sensors used in O&G industry. The integrated sensor combination is likely to overcome the limitations of existing fibre optic sensors with regards to SNR, sensing range and multimodal sensing capability. The new sensor configuration operating in multiple wavelength regimes in a multiplexed fashion, is competent to perform multi-parameter sensing.

Finally, Chapter 8 summarises the thesis and also includes the relevant conclusion of the investigations carried out. The contributions and future scope of the research work carried out are also provided in this chapter.

1.5 Summary

This chapter discusses about the need for the development of a novel multimodal sensor for the condition monitoring of O&G critical parameters like temperature, pressure, etc. The technical difficulties and shortcomings of the traditional electrical sensors within the oil industry has been examined. Fibre optic sensor have been identified as a suitable sensing solution for the O&G industry considering the prevalent harsh environmental conditions. A scope for multimodal sensors with improved sensing capabilities through the development of a novel fibre optic sensor configuration has been discussed.

1.6 References

[1] Lehmkoster J and Schroder T. Oil and gas from the sea*. World Ocean Review. maribus gGmbH*. 2014.

[2] Algeroy J, Lovell J, Tirado G, Meyyappan R, Brown G, Greenaway R, *et al*. Permanent Monitoring: Taking it to the Reservoir. *Oilfield Review Spring.* 2010; 22(1):34-41.

[3] Zhang Y.Z, Xiao L.Z, Fu J, Chen H and Zhao X. The perspective of the permanent monitoring with an FBG sensor network in oil and gas production in China. *ICMIT 2005: Information Systems and Signal Processing: International Society for Optics and Photonics*. 2005; 60410X-60410X6.

[4] Xu X, Peng G, Liu X and Shao Y. Oil and Gas Exploration Information Integration Management Plan Based on GIS Technology. *Computational and Information Sciences (ICCIS 2012).* 2012; 526-529.

[5] Akhondi M.R, Talevski A, Carlsen S and Petersen S. Applications of Wireless Sensor Networks in the Oil, Gas and Resources Industries. *Advanced Information Networking and Applications (AINA).* 2010; 941-948.

[6] Ahmed R.M, Soriano Arambulo V.H and Stalford H.L. Intelligent Casing-Intelligent Formation (ICIF) Design. *Offshore Technology Conference*. 2014.

[7] Zhang Y.Z, Xiao L.Z and Wang J.Y. Oil Well Real-time Monitoring With Downhole Permanent FBG Sensor Network. *Control and Automation. ICCA 2007, IEEE International Conference.* 2007; 2591-2594.

[8] Makhlouf A.S.H, Aliofkhazraei M, editors. Handbook of Materials Failure Analysis With Case Studies from the Oil and Gas Industries. *Butterworth-Heinemann*. 2015.

[9] Gysling D.L and Bostick F.III. Changing paradigms in oil and gas reservoir monitoring-the introduction and commercialization of in-well optical sensing systems. *15th Optical Fiber Sensors Conference Technical Digest, OFS 2002*, *IEEE.* 2002; 43-46.

[10] Meehan N. Reservoir Monitoring Handbook. *Elsevier Science & Technology Books*. 2012.

[11] Craig B. Deep Oil and Gas Well Construction. *Advanced Materials & Processes.* 2008; 33-35.

[12] DeBruijn G, Skeates C, Greenaway R, Harrison D, Parris M, James S, *et al*. High-Pressure, High-Temperature Technologies. *Oilfield Review Autumn.* 2008; 46-60.

[13] Hoffmann L, Muller M.S, Kramer S, Giebel M, Schwotzer G, Wieduwilt T. Applications of fibre optic temperature measurement. *Proceedings of the Estonian Academy of Sciences, Engineering.* 2007; 13(4):363-378.

[14] Mukhopadhyay S.C. New Developments in Sensing Technology for Structural Health Monitoring*. Springer*. 2011.

[15] Lee B. Review of the present status of optical fiber sensors. *Optical Fiber Technology.* 2003; 9(2):57-79.

[16] Hill D. Managing Oil and Gas with Fibre-Optic Sensing. *EIC Energy Focus Spring 2014.* 2014; 221-222.

[17] Choudhury P, Singh O.N. Frontiers in Optical Technology: Materials and Devices. *Nova Publishers*. 2007.

[18] Gholamzadeh B, Nabovati H. Fiber optic sensors. *World Academy of Science, Engineering and Technology.* 2008; 42(3):335-340.

[19] Kinet D, Megret P, Goossen K.W, Qiu L, Heider D, Caucheteur C. Fiber Bragg grating sensors toward structural health monitoring in composite materials: Challenges and solutions. *Sensors.* 2014; 14(4):7394-7419.

[20] Cooper KL, Wang A, Pickrell GR. Optical Fiber High Temperature Sensor Instrumentation for Energy Intensive Industries. Virginia Polytechnic Institute and State University, Blacksburg, VA; 2006.

[21] Reed C, Robinson AJ, Smart D. Techniques for monitoring structural behaviour of pipeline systems. American Water Works Association; 2004.

[22] Fernandez-Vallejo M, Lopez-Amo M. Optical fiber networks for remote fiber optic sensors. *Sensors.* 2012; 12(4):3929-3951.

2. LITERATURE REVIEW

2.1 Introduction

This chapter presents a detailed literature review carried out on different fibre optic sensing technologies. The focus of the review is to look into a suitable long-distance multi-point multimodal fibre optic sensor configuration as required for O&G applications. The literature review also investigates different possibilities to enhance the performance of the fibre optic sensors for signal intensity enhancement and thereby SNR improvement for O&G application.

2.2 Fibre-Optic Sensing Technologies

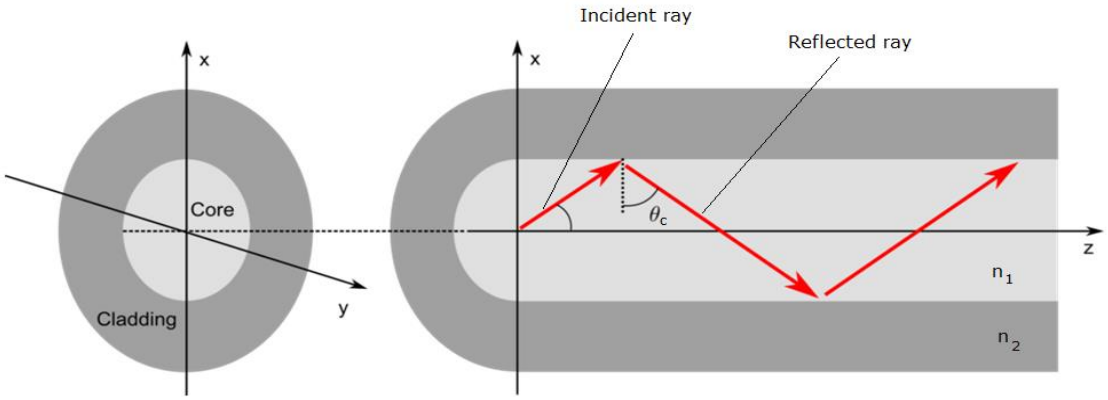

Figure 2.1 Schematic of light propagation through an optical fibre

Optical fibre is a medium through which light can propagate and the underlying principle is total internal reflection. Figure 2.1 illustrates the light propagation through an optical fibre. If the angle of incidence of the incident ray is greater than the critical angle the light ray gets reflected and confined within the core, else it is refracted. Critical angle is defined by Snell's law and is given by:

$$\sin\theta_c = \frac{n_2}{n_1}$$

where, n_1 and n_2 corresponds to the core and cladding refractive indices respectively.

Optical fibres can be used as sensors for sensing various physical parameters like temperature, pressure, strain, etc., wherein the parameter to be sensed modulates various properties of light. Existing optical fibre sensing technologies are categorised based on the effects used to measure physical phenomena and also the light modulation techniques used. In optical fibre, sensor information is conveyed as a variation in intensity, frequency, phase, polarization, wavelength or their combination of light [1]. Optical fibre sensing techniques like Raman [2], interferometry (Fabry-Perot, Michelson) [3-5], Bragg gratings [6], Brillouin [7] etc., are proficient to monitor different physical parameters such as pressure, temperature, strain, chemical concentration, flow, etc.

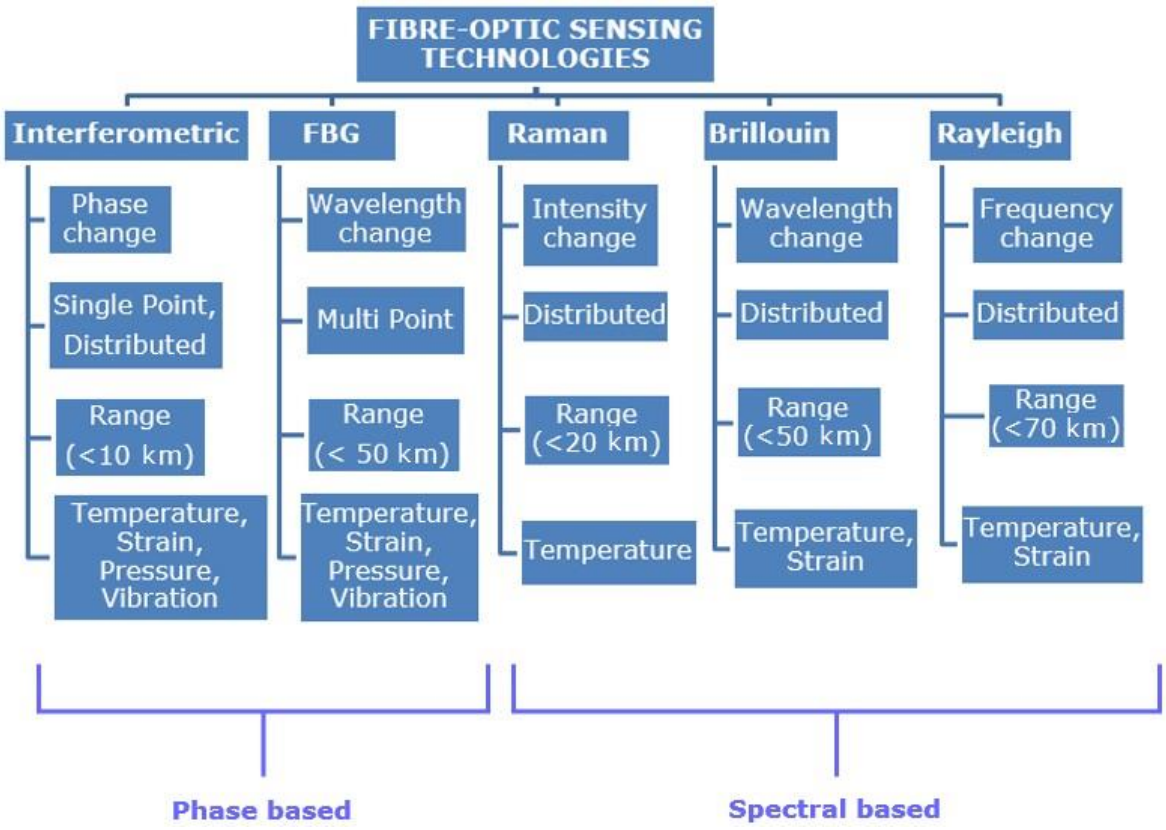

Figure 2.2 Comparison of fibre-optic sensing technologies [3-9]

Figure 2.2 shows the comparison between different optical fibre sensing technologies [3-9]. Distributed fibre optic sensor (Figure 2.3 (a)) enables continuous measurements along the entire length of the sensing fibre, whereas

quasi distributed or multi-point sensors (Figure 2.3 (b)) carries out sensing along specific points of the fibre sensors. Multimodal fibre optic sensors are capable of sensing multiple sensing modalities like phase, wavelength, polarisation etc., which can be utilised for multi-parameter sensing. Multi-parameter sensing involves sensing of multiple parameters, which can be physical parameters like temperature, pressure, vibration, etc., or chemical parameters.

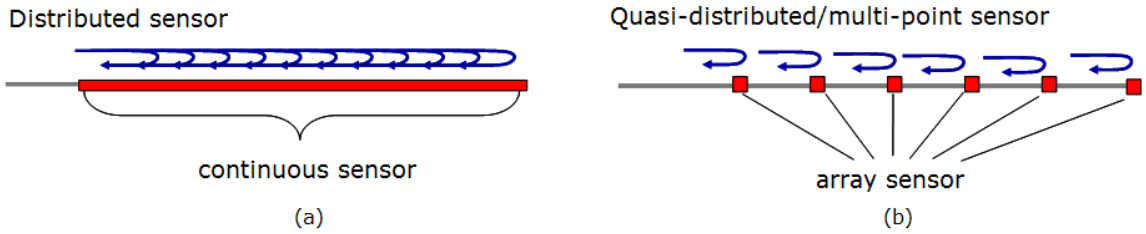

Figure 2.3 (a) Distributed fibre optic sensor and (b) quasi-distributed fibre optic sensor

Fibre optic sensors are mostly based on conventional step index fibres, wherein the core has got higher refractive index than the cladding [10]. However, different kinds of losses like the leakage or mode confinement losses experienced by these traditional fibres is a major limitation, especially when looking for long distance fibre optic remote sensing applications [11-12]. Furthermore, noises are frequently generated within the fibre optic sensing system and also from the environment which greatly influences the noise floor performance and the weak signal detection especially in largescale quasi-distributed sensing network [13]. Hence, to compensate for these noise effects within the sensing system and also the losses in the fibre sensors, advanced techniques are required for various O&G remote sensing applications. Moreover, the oil industry is keen on developing multi-point or distributed multimodal sensors, for the condition monitoring of critical parameters like pressure,

temperature, vibration, strain, etc., [14-15]. Multiparameter sensors provides versatile sensing solutions, enabling miniaturisation of the sensors and also bringing new sensor functionalities with improved measurement performances for sensing different critical parameters [16].

The literature review conducted revealed that, FBG sensors have several distinct advantages over other optical fibre sensors. They are competent to sense almost all physical parameters such as temperature, strain, pressure, vibration, etc., and also offer multi-point sensing with appreciably good range. Specific advantages of FBG sensors over other types of fibre-optic sensors are:

- They give wavelength encoded measurements and hence information is not susceptible to light power fluctuations [17].
- Multiple gratings can be inscribed on to the same fibre, taking advantage of the wavelength multiplexing capability [18]. This enables them to read many numbers of sensors on very few fibres, resulting in reduced cabling requirements and easier installation.
- Multi-point or quasi-distributed sensing can be achieved in a cost-effective and compact manner [19].
- The sensor responses to strain and temperature in linear and additive manner [20-21].

A major limitation of FBG sensor is its cross-sensitivity, as it responds to multiple parameters like temperature and strain in a coupled fashion [22]. Consequently, the effects of these parameters need to be separated out from each other, in order to make measurements simultaneously or separately. Hence, the existing FBG technology needs to be adapted to overcome its technical difficulties, for ensuring better performance for the oil industry.

Many techniques have already been explored for the discrimination of physical parameters in FBG sensor. A common approach is to engage two FBGs in close proximity, wherein one is the sensing FBG and the other is the reference FBG which is kept isolated from one of the parameters [23]. Furthermore, the sensor and reference gratings can be on the same or different optical fibres as well [24]. Another method is to employ two FBGs operating at different Bragg wavelengths, responding distinctly to different parameters [25]. Besides this, measurement of wavelength shift in two FBGs, showing different responses to parameters like temperature and strain enables simultaneous measurement of the two parameters [26]. An alternative technique proposed was, FBGs inscribed on different-diameter fibres, giving distinct strain responses and same temperature responses [5, 27].

However, utilising multiple FBGs for distinguishing various physical parameters restrict the number of sensors that can be deployed down-hole. The major factor deciding the number of FBG sensors that can be designed on the optical fibre is the wavelength range, which is also termed as the "wavelength window". Individual sensors need room to vary up and down in wavelength corresponding to changes in their environmental parameters [28]. One method to accommodate more FBG sensors on the optical fibre is to narrow down the spectral width of its reflected signal. Furthermore, FBG sensors also experience low SNR values with increasing transmission length [29-30]. Hence, in order to improve SNR, amplitude of the FBG reflectivity signal need to be increased and the noise caused by crosstalks from adjacent channels need to be minimized.

Since FBG sensor gives higher response to strain than pressure, polymer coatings are required to improve its sensitivity. These polymer coatings convert transverse pressure on the sensor into longitudinal strain. For example,

polyamide [31-33] and acrylate [34] coatings considerably increases the sensor sensitivities to temperature and strain.

2.3 Technical challenges

Major challenges of multi-point multimodal FBG sensing are listed below:

- Cross-sensitivity - It is a key problem in FBG sensors, where one physical parameter (temperature or strain) influences the value of the other.
- Cross coupling - Nonlinear coupling of sensor parameters makes it hard to decouple measurands of different physical variables.
- Transmission and sensing range - The range of the sensor is very important because physical parameters are to be measured from ultra-deep oil wells.
- SNR - SNR can be improved by increasing the reflected signal amplitude and by reducing the signal attenuation and crosstalks.
- Number of sensors – The finite optical spectrum limits the number of sensors that can be designed. More sensors are required to achieve multi-point or distributed sensing down-hole.
- Sensitivity - Enhanced sensitivity to physical parameters like pressure and temperature can be achieved with suitable polymer coatings.

Although FBGs are capable of sensing almost all physical parameters like temperature, strain, pressure, vibration, etc., however, they respond to multiple sensing parameters in a coupled fashion. Therefore, to measure these physical parameters separately or both simultaneously, the effects of temperature and strain need to be decoupled from each other. Therefore, multi-parameter measurements become important, as it allows to reduce the size, cost and complexity of the sensing system, and also provides parameter discrimination

in situations where cross-sensitivity is a critical issue [35]. Also, more sensors are required down-hole with longer sensing range for effective remote monitoring of the oil wells. However, this results in higher signal attenuation, crosstalks and losses. In order to avoid this situation, there is a need to enhance the sensing signals and also reduce the fibre losses. Considering the factor that the optical spectrum is limited, so the broad reflected spectrum limits the number of sensors that can be designed. Therefore, inorder to include more number of sensors, the spectral width of the reflected signal need to be reduced. Even though intensive researches have been carried out on specialised fibres like PCFs [36-37] and FBGs for many years, **to the best of our knowledge, no work has been reported utilising their synergy in O&G sensing applications.** PCF-FBG based sensor is capable of differentiating the effects of different parameters like temperature and strain [38]. Their combination can improve the overall performance of the sensor system in terms of power, energy scaling and discrimination of cross-sensitivities [39-40]. The reflectivity peaks from the PCF-FBG sensor have inconsistent sensitivity to external parameters which helps to attain multi-parameter measurement simultaneously, offering good stability and wide range of broadband tuning [41-42].

The main advantage of PCF is their high light confinement characteristics which is otherwise difficult to achieve in ordinary conventional fibres. LCPCFs (Liquid crystal PCFs) open new perspectives in sensing applications [43]. With the addition of liquid crystals on to the PCF air holes, its output signal experiences a wavelength shift corresponding to the variation in physical parameters like temperature [44-45]. Liquid crystals also provide means of achieving active control over PCF propagation and polarization characteristics [46]. The thermal and electrical tuning capabilities of LCPCFs along with their unique spectral and

polarization properties opens up their possibilities for multi-parameter fibre optic sensing [43]. Furthermore, through PCF nanostructuring, ultra-low confinement losses can be achieved in a large wavelength region [47-48]. The guidance properties of the PCF, having radially periodic cladding structure of concentric high and low-index layers can be improved by optimising its effective refractive index [49]. A core with higher refractive index facilitates higher light confinement [50] which in turn increases the propagation distance of the light signal. One approach to manipulate the core refractive index is through rare earth doping [51-53]. The refractive index of silicate glass increases with increasing rare earth concentration [54]. Another offshoot advantage of doping the fibre core with rare earth elements is its photoluminescence and Raman signatures [55]. For different laser excitations the doped glasses generate specific Raman and photoluminescence emissions corresponding to each rare earth element [56]. These Raman and photoluminescence emissions can be utilised for sensing applications as they are sensitive to physical parameters like temperature and also to chemicals [57-60]. In addition, Raman and photoluminescence emissions from the rare earth doped core PCF-FBG sensor facilitates multi-parameter sensing. Raman based sensing technique also facilitates distributed temperature sensing [61], which is very beneficial while looking for the complete temperature profile of the oil well. To sum up, optical fibre sensing technologies are promising solutions for smarter sensing systems in offshore oil industry.

2.4 Signal to Noise Ratio Perspectives in an optical sensing system

SNR is defined as the ratio of signal power to the noise power and is often expressed in decibels (dB) [62]. In a sensing system, SNR compares the level

of a desired signal to the level of background noise. In the design of new optical sensors with improved performance indicators, the most important issue is how to enhance the SNR within the chemical and biological environments [63]. The measured signal or the signal from the fibre-optic sensors are generally very weak when used for remote sensing applications [64]. Extracting effective information from the weak signal is an extremely difficult process. In a fibre optic sensing system consisting of a light source, optical fibre sensor and the detector, noise can creep into the sensing system from any three of these elements and also the environment. These kinds of noises are generally called as Common Mode Noises (CMN) [65]. At the source end, noise can be an intensity or spectral change and at the detector end noise can arise from its corresponding condition electronics and is known as laser noise and detector noise respectively [66]. Furthermore, the losses experienced by the medium or the fibre sensors also contributes to the lower SNR. In an optical system different kind of noises can arise, such as Relative Intensity Noise (RIN), mode partition noise, quantum noise, etc., from the source; modal noise, polarization dependent noise, phase noise, etc., from the medium and shot noise, dark noise, thermal noise, etc., from the detector [67-69].

In FBG based sensing systems, noise caused by the Optical Return Loss (ORL) is the main noise contributor, and coupler is the main source of signal attenuation [70]. Thermal noise also affects the SNR of the FBG reflected signal, due to the strong background spectrum [71]. One approach to handle the SNR issue is noise filtering using suitable signal processing techniques [72]. Noises within FBG based sensing system can be reduced by implementing a Bragg peak detection method that is immune to noise [73]. Another method to improve the SNR is by improving the back-reflectivity signal from fibre sensor [74]. Thermal

noise is a serious issue for Raman based sensors [75]. Hence, SNR improvement is also required for Raman based distributed sensors [76]. A commonly employed technique to increase SNR is averaging the received signal, which reduces the signal noise. However, averaging also increases the signal acquisition time which proves unsuitable for most real-time distributed sensing systems [77]. Deconvolution of Raman spectra is another technique used to separate out useful Raman peaks submerged in noise background [78]. Furthermore, with recent advancements in Artificial Intelligence (AI) and machine learning techniques, noise can be easily separated out from the signal using suitable algorithms [79]. At the detector end of the sensing system, noise is no longer an issue as the instruments can be trained to identify the noise models and its stochastic characteristics using different learning algorithms [80-81]. New data-driven approaches are emerging for sensing systems, replacing the traditional model-based approaches [82,83]. The whole idea of using data driven techniques for fibre optic sensing systems is to get rid of the noise frequencies at the detector and obtain a useful signal from a tiny response from the sensor. Furthermore, using data driven approaches, the cross-sensitivity issues of the multi-parameter sensors can be reduced. Hence, this thesis will look into different investigations to enhance the signal from the fibre sensors, assuming noise is constant, to improve the overall SNR of the sensing system, as noise can be easily handled with new AI techniques.

2.5 Summary

A detailed literature review of different fibre optic sensing techniques was carried out in this chapter, to identify a feasible sensing solution for the oil industry. The different classifications of the fibre optic sensors were discussed.

The technical challenges associated with the most commonly used FBG sensors were described. Moreover, a thorough review leading to a new idea for multimodal sensing using a novel fibre optic configuration has been discussed. Lastly, to improve the performance of the multimodal sensor in terms of its SNR, different approaches and techniques have been identified. The exhaustive literature review provided new insights towards the development of a unique multimodal fibre optic sensor for oil O&G applications.

2.6 References

[1] Udd E. Fiber optic smart structures. *Proceedings of the IEEE.* 1996; 84(6):884-894.

[2] Kee HH, Lees GP, Newson TP. 1.65 μm Raman-based distributed temperature sensor. *Electronics Letters.* 1999; 35(21):1869-1871.

[3] Chen X, Shen F, Wang Z, Huang Z, Wang A. Micro-air-gap based intrinsic Fabry-Perot interferometric fiber-optic sensor. *Applied Optics.* 2006; 45(30):7760-7766.

[4] Pinet É. Fabry-Pérot fiber-optic sensors for physical parameters measurement in challenging conditions. *Journal of Sensors.* 2009; 2009.

[5] Song M, Lee B, Lee SB, Choi SS. Interferometric temperature-insensitive strain measurement with different-diameter fiber Bragg gratings. *Optics Letters.* 1997; 22(11):790-792.

[6] Rao Y. In-fibre Bragg grating sensors. *Measurement Science and Technology.* 1997; 8(4):355.

[7] Parker T, Farhadiroushan M, Handerek V, Rogers A. Temperature and strain dependence of the power level and frequency of spontaneous Brillouin scattering in optical fibers. *Optics Letters.* 1997; 22(11):787-789.

[8] Wait P, De Souza K, Newson T. A theoretical comparison of spontaneous Raman and Brillouin based fibre optic distributed temperature sensors. *Optics Communications.* 1997; 144(1):17-23.

[9] Luo J, Hao Y, Ye Q, Hao Y, Li L. Development of optical fiber sensors based on brillouin scattering and FBG for on-line monitoring in overhead transmission lines. *Journal of Lightwave Technology.* 2013; 31(10):1559-1565.

[10] Fidanboylu K and Efendioglu H. Fiber optic sensors and their applications. Fiber optic sensors and their applications. *5th International Advanced Technologies Symposium (IATS'09)*; 2009. 2-3.

[11] Chou C, Sun N. Analysis of leaky-mode losses for optical fibers. *Journal of the Optical Society of America* B*.* 2008; 25(4):545-554.

[12] Alexander Schmidt M, Argyros A, Sorin F. Hybrid Optical Fibers–An Innovative Platform for In-Fiber Photonic Devices. *Advanced Optical Materials.* 2016; 4(1):13-36.

[13] Duo Y, Xiangge H, Fei L, Lijuan G, Min Z, Xiaokang Q, et al. Self-suppression of common-mode noises of the different fiber optic interferometric accelerometers. *Optics Express.* 2018; 26(12):15384-15397.

[14] Singer JM, Karabacak DM, Farnan M, Ibrahim SK and Todd M. A fiberoptic sensing system for system health monitoring in oil & gas industry applications. *Proceedings of the European Workshop on Structural Health Monitoring*; 2016.

[15] Miah K, Potter D. A review of hybrid fiber-optic distributed simultaneous vibration and temperature sensing technology and its geophysical applications. *Sensors.* 2017; 17(11):2511.

[16] Pevec S, Donlagić D. Multiparameter fiber-optic sensors: a review. *Optical Engineering.* 2019; 58(7):072009.

[17] Lee B. Review of the present status of optical fiber sensors. *Optical Fiber Technology.* 2003; 9(2):57-79.

[18] Rao Y. Recent progress in applications of in-fibre Bragg grating sensors. *Optics and lasers in Engineering.* 1999; 31(4):297-324.

[19] Davis C, Carome E, Weik M, Ezekiel S, Einzig R. Fiberoptic Sensor Technology Handbook, 1986. *Optical Technology Inc., Herndon, VA.* 1986.

[20] Zhang W, Dong X, Zhao Q, Kai G, Yuan S. FBG-type sensor for simultaneous measurement of force (or displacement) and temperature based on bilateral cantilever beam. *Photonics Technology Letters, IEEE.* 2001; 13(12):1340-1342.

[21] Amos S, Prabhu R, Njuguna J. Theoretical design and analysis of a sensing system for high pressure and temperature measurement in subsea underwater applications. *OCEANS 2017-Aberdeen, IEEE*; 1-7.

[22] Amos SU. Cross sensitivity analysis of optical fibre-based sensing for high pressure, high temperature measurement in oil and gas applications. PhD thesis, Robert Gordon University; 2018.

[23] Xu M, Archambault J, Reekie L, Dakin J. Thermally-compensated bending gauge using surface-mounted fibre gratings. *International Journal of Optoelectronics.* 1994; 9(3):281-284.

[24] Song M, Lee SB, Choi SS, Lee B. Simultaneous measurement of temperature and strain using two fiber Bragg gratings embedded in a glass tube. *Optical Fiber Technology.* 1997; 3(2):194-196.

[25] Xu M, Archambault J, Reekie L, Dakin J. Discrimination between strain and temperature effects using dual-wavelength fibre grating sensors. *Electronics Letters.* 1994; 30(13):1085-1087.

[26] Rogers AJ, Handerek VA, Kanellopoulos SE and Zhang J. New ideas in nonlinear distributed optical fiber sensing. *European Symposium on Optics for Environmental and Public Safety,* International Society for Optics and Photonics; 1995. 162-174.

[27] James S, Dockney M, Tatam R. Simultaneous independent temperature and strain measurement using in-fibre Bragg grating sensors. *Electronics Letters.* 1996; 32(12):1133-1134.

[28] Zhou Z, Graver TW, Hsu L, Ou J. Techniques of Advanced FBG sensors: fabrication, demodulation, encapsulation and their application in the structural health monitoring of bridges. *Pacific Science Review.* 2003; 5(1):116-121.

[29] Saitoh T, Nakamura K, Takahashi Y, Iida H, Iki Y, Miyagi K. Ultra-long-distance fiber Bragg grating sensor system. *Photonics Technology Letters, IEEE.* 2007; 19(20):1616-1618.

[30] Kong D, Chang J, Gong P, Liu Y, Sun B, Liu X, et al. Analysis and improvement of SNR in FBG sensing system. *Photonic Sensors.* 2012; 2(2):148-157.

[31] Giaccari P, Limberger H, Kronenberg P. Influence of humidity and temperature on polyimide-coated fiber Bragg gratings. *Proceedings of Bragg Gratings, Photosensitivity, and Poling in Glass Fibers and Waveguides.* 2001.

[32] Gusarov A, Chojetzki C, Mckenzie I, Thienpont H, Berghmans F. Effect of the fiber coating on the radiation sensitivity of type I FBGs. *Photonics Technology Letters, IEEE.* 2008; 20(21):1802-1804.

[33] Yeo T, Sun T, Grattan K, Parry D, Lade R, Powell B. Characterisation of a polymer-coated fibre Bragg grating sensor for relative humidity sensing. *Sensors and Actuators B: Chemical.* 2005; 110(1):148-156.

[34] Hill D, Cranch G. Gain in hydrostatic pressure sensitivity of coated fibre Bragg grating. *Electronics Letters.* 1999; 35(15):1268-1268.

[35] Frazao O, Carvalho J, Ferreira L, Araújo F, Santos J. Discrimination of strain and temperature using Bragg gratings in microstructured and standard optical fibres. *Measurement Science and Technology.* 2005; 16(10):2109.

[36] Knight J, Birks T, Russell PSJ, Atkin D. All-silica single-mode optical fiber with photonic crystal cladding. *Optics Letters.* 1996; 21(19):1547-1549.

[37] Knight JC. Photonic crystal fibres. *Nature.* 2003; 424(6950):847-851.

[38] Martelli C, Canning J, Groothoff N and Lyytikainen K. Bragg gratings in photonic crystal fibers: strain and temperature characterization. *17th International Conference on Optical Fibre Sensors,* International Society for Optics and Photonics; 2005. 5855:302-305.

[39] Jollivet C, Guer J, Hofmann P, Schulzgen A. Monolithic Fiber Lasers Combining Active PCF With Bragg Gratings in Conventional Single-Mode Fibers. *Selected Topics in Quantum Electronics, IEEE Journal of.* 2014; 20(5):36-41.

[40] Cusano A, Paladino D. Developments and applications of microstructured fiber Bragg gratings. *Optical Fiber Communication Conference and Exposition and National Fiber Optic Engineers Conference*, Los Angeles, CA, 2011; 1-3.

[41] Zhao Y, Zhang Y, Wu D, Wang Q. Magnetic field and temperature measurements with a magnetic fluid-filled photonic crystal fiber Bragg grating. *Instrumentation Science & Technology.* 2013; 41(5):463-472.

[42] Chen W, Li J, Lu P. Progress of photonic crystal fibers and their applications. *Frontiers of Optoelectronics in China; Selected Publications from Chinese Universities.* 2009; 2(1):50-57.

[43] Wolinski T, Szaniawska K, Ertman S, Lesiak P, Domanski A, Dabrowski R, et al. Influence of temperature and electrical fields on propagation properties of

photonic liquid-crystal fibres. *Measurement Science and Technology.* 2006; 17(5):985.

[44] Algorri JF, Urruchi V, Bennis N, Sánchez-Pena JM. A Novel High-Sensitivity, Low-Power, Liquid Crystal Temperature Sensor. *Sensors.* 2014; 14(4):6571-6583.

[45] Algorri J, Zografopoulos D, Tapetado A, Poudereux D, Sánchez-Pena J. Infiltrated Photonic Crystal Fibers for Sensing Applications. *Sensors.* 2018; 18(12):4263.

[46] Rajan G. *Optical Fiber Sensors: Advanced Techniques and Applications.* CRC Press; 2015.

[47] Chen D. Nanostructured Photonic Crystal Fiber with Ultra-high Birefringence. *2006 International Symposium on Biophotonics, Nanophotonics and Metamaterials,* IEEE; 2006. 362-365.

[48] Islam MS, Ng BWH, Abbott D. Porous-core photonic crystal fibers guide polarization-preserving terahertz waves. *Laser Focus World.* 2018; 54(5):49.

[49] Cubillas AM, Unterkofler S, Euser TG, Etzold BJ, Jones AC, Sadler PJ, et al. Photonic crystal fibres for chemical sensing and photochemistry. *Chemical Society Reviews.* 2013; 42(22):8629-8648.

[50] Pinto AM, Lopez-Amo M. Photonic crystal fibers for sensing applications. *Journal of Sensors.* 2012; 2012.

[51] Lumholt O, Bjarklev A, Rasmussen T, Lester G. Rare earth-doped integrated glass components: modeling and optimization. *Journal of Lightwave Technology.* 1995; 13(2):275-282.

[52] Wang F, Hu L, Xu W, Wang M, Feng S, Ren J, et al. Manipulating refractive index, homogeneity and spectroscopy of Yb-doped silica-core glass towards

high-power large mode area photonic crystal fiber lasers. *Optics Express.* 2017; 25(21):25960.

[53] Nandi P, Srinivasan A, Jose G. Structural dependent thermal and optical properties of rare earth doped glass with mixed glass formers. *Optical Materials.* 2009; 31(4):653-659.

[54] Chimalawong P, Kirdsiri K, Kaewkhao J, Limsuwan P. Investigation on the Physical and Optical Properties of Dy3+ Doped Soda-Lime-Silicate Glasses. *Procedia Engineering.* 2012; 32:690-698.

[55] Cui J, Hope GA. Raman and Fluorescence Spectroscopy of CeO2, Er2O3, Nd2O3, Tm2O3, Yb2O3, La2O3, and Tb4O7. *Journal of Spectroscopy.* 2015; 2015.

[56] Burruss RC, Ging TG, Eppinger RG, Samson AM. Laser-excited fluorescence of rare earth elements in fluorite: Initial observations with a laser Raman microprobe. *Geochimica et Cosmochimica Acta, Elsevier*. 1992; 56(7):2713-23.

[57] Quoi KW, Lieberman RA, Cohen LG, Shenk DS, Simpson JR. Rare-earth doped optical fibers for temperature sensing. *Journal of Lightwave Technology.* 1992; 10(6):847-852.

[58] Amira Z, Bouyahi M, Ezzedine T. Measurement of Temperature through Raman Scattering. *Procedia Computer Science.* 2015; 73:350-357.

[59] Dakin JP, Pratt DJ, Bibby GW, Ross JN. Distributed optical fibre Raman temperature sensor using a semiconductor light source and detector. *Electronics Letters.* 1985; 21(13):569-570.

[60] Wolfbeis OS. Materials for fluorescence-based optical chemical sensors. *Journal of Materials Chemistry.* 2005; 15(27-28):2657-2669.

[61] Soto MA, Nannipieri T, Signorini A, Lazzeri A, Baronti F, Roncella R, et al. Raman-based distributed temperature sensor with 1 m spatial resolution over 26 km SMF using low-repetition-rate cyclic pulse coding. *Optics Letters.* 2011; 36(13):2557-2559.

[62] Daniel SSA. An efficient routing protocol under noisy environment for mobile ad hoc networks using fuzzy logic. *International Journal of Advanced Research in Artificial Intelligence.* 2013; 2(9).

[63] Pan J, Cha T, Chen H, Choi J. Carbon nanotube-based optical platforms for biomolecular detection. *Carbon Nanotubes and Graphene for Photonic Applications. Elsevier*. 2013; 270-303.

[64] Liu X, Jin B, Bai Q, Wang Y, Wang D, Wang Y. Distributed Fiber-Optic Sensors for Vibration Detection. *Sensors.* 2016; 16(8).

[65] Duo Y, Xiangge H, Fei L, Lijuan G, Min Z, Xiaokang Q, et al. Self-suppression of common-mode noises of the different fiber optic interferometric accelerometers. *Optics Express.* 2018; 26(12):15384-15397.

[66] Duan L. Thermal Noise-Limited Fiber-Optic Sensing at Infrasonic Frequencies. *IEEE Journal of Quantum Electronics.* 2015; 51(2):1-6.

[67] Wild G, Richardson S. Analytical modelling of interrogation systems for fibre Bragg grating sensors. *35th Australian Conference on Optical Fibre Technology, IEEE,* 2010; 1-4.

[68] Ford HD, Beddows R, Casaubieilh P, Tatam RP. Comparative signal-to-noise analysis of fibre-optic based optical coherence tomography systems. *Journal of Modern Optics.* 2005; 52(14):1965-1979.

[69] Keiser G. *Optical fiber communications.* McGraw-Hill Singapore; 2010.

[70] Kong D, Chang J, Gong P, Liu Y, Sun B, Liu X, et al. Analysis and improvement of SNR in FBG sensing system. *Photonic Sensors.* 2012; 2(2):148-157.

[71] Liao C, Wang D. Review of femtosecond laser fabricated fiber Bragg gratings for high temperature sensing. *Photonic Sensors.* 2013; 3(2):97-101.

[72] Mengran Z, Haiqing Z, Hongwei W. Study of eliminating noise of signal in fiber-optic sensor system. *9th International Conference on Optical Communications and Networks, ICOCN 2010*, Nanjing, 2010; 48-50.

[73] De Pauw B, Lamberti A, Rezayat A, Ertveldt J, Vanlanduit S, Van Tichelen K, et al. Signal-to-Noise Ratio Evaluation of Fibre Bragg Gratings for Dynamic Strain Sensing at Elevated Temperatures in a Liquid Metal Environment. *Journal of Lightwave Technology.* 2015; 33(12):2378-2385.

[74] Wang X, Yan Z, Wang F, Sun Z, Mou C, Zhang X, et al. SNR Enhanced Distributed Vibration Fiber Sensing System Employing Polarization OTDR and Ultraweak FBGs. *IEEE Photonics Journal.* 2015; 7(1):1-11.

[75] McSherry M, Fitzpatrick C, Lewis E. Review of luminescent based fibre optic temperature sensors. *Sensor Review.* 2005; 25(1):56-62.

[76] Baronti F, Lazzeri A, Roncella R, Saletti R, Signorini A, Soto MA, et al. SNR enhancement of Raman-based long-range distributed temperature sensors using cyclic Simplex codes. *Electronics Letters.* 2010; 46(17):1221-1223.

[77] Sun X, Li J and Hines M. SNR improvement in a Raman based distributed temperature sensing system using a stimulated Raman scattering filter. *Fiber Optic Sensors and Applications XIV,* International Society for Optics and Photonics; 2017. 102080E.

[78] Greek LS, Schulze HG, Blades MW, Bree AV, Gorzalka BB, Turner RF. SNR enhancement and deconvolution of Raman spectra using a two-point entropy regularization method. *Applied Spectroscopy.* 1995; 49(4):425-431.

[79] de Mesquita RN, Perillo SR, dos Santos RC. Process Sensors Characterization Based on Noise Analysis Technique and Artificial Intelligence. *2005 International Nuclear Atlantic Conference - INAC 2005*, Santos, Brazil. 2005.

[80] Dürr V, Schmitz J, Cruse H. Behaviour-based modelling of hexapod locomotion: linking biology and technical application. *Arthropod Structure & Development.* 2004; 33(3):237-250.

[81] Yin J, Yang Q, Pan JJ. Sensor-Based Abnormal Human-Activity Detection. *IEEE Transactions on Knowledge and Data Engineering.* 2008; 20(8):1082-1090.

[82] Güemes A, Fernández-López A, Díaz-Maroto P, Lozano A, Sierra-Perez J. Structural health monitoring in composite structures by fiber-optic sensors. *Sensors.* 2018;18(4):1094.

[83] Joshuva A, Sugumaran V. A data driven approach for condition monitoring of wind turbine blade using vibration signals through best-first tree algorithm and functional trees algorithm: A comparative study. *ISA Transactions.* 2017 Mar 1; 67:160-72.

3. INVESTIGATIONS ON MICROSTRUCTURED FIBRE SENSORS

3.1 Introduction

This chapter focusses on the propagation characteristics and properties of the PCF with the goal of SNR improvement of the multimodal sensor configuration, through signal intensity enhancement and reduction of losses. Tuning of the structural and material characteristics of the PCF increases the electric field confinements, aiding in improving the overall SNR.

The investigations carried out are:

- Comparison of the propagation characteristics of step index single mode fibre (SMF) and PCF in terms of its electric field intensity and mode field diameter (MFD).
- Analysis of the effect of different structural parameters such as number of air hole rings, size and spacing between air holes on the propagation characteristics of the microstructured fibre.
- Study of the influence of liquid crystal infiltration on PCF parameters like confinement loss, MFD and bandgap.
- Analysis of the effect of core nanostructuring and refractive index change through different liquid crystal infiltrations on PCF parameters like confinement wavelengths, confinement losses, bandwidth, MFD, etc.
- Study of the rare earth doping effects within the core of nanostructured PCF for reduced confinement losses.

PCFs [1] also known as microstructured fibres is a new class of optical waveguides/fibres. PCFs are gaining popularity in recent years, owing to their specialised geometrical structure (core-air hole cladding) and unique properties

like guiding mechanisms and modal characteristics, making them an interesting candidate for a range of applications [2]. They produce lower optical transmission losses compared to standard silica optical fibres [3]. PCFs are more flexible than normal optical fibres, because it is possible to manage their properties, leading to a freedom of design [4]. The large refractive index difference between silica and air of the PCF enables tighter mode confinements than conventional all solid single mode glass optical fibres [5].

The main advantage of PCF [1-3] is their high light confinement characteristics which is otherwise difficult to achieve in conventional fibres. LCPCF open new perspectives in sensing applications [6]. With the addition of liquid crystals on to the PCF air holes, wavelength shifts results as the output signal with variation in physical parameters like temperature [7] and also provides means of achieving active control over PCF propagation and polarization characteristics [8]. The thermal and electrical tuning capabilities of LCPCFs along with their unique spectral and polarization properties opens up their possibilities for multi-parameter fibre-optic sensing [6].

LCPCF enables effective control over the mode confinements and light characteristics. This is because, the liquid crystal infused in the cladding holes creates a Photonic Bandgap (PBG) effect, restricting the modes within the low index core region rather than leaking. However, the integration of LCPCF based sensors with existing fibre optic sensing systems (which are mostly based on single mode fibres) are quite challenging, mainly due to their difference in core sizes and MFDs. Moreover, their integration will result in different forms of losses, which are dominated by confinement loss. Therefore, it is important to develop approaches to reduce losses occurring within the fibre core, so that signal power is enhanced and thereby transmission and sensing range of the

fibre can also be increased. By optimising geometrical parameters such as hole distribution, hole sizes, etc., of the PCF, confinement losses can be minimized. Furthermore, analysing effective area and MFD gives a better insight of leakage loss, macro-bending loss and numerical aperture of the fibre sensor.

PCFs developed using nanostructured composite materials provides special optical properties. Nanostructuring and infusion of liquid crystal materials enhances the capabilities of all silica PCF, facilitating their operation in different spectral regimes. Wavelength tunability feature of nanostructured PCF can be utilised for many sensing applications. Commercially available PCFs, fabricated from silica (SiO_2) material operate mostly in the communication wavelength band ($1.55\,\mu m$), limiting their scope for advanced fibre optic sensing applications which aims the near infrared (NIR) and mid infrared (MIR) wavelengths. Material absorption limits of silica have always been a major problem in large wavelength region [9]. All these drawbacks of SiO_2 material create a need for new materials for emerging fibre optic applications like NIR and MIR (3-6 μm) sensors, next generation communication systems in the $2.5\,\mu m$ wavelength band, MIR fibre lasers, etc., [10-11].

The properties of SiO_2 based PCF can be manipulated by two techniques - nanostructuring and fusing in liquid crystal-silica composite materials. The modified SiO_2 material shows some unique optical properties, wherein the spectral bands can be tuned to the required wavelength region. Wavelength-scale periodic microstructuring creates a dramatic change in the optical properties of the materials [5]. Nanostructured optical materials will provide special properties which can improve the capabilities of existing optical sensing technologies [12-13]. Nanostructuring of PCF air holes is expected to improve its birefringence property, reduce the confinement losses and also decrease its

effective mode area, which in turn improves the propagation distance and range Fof the fibre sensor [14]. Highly birefringent PCFs exhibit multi-parameter sensing capabilities as they have different polarisation states which show different sensitivities to physical parameters like temperature and strain [15]. Furthermore, addition of liquid crystal materials into the cladding holes modifies PCF transmission and polarisation properties, enabling them to operate within the photonic bands having highest sensitivities. Another advantage of material infusion is that it is possible to modify the properties of PCF even after its fabrication. PCF air holes filled with special materials like liquid crystals changes their optical properties in response to electric or magnetic fields or light intensity. Liquid crystal materials infused into the cladding holes creates a PBG effect, restricting the modes within the core region rather than leaking, facilitating a stronger sensing signal [16].

NIR wavelengths of the optical spectrum are of particular interest for fibre-optic sensing applications due to their improved sensitivity and accuracy compared to other spectral regions. The NIR bands have shown high sensitivities to methane gas sensing, which is of very interest in many industrial and safety applications [17-18]. Gas detection is a very crucial task in O&G industry, in order to protect their valuable assets and workers from safety hazards. The MIR wavelengths have attracted different laser spectroscopic based environmental and medical sensing applications [19-20]. Considering the growing interest of optical fibres in new application areas, it becomes important to enhance its capabilities and functionalities. Future applications will rely on well-developed optical materials and technologies along with new, modified and special properties of optical fibres [10].

Rare earth doped nanostructured silica composite materials provides specialised optical features and properties. Light propagation and sensing characteristics of fibre optic sensors can be modified by optimising their structural and material parameters. Doping of different rare earth materials and nanostructuring improves the capabilities of all silica fiber optic sensors, facilitating photoluminescence-based sensing and the operation of the sensors in different spectral regions. One main advantage of rare earth materials is that they absorb only specific Ultraviolet (UV) or visible (VIS) wavelengths and create corresponding sharp photoluminescence emissions in the VIS or infrared wavelengths. Nanostructuring and doping of rare earth materials enhances the capabilities of fibre optic sensor by reducing leakage losses and improving the signal strength, which is crucial in long distance remote sensing applications.

Rare earth doped silica material is an important optical material for new scientific and technological applications [21-22]. Different rare earth materials like Terbium (Tb), Ytterbium (Yb), Erbium (Er), Neodymium (Nd), etc., offer a wide range of photoluminescence emission profiles covering the visible and near infrared wavelengths making it the most suitable candidates for photoluminescence-based fibre optic sensors [23]. Furthermore, periodic microstructuring improves the performance of conventional optical fibre sensors, owing to its design flexibility and modification of light guidance properties [4]. Another attractive feature of PCF is that it allows the integration of light–matter interactions along the entire length of the fibre which further improves the performance of the fibre sensor system [24]. Moreover, transmission losses of PCFs are low and they have stronger light mode confinements compared to traditional silica fibres due to the large index

difference between silica core and air holes in cladding [3,5]. Nanostructuring of PCF tunes its spectral positions and photonic bandgaps [25].

3.2 Theoretical Background

PCFs are optical fibres with a complex refractive index profile that employs a microstructured arrangement of low-index material in a background material of higher refractive index [26]. Normally the background materials used in PCFs are pure or undoped silica and the low index cladding region consists of many number of air voids also known as air holes [27]. Typically, photonic crystals are periodic optical (micro or nano) structures running axially along the length of the optical fibre, that affects the propagation characteristics of the electromagnetic waves travelling through its core [5].

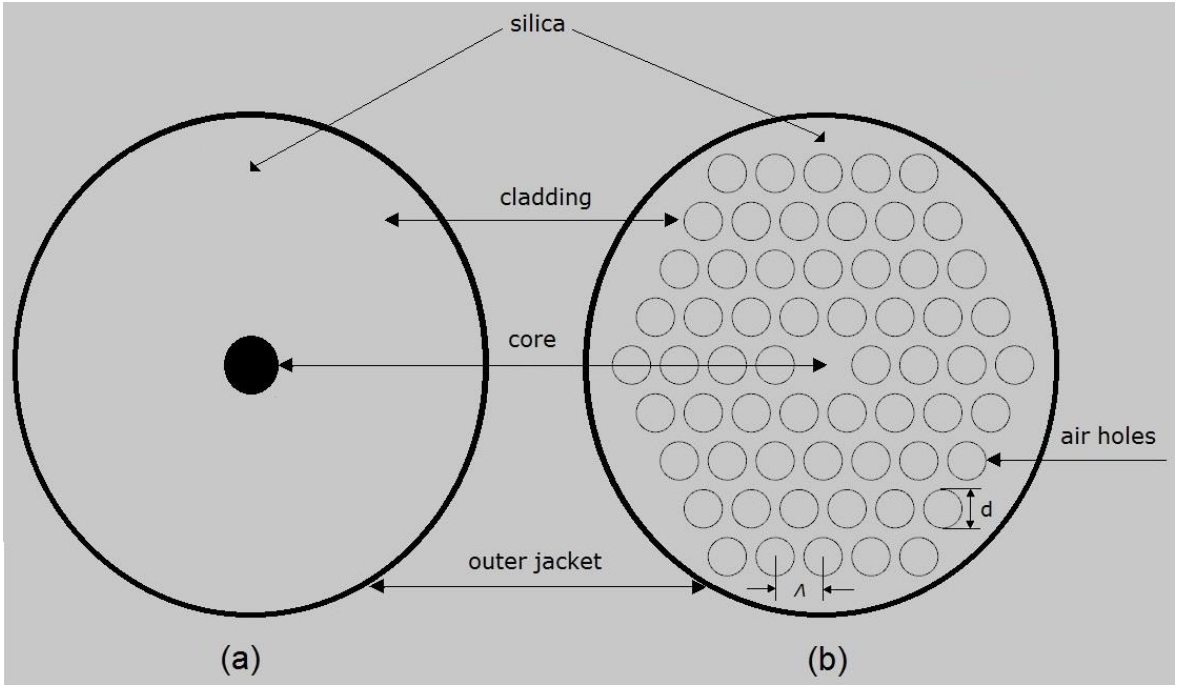

Figure 3.1: Cross-section of: (a) step-index SMF and (b) solid core PCF

Figures 3.1 (a) and (b) show the cross-sectional view of the structural difference between a standard step-index SMF and a solid core PCF with microstructured cladding. During fibre modelling, the only physical parameter that needs to be

taken into account in the case of SMF is the core diameter. On the other hand, while modelling a PCF, three geometrical parameters are to be considered: core diameter, cladding hole diameter and also the pitch (hole to hole distance). The geometrical parameters of PCF comprise of: pitch (Λ) which is the cladding hole center to center distance and the diameter of cladding air hole (d).

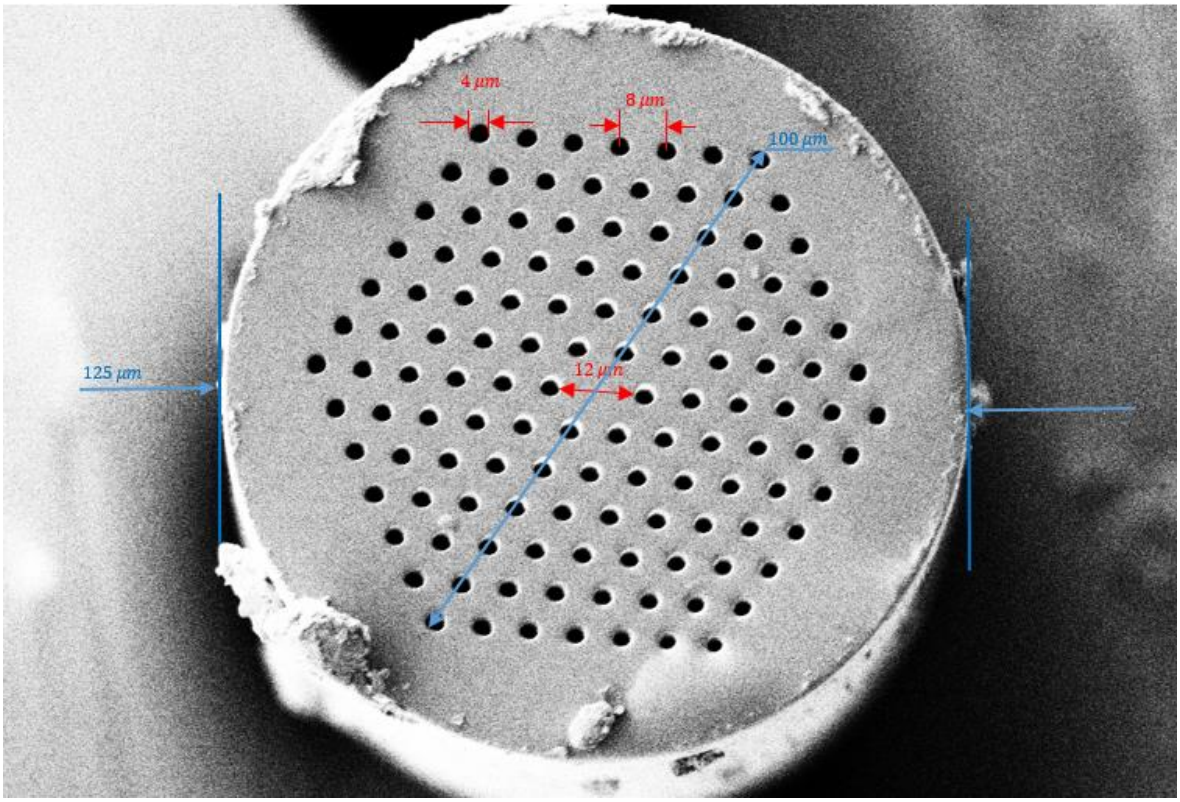

Figure 3.2: SEM image of a cross-section of solid core PCF (ESM-12-B)

Figure 3.2 shows the SEM (scanning electron microscopy) image of a typical commercially available solid core PCF with trade name ESM-12-B. The dimensions of its structural parameters measured and obtained are: diameter of core $(D_{core}) = 12\ \mu m$, diameter of cladding $(D_{cladding}) = 125\ \mu m$, pitch $(\Lambda) = 8\ \mu m$ and diameter of cladding air holes $(\mathrm{d}) = 4\ \mu m$.

PCFs normally have two modes of operation based on their light guiding technique – index guiding and bandgap guiding [28]. Index guiding PCFs operates similar to conventional optical fibres wherein light is confined within

the high index core by modified total internal reflection (M-TIR) principle [29]. However, bandgap PCFs guides light in the low index core region by the reflection from photonic crystal cladding [30]. Confinement loss and effective area are two important propagation characteristics of the PCF which can be tuned by altering their physical parameters like core diameter (ρ), cladding hole diameter (d) and pitch (Λ) in combination with the choice of material refractive index and type of crystal lattice [4,31].

Confinement or leakage loss (L_c) is the light confinement ability of the PCF within its core and can be calculated from the imaginary part of its effective refractive index [32].

$$L_c = \frac{\left(\frac{20}{\ln(10)}(2\pi)\right) \mathrm{Im}(n_{eff})}{\lambda} \quad (1)$$

where $\mathrm{Im}(n_{eff})$ is the imaginary part of effective refractive index, n_{eff} and λ is the propagating wavelength. Confinement loss depends on the transmission wavelength, PCF structure, size, shape, number of air holes and number of air hole rings.

Effective mode area (A_{eff}) is considered as the light carrying region of the PCF and is given by the equation [33-34]:

$$A_{eff} = \frac{\left[\iint_{-\infty}^{\infty} |E(x,y)|^2 \, dxdy\right]^2}{\iint_{-\infty}^{\infty} |E(x,y)|^4 \, dxdy} \quad (2)$$

where $E(x,y)$ is the electric field distribution.

Also, effective mode area is related to MFD by the equation [35]:

$$A_{eff} = k_n \left(\frac{\pi}{4}\right) MFD^2 = k_n \, \pi \, w^2 \quad (3)$$

where k_n is the correction factor and spot size, $w = MFD/2$.

Mode field diameter is approximated as,

$$\mathrm{MFD} \approx \frac{2}{\sqrt{\pi}} \sqrt{A_{\mathrm{eff}}} \tag{4}$$

3.3 Design and modeling of PCF using COMSOL Multiphysics

In PCF, the spatial variation of the index is orthogonal to the propagation direction with small holes having a different index of refraction than the rest of the fibre resulting in high degree of confinement of the waveguide mode.

The modeling of a solid core PCF using COMSOL Multiphysics software involves the following steps [36-37]:

1. Modeling of geometry: PCF structural design is carried out, choosing a hexagonal geometry and appropriate geometrical parameters like diameter (d) and spacing (Λ) of the air holes along the x- and y-axes.
2. Setting of physical parameters: Physical parameters such as wavelength of light and refractive index of materials used (silica and air holes) are specified using the Sellmeier's equation [37].
3. Initializing the mesh: The mesh size decides the level of details or the resolution
4. Compute solution: After initialising the mesh, the model is solved for the desired parameter (e.g. effective index of the fibre, effective refractive index of fundamental mode) using COMSOL's Finite Element Method (FEM).
5. Post-processing and visualization: Finally, additional parameters and results can be interpreted using the post-processing and visualization tools within COMSOL.

COMSOL Multiphysics which is a finite element analysis tool is used to analyse the structures in PCF with a huge possibilities of various holes shapes & arrangements. Moreover, the existence of high index contrast in the interfaces of host material and the rods/ air hole channels requires a software like COMSOL to model it [38-39].

The assumptions made for the model are: (a) the fibre consists entirely of homogenous material and (b) no sources of light exist inside the fibre, so that no free charges or currents exist inside the fibre.

The mode analysis is made on a cross-section in the *xy*-plane of the optical fibre. Each mode maintains its modal field distribution in the xy-plane, as the wave propagates in the *z* direction (the x, y, z coordinate frame can be understood from Figure 2.1). By modeling the cross-section, the field patterns of the propagation modes as well as the propagation constants can be calculated. However, this requires invariance in the out-of-plane direction.

As boundary condition along the outside of the cladding, the magnetic field is set to zero. Because the amplitude of the field decays rapidly as a function of the radius of the cladding, this is a valid boundary condition [36].

In the PCF, the cladding consisting of many number of air holes is looked upon as a single material, with its effective refractive index lying between the refractive indices of the individual materials (silica and air).

For a confined mode there is no energy flow in radial direction, thus the wave must be evanescent in the radial direction in the cladding [40]. This is true only if [36],

$$n_{eff} > n_2 \tag{5}$$

On the other hand, the wave cannot be radially evanescent in the core region.

Thus [36]:

$$n_2 < n_{eff} < n_1 \tag{6}$$

The waves are more confined when n_{eff} is close to the upper limit in this interval.

Furthermore, the effective mode index of a confined mode [36]:

$$n_{eff} = \frac{\beta}{k_0} \tag{7}$$

The effective index of the material is defined by the allowed mode with the highest effective index, also known as the Fundamental Space-filling Mode (FSM)

Normalised frequency for a fibre is defined as [36]:

$$V = \frac{2\pi a}{\lambda_0}\sqrt{{n_1}^2 - {n_2}^2} = k_0 a\sqrt{{n_1}^2 - {n_2}^2} \tag{8}$$

where *a* is the radius of the core of the fiber, β is the propagation constant and k_0 is the free-space wave number.

One of the main challenges in finite element modeling is how to treat open boundaries in radiation problems. The Wave Optics Module of COMSOL offers two closely related types of absorbing boundary conditions, the scattering boundary condition and the matched boundary condition. The former is perfectly absorbing for a plane wave, whereas the latter is perfectly absorbing for guided modes [36]. Here, the fibre with guided modes are analysed. So, the latter method is applied. A Perfectly Matched Layer (PML) is used in the model, which is not a boundary condition but an additional domain that absorbs the incident radiation without producing reflections. It provides good performance for a wide range of incidence angles and is not very sensitive [41].

3.4 Structural parameter dependence of fibre propagation characteristics

This section primarily investigates the effect of geometrical parameters on fibre parameters such as confinement loss and MFD, which plays a significant role in long distance fibre-optic remote sensing applications. The objective behind the study is to understand if microstructuring will enhance the electric field confinement, reduce losses and thereby increase the transmission signal intensity of the PCF based sensor. Furthermore, liquid crystal infiltrations are incorporated in the PCF sensor configuration, exploiting their optical properties for PBG based tighter mode confinements and wavelength tunability. Theoretical study conducted on the fibre sensor revealed that confinement loss and MFD can be reduced by properly optimising their structural parameters.

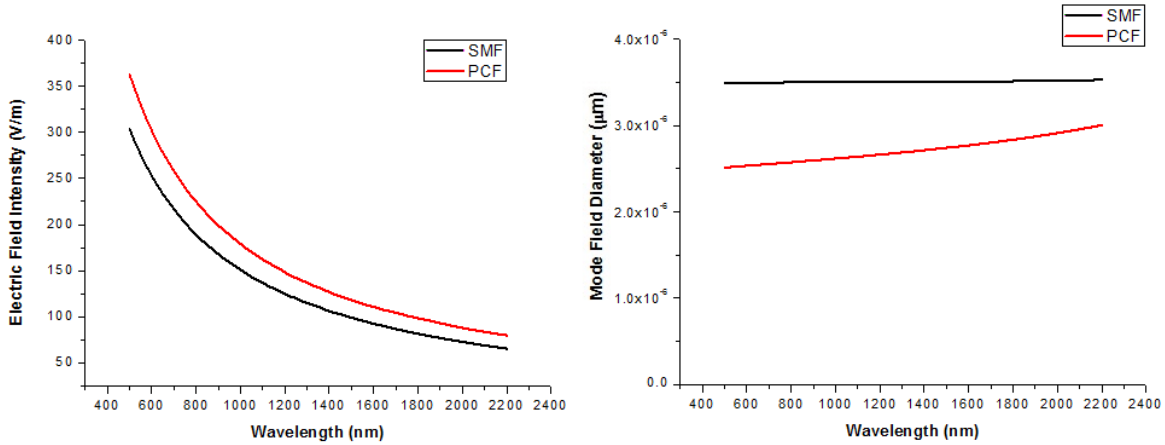

Figure 3.3: Comparison of SMF and PCF: (a) Electric field intensity vs Wavelength (b) MFD vs Wavelength

Figures 3.3 (a) and (b) show a comparison of PCF and SMF in terms of its electric field intensity and MFD for different operating wavelengths. For the analysis, dimensions of the core and cladding and the core-cladding refractive indices of the SMF and PCF were kept constant. The only varying parameter was the microstructuring of the cladding layer. The microstructured cladding had air

holes with diameter, d=1 μm and pitch, Λ=2 μm. As can be observed in Figure 3.3 (a), for the same input parameters assigned, PCF mode fields have higher electric field intensity compared to SMF. Furthermore, as shown in graph 3.3 (b), the MFD of PCF is obtained smaller than the SMF of same core size.

There are several sources of losses in fibres, such as structural imperfections, fibre bending, intrinsic material absorption, Rayleigh scattering, etc. Losses induced at the time of fabrication can be reduced by careful optimisation and monitoring of the fabrication process. Confinement loss is another major type of loss that occurs mainly in fibres fabricated from raw material [42]. Confinement loss which is also known as leakage loss is the leakage of power from the core into the cladding and it occurs mainly in single mode fibres. The guided modes of PCFs are inherently leaky, as the refractive index of core is the same as that of outer cladding without air-holes [43]. Theoretically, PCF with infinite number of air-holes in the cladding is expected to achieve lossless propagation. However, practically fabricated fibre experiences leaky modes due to finite number of air-holes in the photonic crystal cladding.

LCPCF sensors are based on the optical properties of the liquid crystal and have its index of refraction, n_{LC} as the sensing magnitude. LCPCF temperature sensor takes advantage of the temperature dependence of the liquid crystal permittivity, which makes it less susceptible to other external influences and also a lambda shift is experienced at the output as a result of changes in temperature [7].

Confinement losses in the sensor are studied as a function of normalised wavelength (λ/Λ) by varying its different geometrical parameters such as hole diameter, inter-hole spacing and number of air hole rings around the core. Moreover, the MFD which is related to optical field distribution in the fibre gives

a better idea of its loss characteristics. By optimising the structural parameters of PCF, confinement losses can be minimized which improves the strength of the signal and thereby the transmission distance and range of the fibre sensor. In the designed four ring LCPCF, refractive index of the background material, silica is taken as 1.45 and the airhole is infiltrated with liquid crystal materials, Cat No. *1550* (refractive indices n_o=1.461, n_e=1.522 at 22°C) and PCH-5 (refractive indices n_o=1.6049, n_e=1.4863 at 25°C) [44]. Considering O&G sensing environment, typical refractive index value of crude oil is 1.4785 and that of gasoline is in the range 1.42-1.44 [45]. For normal fuels, refractive index is a number bigger than one and normally lower than 1.7. However, for the fibre sensor configuration designed, O&G sensing medium has negligible effect on the strongly confined optical modes propagating through its core.

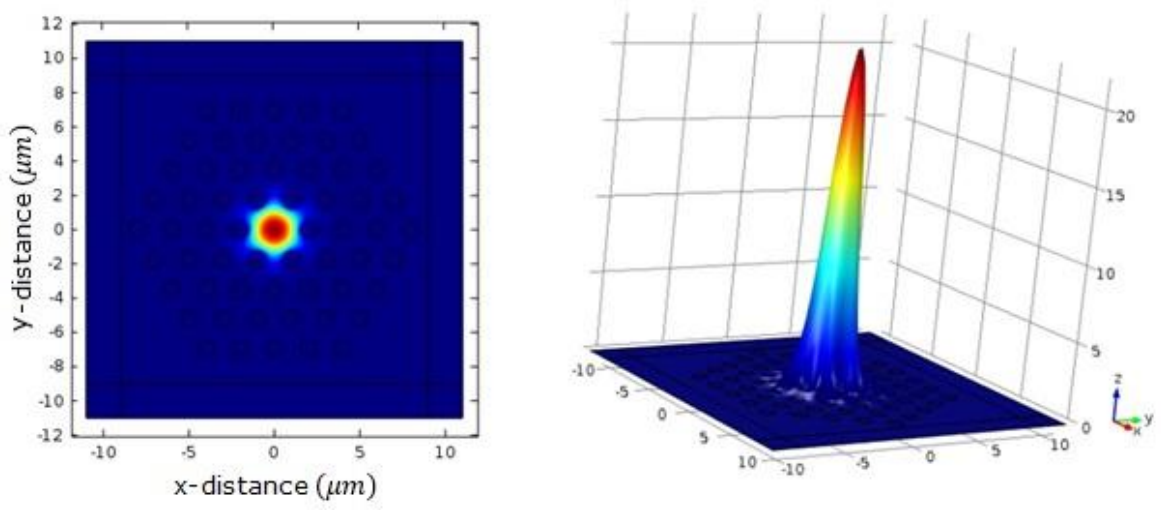

Figure 3.4: Electric field pattern 2D and 3D views for 4- ring LCPCF

Figure 3.4 shows the 2D and 3D views respectively of a Gaussian electric field pattern obtained for the four ring LCPCF. As can be observed from the figure, the guided light modes are strongly confined within the core without any leakages. A PML is introduced around the photonic crystal cladding, which acts as an additional domain to absorb incident radiations without producing back

reflections. The PML is made of an artificial absorbing material which has anisotropic permeability and permittivity that matches with the physical medium outside. With the addition of liquid crystals, the fibre exhibits the common properties of PBG i.e. only certain frequencies of light propagate through the core and all other wavelengths tends to pass through the cladding which has a higher refractive index [46].

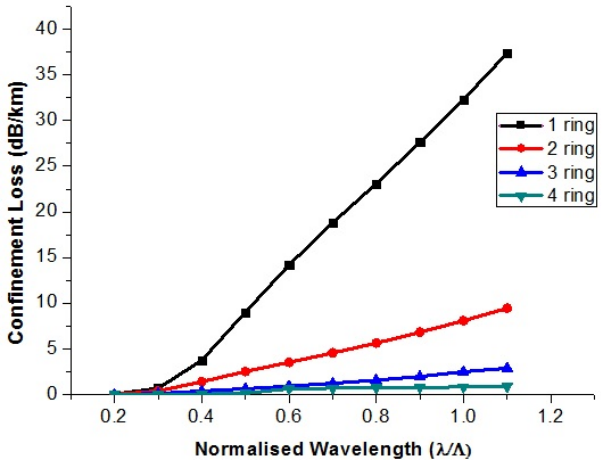

Figure 3.5: Confinement loss vs normalised wavelength for different number of hole rings

To understand the influence of air hole rings on the losses experienced by the PCF sensor different simulations were run. The number of air hole rings within the cladding, ranging from one to four were used for the simulation. As you can see from Figure 3.5, confinement loss decreases with increasing number of hole rings around the core. In the analysis, four ring structure showed minimum confinement loss which is due to the negligible field leakage. Figure 3.6 shows the variation in confinement loss (L) with respect to normalised wavelength (λ/Λ) for a liquid crystal filled PCF with $d/\Lambda=0.5$, $\Lambda=2$ μm, $d=1$ μm for different number of air hole rings in the cladding. For small values of d/Λ, the resultant losses can be higher unless sufficiently larger number of holes are introduced on to the PCF core.

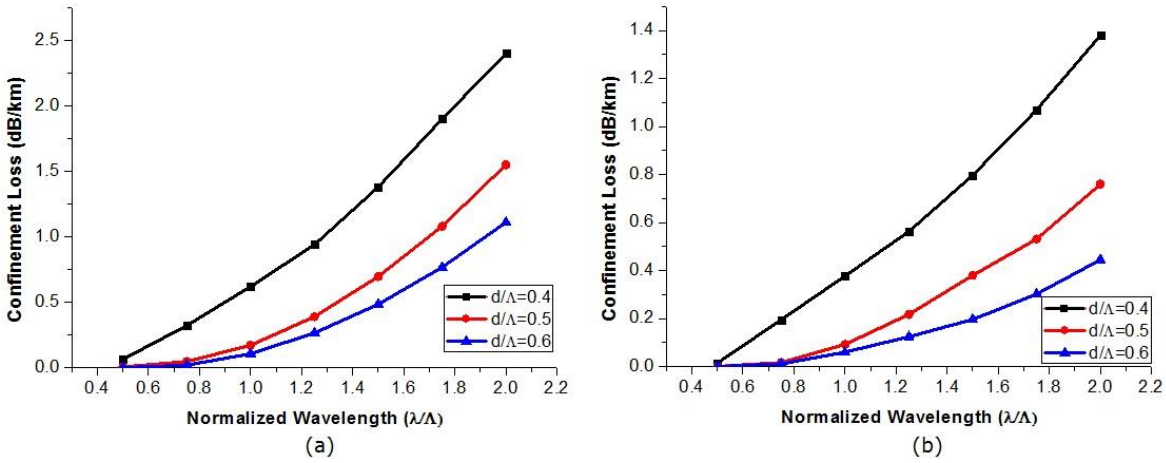

Figure 3.6: Confinement loss vs normalised wavelength for pitch: (a) Λ=1.5μm, (b) Λ=1.9μm

Further simulations were carried out on the designed PCF, to understand the influence of different air hole distributions which includes the effect of air hole diameter and spacing between the air holes on the confinement losses. Figure 3.6 (a) depicts the variation of confinement loss (L) with respect to normalised wavelength (λ/Λ) for different values of diameter to spacing ratio (d/Λ). The hole spacing (Λ) is kept constant at 1.5 μm and the diameter (d) is increased. It can be observed that the confinement loss as expected increases with wavelength (λ), but it tends to decrease with increasing diameter to spacing ratio (d/Λ). Similarly, Figure 3.6 (b) shows another plot of the confinement loss (L) with respect to normalised wavelength (λ/Λ) for a different spacing (Λ) 1.9 μm. Keeping the hole spacing constant, simulation is conducted for three structures (d/Λ= 0.4, 0.5, 0.6). It can be seen that confinement loss again increases with wavelength (λ) and also decreases with increase in d/Λ. Moreover, it is worth noting that confinement loss decreases with increasing spacing (Λ).

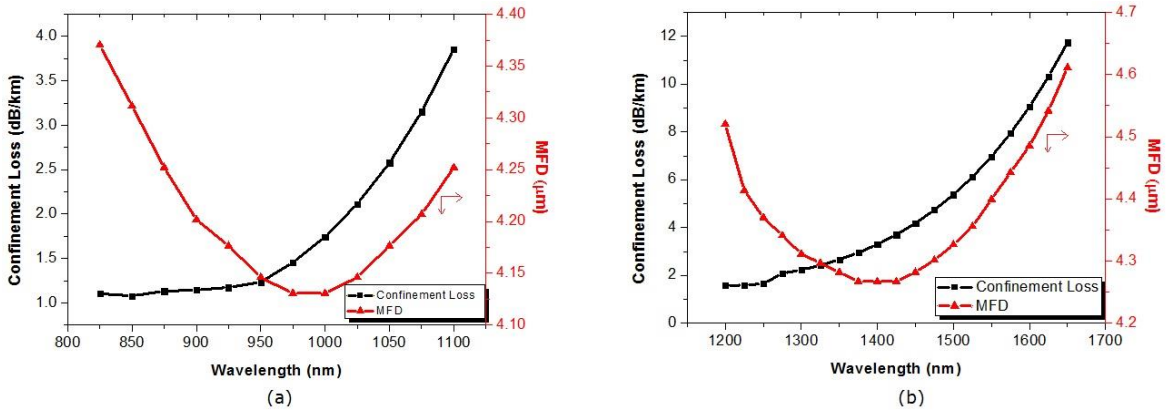

Figure 3.7: Confinement loss and MFD vs wavelength for LC refractive index: (a) n_{LC}=1.522, (b) n_{LC}=1.6049

Furthermore, to understand the effect of liquid crystal infiltrations on PCF propagation parameters like confinement wavelengths, confinement loss and MFD, the simulation was run by varying the liquid crystal materials infused into cladding holes of the PCF. Figures 3.7 (a) and (b) show the variation in confinement loss (in dB/km) and MFD (in μm) with respect to wavelength (in nm) for the PCF filled-up with liquid crystalline mixture, Cat No. 1550 (n_{LC}=1.522) and PCH-5 (n_{LC} =1.6049). For LCPCF infused with Cat No. 1550, single mode operation was possible for wavelengths in the range 825-1100 nm. It was observed that, below the short cut-off wavelength (825 nm) and beyond the long cut-off wavelength (1100 nm), the electric field leaks into the cladding region. However, compared to single mode fibres, PCFs exhibit tighter mode confinement over a wide range of wavelength and hence lower mode area is achieved. In both Figures 3.8(a) and (b), it can be seen that the MFD decreases up to a particular wavelength and then it increases. At low wavelengths, the power density is high, intensity is low and therefore the area transversed by the fibre is less. But at higher wavelengths the power density is low, intensity is high, therefore the effective mode area is also high.

From Figure 3.7 (a) and (b) it can be observed that, by changing the liquid crystal material infiltrated into the holes (PCH-5, n_{LC} =1.6049), the confinement wavelengths can be tuned to wavelength range 1200-1650 nm. Through the simulation it was identified that the photonic bandgap (bands which can guide light), shifts to longer wavelength with increase in liquid crystal refractive index. Also, within the bandgap, leakage losses are smaller compared to outside of the bandgap. The shift in the photonic bandgap, finds numerous applications in fibre-optic sensing, tunable filters and switches. Further simulations carried out by increasing the hole sizes also resulted in reduced mode area and confinement loss, which is due to tighter mode confinement. However, changing the number of air hole rings around the core did not show any variation in the effective area of the LCPCF as observed for confinement loss.

To sum up, tuning of fibre geometrical parameters leads to improvement in light confinement and attenuation reduction which in turn enhance the spatial coverage and accuracy of the fibre sensor. The designed optical fibre sensor with the mentioned improved capabilities and with the potential to perform multiple parameter sensing can effectively solve the limitations of existing sensors down-hole.

From the current theoretical investigation, it was identified that, structural parameters have significant effects on fibre parameters such as confinement loss, effective mode area and MFD. It was found that confinement loss is a strong function of air-filling fraction (d/Λ) and the number of rings employed in the LCPCF cladding. Investigations carried out by varying the hole size and inter-hole distance also resulted in reduction of leakage losses and MFD. Low confinement loss automatically results in improved signal power, which in turn improves the accuracy and spatial range of the sensor. Besides this, the tunability

of the photonic bandgap of the LCPCF by changing the liquid crystal material adds to its sensing capabilities. The present results shows promising future in the direction of PCF-FBG based long distance remote sensing system for O&G applications. Based on the investigation, their synergy will develop an advanced fibre-optic sensing system with longer sensing range and enhanced accuracy for condition monitoring of O&G fields in deeper zones.

3.5 Core nanostructuring and material infusion effects in PCF

This section investigates the effects of core nanostructuring and material infusions for the tuning of critical parameters of silica PCFs like operating wavelength, bandwidth, confinement loss and MFD. These parameters are very important in fibre optic sensing applications as it affects the sensitivity, range and spatial coverage of the sensor. Through the study carried out, a shifting and broadening of the PCF spectral bands was obtained by nanostructuring and infusing composite materials within the PCF.

The studies are carried out by changing the size (nano size holes in the core and micro size holes in the cladding), shape (circular, elliptical) and distribution of PCF air holes. In the previous study carried out, the designed solid core PCF exhibited limited operating wavelengths [47]. Hence, in order to achieve spectral shifting and bandwidth enhancement, core nanostructuring and also the effect of different liquid crystal materials infiltrations within the cladding holes are being investigated. PCF parameters such as confinement losses, effective area and MFD are studied as a function of normalised frequency (Λ/λ). MFD and effective area is associated with the electric field distribution within the fibre. Analysis of these parameters gives a better insight of the propagation characteristics of the PCF.

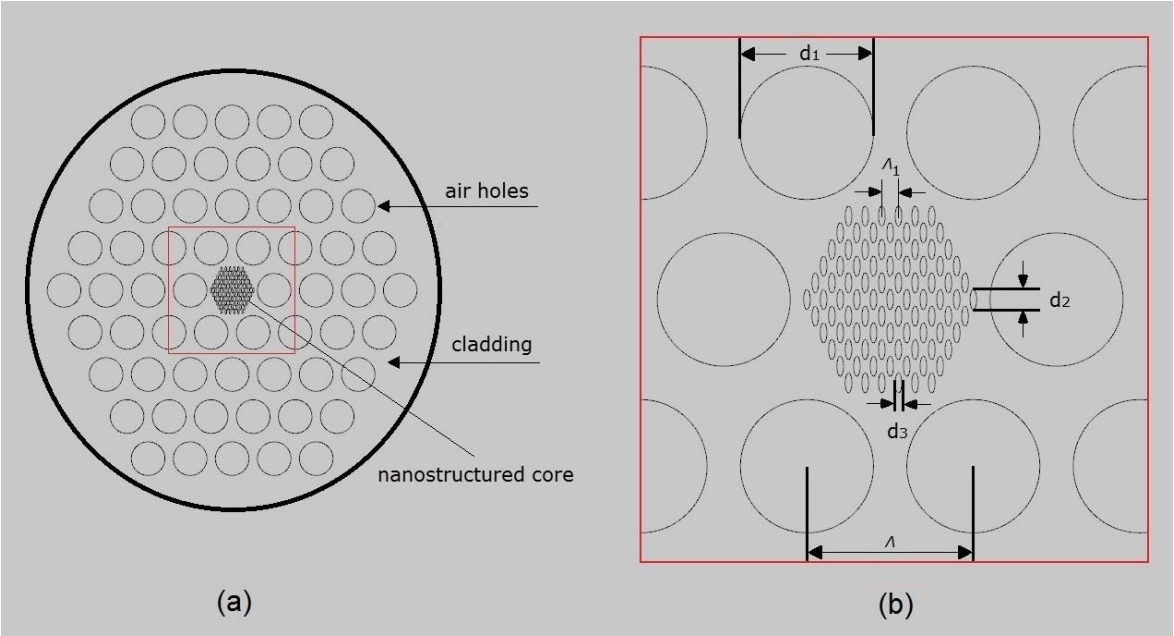

Figure 3.8: Cross section of: (a) designed nanostructured PCF and (b) nanostructured core zoomed view

Figures 3.8 (a) and (b) show the cross section of the designed nanostructured PCF with a four-ring hexagonal lattice of circular air holes in the cladding and a five ring array of elliptical air holes in the core. The geometrical parameters of the nanostructured PCF comprises of: pitch (Λ) which is the cladding hole center to center distance; d_1 is the diameter of the cladding air hole; d_2 and d_3 are the length of major axis and minor axis of the elliptical air holes within the core and Λ' is the hole to hole spacing between the elliptical air holes of core. The elliptical air holes introduce birefringence properties, which greatly improves the sensing capabilities of PCF.

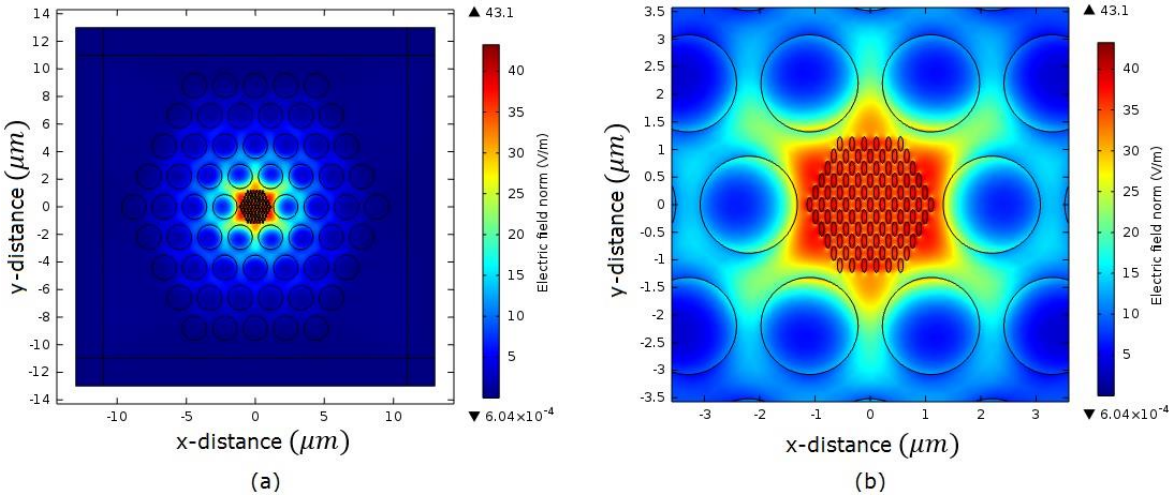

Figure 3.9: (a) Electric field mode profile of the nanostructured PCF, (b) Zoomed view of electric field mode profile in PCF core

Figures 3.9 (a) and (b) show the electric field profile of the fundamental mode obtained for the designed nanostructured PCF. The central core with red color indicates the region of highest electric field. From Table 3.1 it can be observed that the mode confinement wavelengths can be brought down from the infrared (IR) to the NIR wavelengths by tuning the physical parameters of the core and cladding air holes. NIR lower cut off wavelength of 925 nm was achieved for the nanostructured PCF with design parameters: $\Lambda = 1\,\mu m,\ d_1 = 0.8\,\mu m,\ \Lambda' = 100\,nm,\ d_2 = 60\,nm,\ d_3 = 20\,nm$.

Table 3.1: Confinement wavelengths with varying physical parameters

Sl. No.	Core dimensions	Cladding dimensions	Confinement wavelengths
1	$\Lambda' = 0.1\Lambda = 0.22\ \mu m = 220\ nm$ $d_2 = 0.6\Lambda' = 0.132\ \mu m = 132\ nm$ $d_3 = 0.2\Lambda' = 0.044\ \mu m = 44\ nm$	$\Lambda = 2.2\ \mu m$ $d_1 = 0.8\Lambda = 1.76\ \mu m$	≥ 1950 nm
2	$\Lambda' = 0.1\Lambda = 0.2\ \mu m = 200\ nm$ $d_2 = 0.6\Lambda' = 0.12\ \mu m = 120\ nm$ $d_3 = 0.2\Lambda' = 0.04\ \mu m = 40\ nm$	$\Lambda = 2\ \mu m$ $d_1 = 0.8\Lambda = 1.6\ \mu m$	≥ 1775 nm
3	$\Lambda' = 0.1\Lambda = 0.15\ \mu m = 150\ nm$ $d_2 = 0.6\Lambda' = 0.09\ \mu m = 90\ nm$ $d_3 = 0.2\Lambda' = 0.03\ \mu m = 30\ nm$	$\Lambda = 1.5\ \mu m$ $d_1 = 0.8\Lambda = 1.2\ \mu m$	≥ 1450 nm
4	$\Lambda' = 0.1\Lambda = 0.1\ \mu m = 100\ nm$ $d_2 = 0.6\Lambda' = 0.06\ \mu m = 60\ nm$ $d_3 = 0.2\Lambda' = 0.02\ \mu m = 20\ nm$	$\Lambda = 1\ \mu m$ $d_1 = 0.8\Lambda = 0.8\ \mu m$	≥ 925 nm

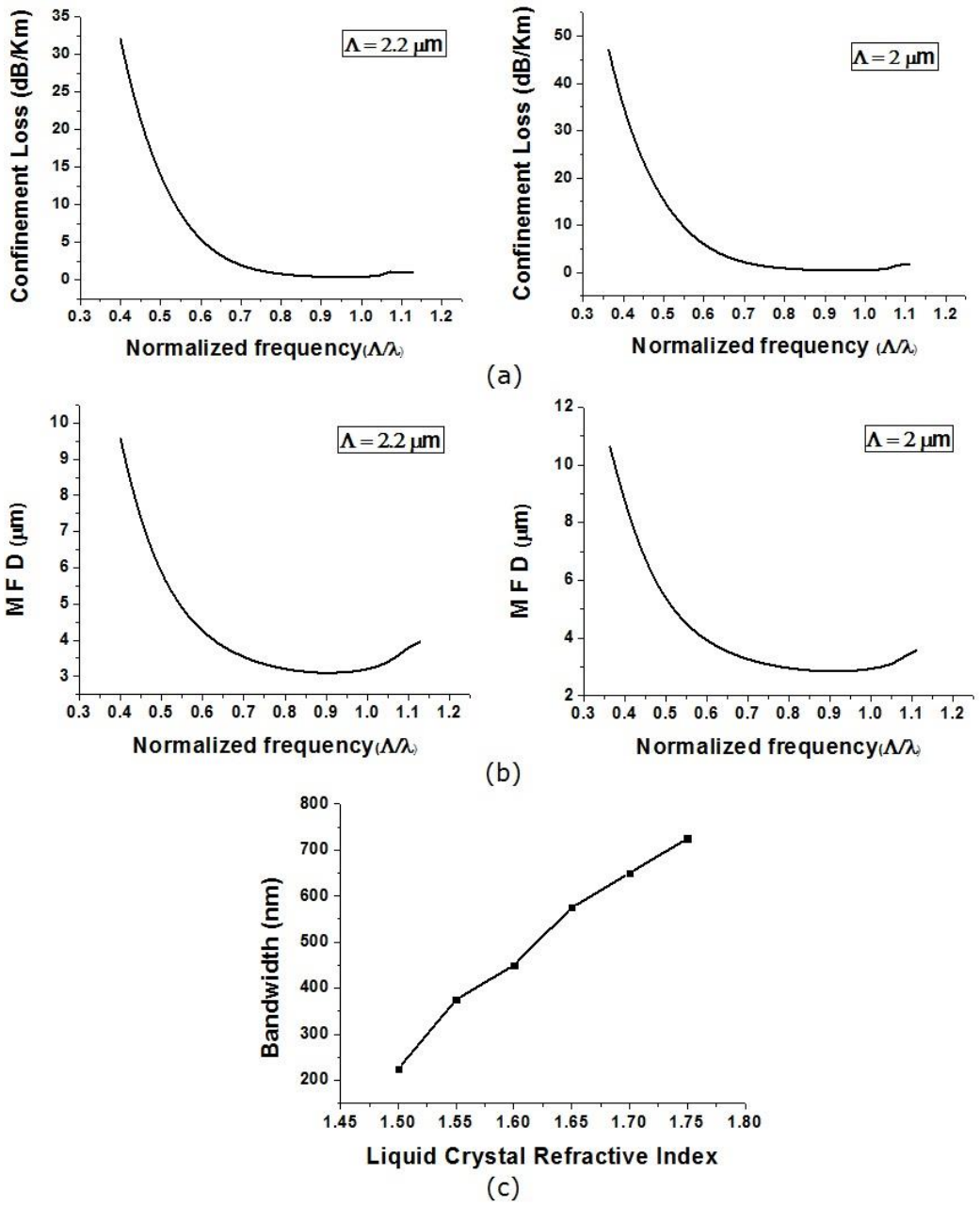

Figure 3.10: (a) Confinement loss vs normalised frequency for $\Lambda = 2.2\ \mu m$ and $\Lambda = 2\ \mu m$; (b) MFD vs normalised frequency for $\Lambda = 2.2\ \mu m$ and $\Lambda = 2\ \mu m$ and (c) Bandwidth vs liquid crystal refractive index

Figure 3.10 (a) depicts the variation in confinement loss (in dB/km) with respect to normalised frequency $(v = \Lambda/\lambda)$ for different pitch or cladding hole spacing. It can be observed that confinement loss decreases with normalised frequency or in other words confinement loss increases with wavelength. Another advantage of bringing down the mode confinement wavelengths from the IR to NIR wavelengths is a reduction in confinement losses. When confinement loss is

reduced, light gets more confined into the PCF core. Hence, the designed low confinement loss PCF returns stronger sensing signals when used in any sensor configuration. Figure 3.10 (b) shows the changes in MFD (in μm) with respect to normalised frequency for different pitch values. From the graph it is clear that MFD decreases with normalised frequency, or MFD experiences an increase for longer wavelengths and a decrease for shorter wavelengths. This is because, at lower wavelengths, the power density of the electric field propagating through the fibre would be higher and hence the effective mode area and MFD would be smaller [48].

Infiltrating different liquid crystal materials like K21 (refractive index, $n_{LC} = 1.732$), PCH-5 $(n_{LC} = 1.6049)$ and Cat No. 1550 $(n_{LC} = 1.522)$ into the cladding holes resulted in the shifting and widening of the PCF spectral bands. The confinement wavelengths achieved are: K21 (1650-2000 nm); PCH-5 (1200-1650 nm) and Cat No. 1550 (825-1100 nm). Hence, mode confinements in NIR wavelengths were achieved by infiltrating the holes with liquid crystal material Cat No. 1550. To sum up, PCF nanostructuring and liquid crystal material infiltrations, reduces its losses and enhances the PCF sensor transmission distance and coverage.

From Figure 3.10 (c), the changes in spectral bandwidth corresponding to different liquid crystal refractive indices value can be observed. It was observed that altering refractive index of liquid crystal material filled into the cladding holes of PCF resulted in an expansion and movement of its photonic bandgap. This feature can be utilised in designing PCFs of any required wavelengths specific to any particular application. Moreover, liquid crystal PCFs owing to their PBG guiding mechanism enables stronger light confinements facilitating sensing at longer distances.

The computational study carried out by nanostructuring the PCF core and by changing the size, shape and distribution of the PCF holes resulted in a shift in its spectral band, accompanied with a reduction in confinement losses and MFD. It was found that the PCF properties are a strong function of its structural parameters such as, size and spacing of the nanostructured air holes in the core and microstructured air holes in the cladding. Further simulations carried out by infusing different liquid crystal composite materials into the PCF resulted in a wavelength shift from IR to NIR. Moreover, altering refractive index of the liquid crystal material filled into the cladding holes of PCF caused a shifting and broadening of the photonic bands. Through these simulations it was identified that the spectral positions and bandgaps can be tuned by nanostructuring the PCF holes and changing its material infiltrations. Hence, nanostructuring and composite material infiltrations makes it possible to have different designer wavelengths possible for the PCF sensors. In addition, low confinement losses and MFD improves the signal power of the sensor, which in turn enhances its range and propagation distance. This study can be extended to MIR wavelengths giving scope for future fibre optic sensing and next generation communication applications.

3.6 Nanostructuring and rare earth doping effects in PCF

The literature review conducted in Chapter 2 revealed that, enhancing the refractive index of the core will improve the light confinement characteristics and guidance properties of the PCF [4]. One method to enhance core refractive index is through rare earth doping. Hence, this section investigates the effect of rare earth material doping on fibre optic sensor parameters like operating wavelength, effective refractive index, confinement loss, effective mode area

and electric field intensity. The doping effects are accommodated by changing the refractive index value of the core within the modelled nanostructured PCF. The studied parameters are critical in fibre optic sensing applications as it affects the range, spatial coverage and sensitivity of the sensor. Through the investigations carried out by periodic nanostructuring of the rare earth doped sensor, a shifting and broadening of the PCF spectral bands and also a reduction in the fiber confinement losses and MFD was achieved. Furthermore, optimal doping of the PCF with rare earth-silica composite material invokes photoluminescence characteristics within the fibre optic sensor.

Current investigations are carried out by changing the geometrical parameters and assigning refractive index of rare earth doped silica in the previously designed nanostructured PCF model [49] in order to tune its propagation characteristics and electric field confinements to suit photoluminescence sensing applications.

Simulations were conducted on the hexagonal lattice nanostructured PCF already designed, by changing its geometrical parameters and assigning refractive index value of various concentrations of Tb doped silicate glasses. Figure 3.11 (a) shows the electric field profile of the fundamental mode for 500 nm wavelength obtained on the rare earth doped nanostructured PCF. The red colour in the central core indicates the region of highest electrical field intensity (42 V/m). By optimising the structural parameters light mode confinements were achieved for visible wavelengths starting from 425 nm and covering the NIR wavelengths.

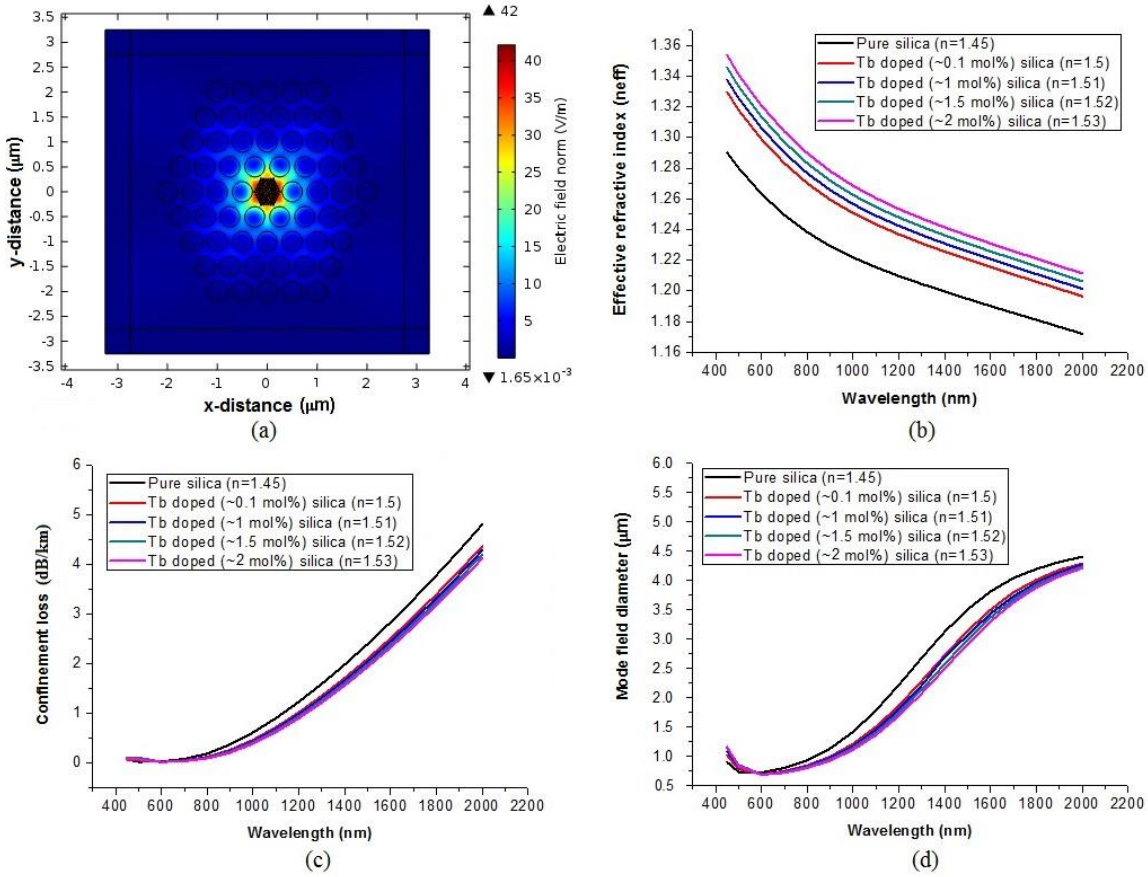

Figure 3.11: (a) Electric field mode profile of rare earth doped nanostructured PCF for 500 nm, (b) Effective refractive index vs wavelength and (c) Confinement loss vs wavelength and (d) MFD vs wavelength

Figure 3.11 (b) shows the variation in effective refractive index (n_{eff}) with respect to wavelength for undoped silica (refractive index, $n = 1.45$) and various concentrations (0.1 to 2 mol%) of Tb doped silica materials with refractive index in the range 1.50 to 1.53 [50] is used as the simulation parameters in the nanostructured PCF. The effective index of the fundamental core mode must be lower than the material forming the core, in order to give rise to a confined mode. For standard optical fibers, $n_{core} > n_{eff} > n_{cladding}$ must hold in order for the mode in the core to be oscillatory and for the modes in the cladding to be exponentially decaying [51]. From the graph, it can be seen that n_{eff} decreases with increasing wavelength.

Figure 3.11 (c) depicts the variation in confinement loss (in dB/km) with respect to wavelength for changes in refractive index corresponding to undoped and Tb doped silica. It can be observed that confinement losses increase with wavelength and also slightly decreases with rare earth doping. One main advantage of bringing down confinement losses is that, light gets more tightly confined into the core region, enabling stronger sensing signals from the rare earth doped fibre optic sensor configuration. Figure 3.11 (d) shows the changes in MFD (in μm) with respect to wavelength for refractive index changes resulting from rare earth doping of silica material. From the graph it can be observed that MFD initially decreases for shorter visible wavelengths and later experiences an increase for longer visible and NIR wavelengths. This is because, at lower wavelengths, the power density of the electric field propagating through the fibre would be higher and hence the effective mode area and MFD would be smaller.

Table 3.2: Confinement wavelengths for varying geometrical parameters

Sl. No.	Core dimensions	Cladding dimensions	Confinement wavelengths
1	$\Lambda' = 0.1\Lambda = 0.1\ \mu m = 100\ nm$ $d_2 = 0.6\Lambda' = 0.06\ \mu m = 60\ nm$ $d_3 = 0.2\Lambda' = 0.02\ \mu m = 20\ nm$	$\Lambda = 1\ \mu m$ $d_1 = 0.8\Lambda = 0.8\ \mu m$	≥ 925 nm
2	$\Lambda' = 0.1\Lambda = 0.05\ \mu m = 50\ nm$ $d_2 = 0.6\Lambda' = 0.03\ \mu m = 30\ nm$ $d_3 = 0.2\Lambda' = 0.01\ \mu m = 10\ nm$	$\Lambda = 0.5\ \mu m$ $d_1 = 0.8\Lambda = 0.4\ \mu m$	≥ 425 nm

From Table 3.2, it can be observed that the mode confinement wavelengths can be brought down from the NIR to visible wavelengths by tuning the physical parameters of the PCF core and cladding air holes. Visible wavelength lower cut off of 425 nm was achieved for the rare earth doped nanostructured PCF with design parameters: $\Lambda = 0.5\ \mu m,\ d_1 = 0.4\ \mu m,\ \Lambda' = 50\ nm,\ d_2 = 30\ nm,\ d_3 = 10\ nm$. Hence alteration of structural parameters of the rare earth doped

nanostructured PCF resulted in the expansion and shifting of its photonic bandgap to shorter wavelengths.

The computational study carried out on the rare earth doped nanostructured PCF by tuning its geometrical parameters induced a shift in its photonic band from NIR to visible wavelengths and also resulted in the reduction of confinement losses and MFD of the fibre sensor. Moreover, altering the refractive index of the rare earth-silica composite materials by optimising the rare earth concentration used in the PCF sensor improves its photoluminescence signature characteristics. To sum up, PCF nanostructuring and optimum rare earth material doping reduces the fibre losses, improves electric field intensity and thereby enhances the transmission distance and coverage of the rare earth doped photoluminescence sensor.

3.7 Summary

A detailed investigation is carried out on different techniques and approaches to enhance electric field confinements within the central core of the optical fibre, through restructuring of core and cladding, material infusions within air holes (modifying refractive index of microstructured cladding) and rare earth doping of microstructured fibres in order to improve the overall signal from the PCF based sensor. Results indicated that geometrical parameters have significant effects on PCF parameters such as confinement loss, effective mode area and MFD. The wavelength tunability feature and stronger mode confinements observed in PCFs infiltrated with liquid crystals finds many advanced sensing applications. Through liquid crystal infiltrations, mode confinement wavelengths were brought down from the communication window (1550 nm range) to the NIR wavelengths around 900 nm. Furthermore, core nanostructuring of the PCF

aided in the reduction of confinement losses and MFD. Also, the rare earth doping of the nanostructured PCF enabled to further bring down the light confinements to visible wavelengths. In addition to the wavelength tuning, an offshoot advantage of rare earth doping within PCF core is its enhanced electric field confinement and intensity improvement. Rare earth doped PCFs also opens up a new idea for the development of multimodal sensors utilising rare earth-based photoluminescence technique. The next chapter will look to investigations carried out on PCF-FBG sensor configuration for sensing multiple parameters from multiple locations as needed for the oil industry.

3.8 References

[1] Knight J, Birks T, Russell PSJ, Atkin D. All-silica single-mode optical fiber with photonic crystal cladding. *Optics Letters.* 1996; 21(19):1547-1549.

[2] Buczynski R. Photonic crystal fibers. *Acta Physica Polonica Series A.* 2004; 106(2):141-168.

[3] Knight JC. Photonic crystal fibres. *Nature.* 2003; 424(6950):847.

[4] Pinto AM, Lopez-Amo M. Photonic crystal fibers for sensing applications. *Journal of Sensors.* 2012; 2012.

[5] Dainese P, Russell PSJ, Joly N, Knight J, Wiederhecker G, Fragnito HL, et al. Stimulated Brillouin scattering from multi-GHz-guided acoustic phonons in nanostructured photonic crystal fibres. *Nature Physics.* 2006; 2(6):388.

[6] Woliński T, Ertman S, Lesiak P, Domański A, Czapla A, Dąbrowski R, et al. Photonic liquid crystal fibers—A new challenge for fiber optics and liquid crystals photonics. *Opto-Electronics Review.* 2006; 14(4):329-334.

[7] Li J, Gauza S, Wu S, Alkeskjold TT, Lægsgaard J, Bjarklev A. High dno/dT liquid crystals and their applications in a thermally tunable liquid crystal photonic crystal fiber. *Molecular Crystals and Liquid Crystals.* 2006; 453(1):355-370.

[8] Rajan G. *Optical fiber sensors: advanced techniques and applications.* CRC Press; 2015.

[9] Shephard JD, Urich A, Carter RM, Jaworski P, Maier RR, Belardi W, et al. Silica hollow core microstructured fibers for beam delivery in industrial and medical applications. *Frontiers in Physics.* 2015; 3:24.

[10] Schuster K, Unger S, Aichele C, Lindner F, Grimm S, Litzkendorf D, et al. Material and technology trends in fiber optics. *Advanced Optical Technologies.* 2014; 3(4):447-468.

[11] Tittel FK, Richter D, Fried A. Mid-infrared laser applications in spectroscopy. *Solid-state mid-infrared laser sources, Springer*. 2003; 458-529.

[12] Zhang Y. *Physical properties investigation of nanostructured materials and their applications.* University of California, Santa Cruz; 2008.

[13] Paquet C, Kumacheva E. Nanostructured polymers for photonics. *Materials Today.* 2008; 11(4):48-56.

[14] Chen D. Nanostructured Photonic Crystal Fiber with Ultra-high Birefringence. *International Symposium on Biophotonics, Nanophotonics and Metamaterials, IEEE.* 2006; 362-365.

[15] Nasilowski T, Lesiak P, Kotynski R, Antkowiak M, Fernandez A, Berghmans F, et al. Birefringent photonic crystal fiber as a multi-parameter sensor. *Proceedings of Laser & Electro-Optics Society.* 2003; :29-32.

[16] Wolinski T, Szaniawska K, Ertman S, Lesiak P, Domanski A, Dabrowski R, et al. Influence of temperature and electrical fields on propagation properties of

photonic liquid-crystal fibres. *Measurement Science and Technology.* 2006; 17(5):985.

[17] Cubillas AM, Lazaro JM, Conde OM, Petrovich MN, Lopez-Higuera JM. Gas sensor based on photonic crystal fibres in the 2v3 and v2 2v3 vibrational bands of methane. *Sensors.* 2009; 9(8):6261-6272.

[18] Shemshad J, Aminossadati SM, Kizil MS. A review of developments in near infrared methane detection based on tunable diode laser. *Sensors and Actuators B: Chemical.* 2012; 171:77-92.

[19] Sigrist MW. Mid-infrared laser-spectroscopic sensing of chemical species. *Journal of Advanced Research.* 2015; 6(3):529-533.

[20] Sorokina IT, Vodopyanov KL. *Solid-state mid-infrared laser sources,* Springer Science & Business Media; 2003.

[21] Dussardier B, Blanc W, Peterka P. Tailoring of the local environment of active ions in rare-earth-and transition-metal-doped optical fibres, and potential applications. *Selected Topics on Optical Fiber Technology.* IntechOpen; 2012.

[22] Ballato J, Ebendorff-Heidepriem H, Zhao J, Petit L, Troles J. Glass and process development for the next generation of optical fibers: A review. *Fibers.* 2017; 5(1):11.

[23] Naczynski DJ, Tan MC, Riman RE, Moghe PV. Rare earth nanoprobes for functional biomolecular imaging and theranostics. *Journal of Materials Chemistry B.* 2014; 2(20):2958-2973.

[24] Schartner EP, Tsiminis G, François A, Kostecki R, Warren-Smith SC, Nguyen LV, et al. Taming the light in microstructured optical fibers for sensing. *International Journal of Applied Glass Science.* 2015; 6(3):229-239.

[25] Johny J, Prabhu R, Fung WK. Numerical Investigation of Nanostructured Silica PCFs for Sensing Applications. *Journal of Materials.* 2017; 69(11):2286-2291.

[26] Guobin R, Zhi W, Shuqin L, Yan L, Shuisheng J. Full-vectorial analysis of complex refractive-index photonic crystal fibers. *Optics Express.* 2004; 12(6):1126-1135.

[27] Cucinotta A. Photonic Crystal Fiber: Theory and Fabrication. *Bentham Science.* 2012; :84-92.

[28] Pal BP. *Guided wave optical components and devices: Basics, technology, and applications.* Academic Press; 2010.

[29] Wehrspohn RB, Kitzerow H, Busch K. *Nanophotonic materials: Photonic crystals, plasmonics, and metamaterials.* John Wiley & Sons; 2008.

[30] Xiao L, Jin W, Demokan M. Photonic crystal fibers confining light by both index-guiding and bandgap-guiding: hybrid PCFs. *Optics Express.* 2007; 15(24):15637-15647.

[31] Ahmed K, Morshed M. Design and numerical analysis of microstructured-core octagonal photonic crystal fiber for sensing applications. *Sensing and Bio-Sensing Research.* 2016; 7:1-6.

[32] Tan X, Geng Y, Tian Z, Wang P, Yao J. Study of ultraflattened dispersion square-lattice photonic crystal fiber with low confinement loss. *Optoelectronics Letters.* 2009; 5(2):124-127.

[33] Miyagi K, Namihira Y, Razzak SA, Kaijage SF, Begum F. Measurements of mode field diameter and effective area of photonic crystal fibers by far-field scanning technique. *Optical Review.* 2010; 17(4):388-392.

[34] Rifat AA, Ahmed K, Asaduzzaman S, Paul BK, Ahmed R. Development of Photonic Crystal Fiber-Based Gas/Chemical Sensors. *Computational Photonic Sensors,* Springer. 2019; 287-317.

[35] Mortensen NA. Effective area of photonic crystal fibers. *Optics Express.* 2002; 10(7):341-348.

[36] Multiphysics C. Wave Optics Module Users Guide v. 4.3. 2 COMSOL AB. *Stockholm, Sweden.* 2013.

[37] Prabhakar G, Peer A, Kumar A, Rastogi V. Finite element analysis of solid-core photonic crystal fiber*. Students Conference on Engineering and Systems, IEEE*; 2012; 1-5.

[38] Arismar CS, Nobrega HE, Hernandez-Figueroa F, Di Pasquale F. PCFDT: An accurate and friendly photonic crystal fiber design tool. *Optik - International Journal for Light and Electron Optics.* 2008; 119(15):723-732.

[39] Franco MA, Hattori HT, Sircilli F, Passaro A, Abe NM. Finite element analysis of photonic crystal fibers. *Proceedings of the 2001 SBMO/IEEE MTT-S International Microwave and Optoelectronics Conference.* 2001; 1:5-7.

[40] Pryor RW. *Multiphysics modeling using COMSOL 4: a first principles approach.* Jones & Bartlett Publishers; 2009.

[41] Tabatabaian M. *COMSOL5 for engineers.* Stylus Publishing; 2015.

[42] Saitoh K, Koshiba M. Numerical modeling of photonic crystal fibers. *Journal of Lightwave Technology.* 2005; 23(11):3580.

[43] Pourmahyabadi M, Nejad 111SM. Numerical analysis of index-guiding photonic crystal fibers with low confinement loss and ultra-flattened dispersion by FDFD method. *Iranian Journal of Electrical and Electronic Engineering.* 2009; 5(3):170-179.

[44] Yeh P, Gu C. *Optics of liquid crystal displays.* John Wiley & Sons; 2010.

[45] Jones C. *Hydrocarbons: Physical Properties and their Relevance to Utilisation*, Jones & Ventus Publishing, 2010.

[46] Knight JC, Broeng J, Birks TA, Russell PSJ. Photonic band gap guidance in optical fibers. *Science (New York, N.Y.).* 1998; 282(5393):1476-1478.

[47] Johny J, Prabhu R, Fung WK. Investigation of structural parameter dependence of confinement losses in PCF–FBG sensor for oil and gas sensing applications. *Optical and Quantum Electronics.* 2016; 48(4):252.

[48] Billington R. Effective area of optical fibres-definition and measurement techniques.

[49] Johny J, Prabhu R and Fung WK. Computational study of nanostructured composite materials for photonic crystal fibre sensors. *IOP Conference Series: Materials Science and Engineering*: IOP Publishing. 2017; 195(1): 012012.

[50] Hoaksey A. *Terbium doped glasses: their optical properties and potential applications.* Doctoral dissertation, Durham University; 1975.

[51] Johny J, Shashidharan S, Sudheer SK, Kumar KS. Design and Simulation of a Radio over Fiber System with Chromatic Dispersion and Polarisation Mode Dispersion Compensation*. Symposium on Photonics and Optoelectronics*, IEEE 2012; 1-4.

4. INVESTIGATIONS ON FBG SENSORS ON MICROSTRUCTURED FIBRES

4.1 Introduction

Even though intensive researches have been carried out on specialised fibres like PCFs and FBG for many years, to the best of my knowledge, no work has been reported exploiting their synergy in O&G sensing applications. As discussed in the literature review conducted in Chapter 2, PCF-FBG integration opens up new possibilities in multi-parameter fibre-optic sensing, owing to their active control over light characteristics and mode confinements. PCF-FBG based sensor is capable of differentiating the effects of different parameters like temperature and strain [1]. Their combination can improve the overall performance of the sensor system in terms of power, energy scaling and discrimination of cross-sensitivities [2]. The multi-resonant peaks from the PCF-FBG sensor helps to attain multi-parameter measurement simultaneously, offering good stability and wide range of broadband tuning [3]. However, their integration results in a mismatch in their MFD, which in turn causes various types of losses such as confinement loss, scattering loss, etc.

This chapter concentrates on the sensing characteristics of PCF-FBG sensor combination with the objective to attain signal intensity enhancement, through different approaches like tuning of grating parameters and FBG sensor positioning. A detailed study was carried out on FBG sensors in Chapter 2, in order to identify its suitability for different sensing requirements of O&G industry like longer sensing range, multi-point multi-parameter sensing, avoidance of cross-sensitivity issues, etc.

Structural health and condition monitoring, where advanced sensing technologies are employed, is a vital element in offshore O&G sector. It plays a

crucial role in ensuring safe and efficient explorations in order to significantly enhance the productivity from ultra-deep oil fields. Currently, most of the subsea assets have almost reached their design lifetime, though considerable amount of untapped hydrocarbon reserves are still available. Consequently, structural integrity and maintenance of the deteriorated subsea structures has become very important considering its impact on the environment and O&G economy as a whole. Hence, in order to extend the life span of valuable subsea assets, there is an urgent need for improved and reliable condition monitoring systems for its infrastructures, with increased signal transmission length and enhanced spatial coverage to retrieve sensing data from deeper zones.

Precise placement and alignment of FBG sensors is a key requirement in sensor integration for accurate measurement, prior to securing them to the well bore structures [4]. Identifying the right position of FBG sensors with respect to pipeline axis is very important because the FBG sensors show highest sensitivity and records peak intensity at specific points [5]. This aids in the precise and accurate measurements of the physical parameters in long distance remote monitoring applications.

4.2 Theoretical Background

FBGs are reflective sensors inscribed within the core of the optical fibre with a periodic or aperiodic perturbation of effective refractive index [6]. FBGs are wavelength-dependent reflectors, as they reflect particular wavelengths of light and transmits the remaining ones. FBGs are constructed through the UV-written periodic modulation of the optical fibre's effective index of refraction [7-8].

The fundamental principle of FBG sensor depends on the Bragg condition which states that any changes in physical parameters such as pressure, temperature,

strain etc., modifies the refractive index or grating period of the fibre grating, which in turn changes the Bragg reflected wavelength correspondingly [7].

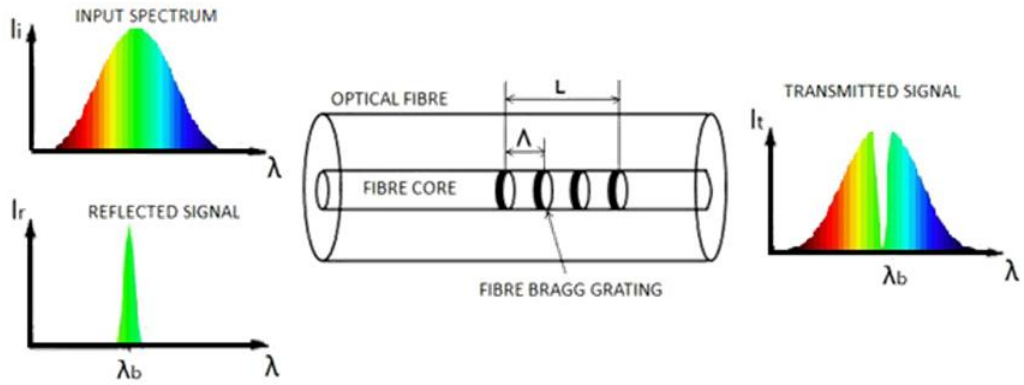

Figure 4.1: Detection principle of FBG sensor

Figure 4.1 illustrates the detection principle of FBG sensor. When a broad-spectrum of light is sent into the FBG sensor, reflections occur from each segment of alternating refractive index (gratings). These reflections interfere constructively only for a specific wavelength of light, known as the Bragg wavelength (λ_b). This effectively causes the FBG to reflect a specific wavelength of light while transmitting all others.

4.3 Modelling of FBG

Both in PCF and FBG a spatial change in the refractive index is simulated. In contrast to PCF, the FBG has an index of refraction that changes along its propagation direction. This results in a reflection at a particular wavelength and bandwidth which is determined by the geometry and material properties of the Bragg grating.

Theoretical modelling of FBG will help in understanding the grating parameters and their relation to optical pulse properties like amplitude and spectral width. FBG modelling using COMSOL Multiphysics software would require 3D simulations to accommodate its effective refractive index differences along the

propagation direction. Owing to the complexity of the larger 3D models, the memory and time requirements of the iterative solver would be higher compared to the 2D cross-sectional modelling. Hence for simplicity, modelling and characterisation of the fibre grating was conducted by solving the coupled mode equations using the transfer matrix method in MATLAB software [9-11]. MATLAB based simulations were conducted to analyse the effects of different grating parameters and the influence of techniques like chirping and apodisation on the FBG reflectivity spectrum. FBG sensors are designed to reflect certain wavelengths of light, which experiences a shift in wavelength upon sensing various physical parameters.

The basic principle of FBG sensor relies on the Bragg condition. So, any changes in physical parameters like temperature, strain, polarization, etc., alters the refractive index or grating period of the fibre grating, which will change the Bragg wavelength correspondingly. The incident wave gets coupled to the same counter propagating wave and thus it gets reflected. The Bragg reflected wavelength [7] is given by:

$$\lambda_b = 2.n_{eff}.\Lambda_g \quad (1)$$

where n_{eff} is the effective refractive index and Λ_g is the period of the grating or spatial period.

As discussed in the literature review conducted in Chapter 2, the O&G industry require multiple sensors for sensing various parameters from multiple locations. The main factor deciding the number of FBG sensors that can be designed on the optical fibre is the wavelength window. As the optical spectrum is limited, hence to accommodate more number of FBG sensors on the same optical fibre is to reduce the spectral width of its reflected signal. Furthermore, to improve the SNR of the PCF-FBG sensor configuration, the amplitude of the FBG

reflectivity signal need to be increased. Hence the following section will look into different investigations carried out on the FBG for reflectivity-bandwidth optimisation.

4.3.1 Investigations on Uniform FBGs

Uniform FBGs are those which have a constant period and constant peak amplitude of refractive index variation throughout the length of the FBG. Consider an FBG with spatial period Λ_g and length L_g. Suppose there are two identical modes propagating in opposite direction and let R and S represent the amplitude of forward and counter propagating mode respectively. The amplitudes of the forward and backward waves are governed by the coupled differential equations [11] given by:

$$\frac{dR}{dz} = i\,\hat{\sigma}\,R(z) + i\,k\,S(z) \tag{2}$$

$$\frac{dS}{dz} = -i\,\hat{\sigma}\,S(z) - i\,k^{*}\,S(z) \tag{3}$$

where z represents the position of the grating and k represents the AC (associated coupling) coefficient [11-12] and is given by:

$$k = \frac{\pi}{\lambda}.\Delta n_{eff}.v \tag{4}$$

where, v is the fringe visibility.

DC (Demi Coupling) coefficient [11-12] is given by,

$$\sigma = \frac{2\pi}{\lambda}.\Delta n_{eff} \tag{5}$$

Tuning parameter, $$\delta = 2\pi.n_{eff}\left[\frac{1}{\lambda} - \frac{1}{\lambda_d}\right] \tag{6}$$

$$\hat{\sigma} = \delta + \sigma \tag{7}$$

where λ_d is the design wavelength and n_{eff} is the effective refractive index.

The amplitude and power reflection coefficients [13-14] respectively can be shown as:

$$\rho = \frac{-k \sinh(\sqrt{k^2 - \hat{\sigma}^2}L)}{\hat{\sigma} \sinh(\sqrt{k^2 - \hat{\sigma}^2}L) + i\sqrt{k^2 - \hat{\sigma}^2} \cosh(\sqrt{k^2 - \hat{\sigma}^2}L)} \quad (8)$$

$$R = \frac{sinh^2(\sqrt{k^2 - \hat{\sigma}^2}L)}{cosh^2\left(\sqrt{k^2 - \hat{\sigma}^2}L\right) - \frac{\hat{\sigma}^2}{k^2}} \quad (9)$$

The reflectivity curves are studied as a function of normalised wavelength (λ/λ_{max}) using MATLAB. For Bragg scattering condition, λ_d is taken as 1550 nm and n_{eff} is taken as 1.45 [11].

$$\lambda_{max} = \left[1 + \frac{\Delta n_{eff}}{n_{eff}}\right].\lambda_d \quad (10)$$

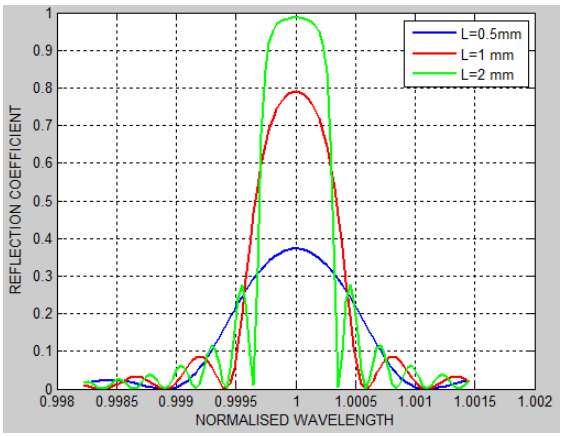

Figure 4.2: Reflectivity curve of FBG with different grating lengths

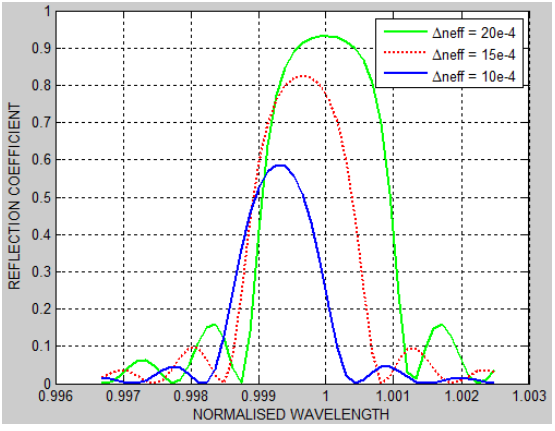

Figure 4.3: Reflectivity curve of FBG with different refractive index change

From Figures 4.2 and 4.3, it is obvious that the reflection coefficient increases with increase in refractive index change and grating length. However, the side lobe strength also gets increased with an increase in grating length. Hence a uniform period, index-modulation grating ('top hat') will definitely produce side lobes [10]. Therefore, there needs to be a tradeoff between the reflectivity and power loss in the side lobes in order to improve the range of the sensor.

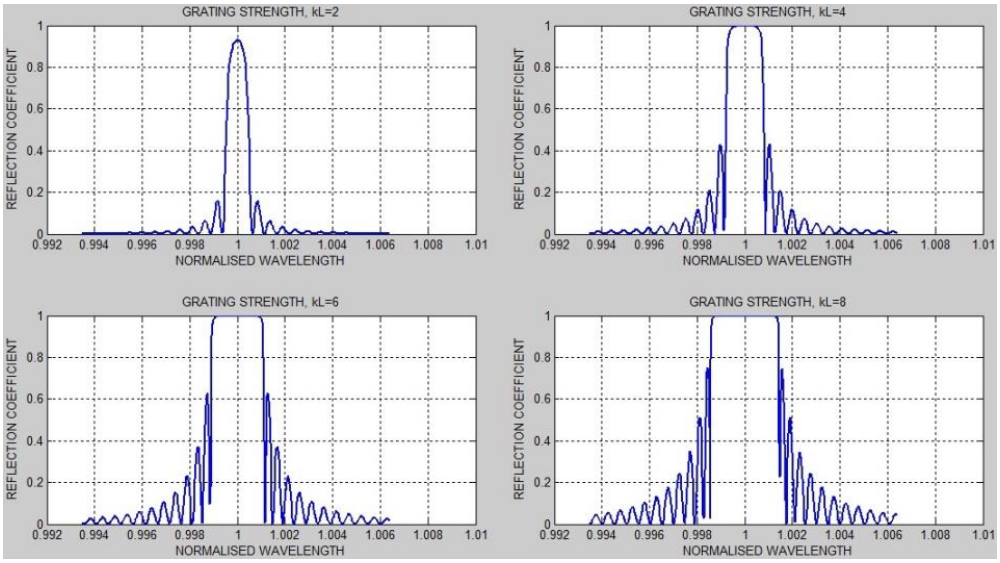

Figure 4.4: Reflectivity curve of FBG with different grating strengths (kL = 2,4,6 and 8 ; Δn_{eff}= 1e-4 ; L_g= 1mm)

Figure 4.4 shows the power reflectivity curve for uniform gratings with different coupling constants plotted versus normalised wavelength (λ/λ_{max}). When the number of grating periods, $N = L_g/\Lambda_g$ is larger or smaller, the reflection coefficient and width would be narrower or broader, respectively, for a given value of kL [11]. From Figure 4.4, it can be observed that with decrease in grating strength (kL), the spectral width also gets reduced.

Simulation results have shown that the grating parameters like effective refractive index, grating length and grating strength have significant effects on the amplitude and spectral width of the FBG sensor. So, by using an FBG of

properly optimised parameters a perfect reflection of the signal can be obtained from the FBG.

4.3.2 Investigations on Non-Uniform FBGs

Uniform FBGs had issues like higher side lobes associated with its reflectivity spectra. These side lobe characteristics are attributed to residual multiple reflections at the grating ends [15]. The main advantage of non-uniform grating is that it allows for the optical properties of the fibre to be changed by varying the effective refractive index or the grating period, along the length of the fibre axis. So, by using a complex refractive index profile or grating pitch variation, the frequency response of the FBG can be tailored to meet the desired superior performance. Depending on the variation in grating period and refractive index profile, non-uniform gratings are of two types: chirped and apodised gratings [15].

A chirped Bragg grating has a varying grating period. It can be created by two approaches: one is by changing the Bragg period and other is by changing the refractive index along the propagation direction of the fibre, which both has ultimately the same effect on the grating [16]. Chirping technique improves the spectral response, as multiple wavelengths are reflected from different grating positions [17].

The linear chirp phase term is given by [11]:

$$\frac{1}{2}\frac{d\phi}{dz} = -\frac{4\pi n_{eff} z}{{\lambda_d}^2}\frac{d\lambda_d}{dz} \tag{11}$$

where, chirp $d\lambda_d/dz$ is the rate of change of design wavelength with respect to grating position, which is expressed in nanometres/centimetres.

A non-uniform fibre Bragg grating is considered as splitting a uniform fibre Bragg grating into many sections along the fibre, through which the incident light waves are propagated. The uniform section, i is described by transfer matrix [11]:

$$F_i = \begin{bmatrix} \cosh\ (\gamma_B \Delta z) - i\frac{\hat{\sigma}}{\gamma_B} \sinh\ (\gamma_B \Delta z) & -i\frac{k}{\gamma_B} \sinh\ (\gamma_B \Delta z) \\ i\frac{k}{\gamma_B} \sinh\ (\gamma_B \Delta z) & \cosh\ (\gamma_B \Delta z) + i\frac{\hat{\sigma}}{\gamma_B} \sinh\ (\gamma_B \Delta z) \end{bmatrix} \quad (12)$$

where Δz is length of ith uniform section and $\hat{\sigma}$ and k are local values in the ith section and

$$\gamma_B = \sqrt{k^2 - \hat{\sigma}^2} \quad (13)$$

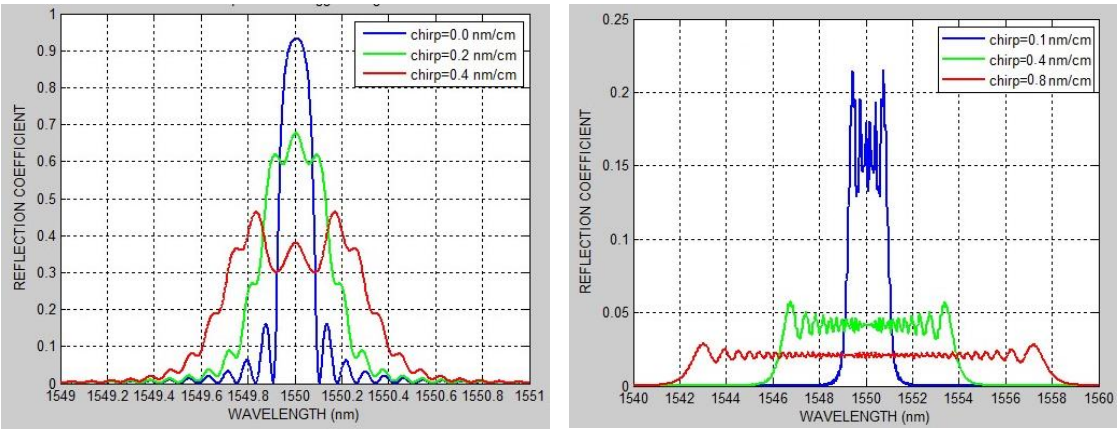

Figure 4.5: Reflectivity curve of chirped FBG

Figure 4.5 shows the different reflection spectra obtained for different chirp values ($d\lambda_d/dz$) 0.0, 0.2, 0.4, 1.0, 4.0 and 8.0 nm/cm respectively. In these simulations the gratings are assumed to be 10 mm long with a uniform refractive index change ($\Delta n_{eff} = 1 \times 10^{-4}$). From the reflectivity curve of chirped grating it can be observed that by increasing the chirp value, the side lobes get suppressed. However, with increasing chirp value, a reduction in the maximum reflectivity of the grating as well as broadening of the spectra can be observed.

These issues can be addressed by increasing the index of refraction modulation and grating length [18].

Apodisation is the process of varying the refractive index modulation depth along the length of the grating. This approach suppresses the side lobes and thereby smoothen the reflectivity curve of the grating. Apodisation can significantly diminish the reflectivity of side lobes which in turn allows the isolation of adjacent channels [19]. Consequently, adjacent channel separation also reduces cross-sensitivities induced by crosstalks.

There are several most commonly used functions, which can be used as apodisation profiles. Few of the apodisation profiles are as follows [20]:

a) raised sine profile,

$$f(z) = sin^2\left(\frac{\pi z}{L_g}\right), \qquad 0 \leq \mathrm{z} \leq L_g \tag{14}$$

b) sine profile,

$$f(z) = sin\left(\frac{\pi z}{L_g}\right), \qquad 0 \leq \mathrm{z} \leq L_g \tag{15}$$

c) sinc profile,

$$f(z) = \frac{\sin(x)}{x}, \qquad x = \frac{2\pi\left(z - \frac{L_g}{2}\right)}{L_g}; \quad 0 \leq \mathrm{z} \leq L_g \tag{16}$$

d) positive-tanh profile,

$$\begin{aligned} f(z)) &= tanh\left[\frac{2az}{L_g}\right], \qquad 0 \leq \mathrm{z} \leq \frac{L_g}{2} \\ &= tanh\left[\frac{2a(L_g - z)}{L_g}\right], \qquad \frac{L_g}{2} \leq \mathrm{z} \leq L_g \end{aligned} \tag{17}$$

e) Blackman profile,

$$f(z) = \frac{1 + 1.19\cos(x) + 0.19\cos(2x)}{2.38} \tag{18}$$

$$x = \frac{2\pi\left(z - \frac{L_g}{2}\right)}{L_g}; \quad 0 \leq z \leq L_g$$

f) Gaussian profile,

$$f(z) = exp\left[-4\left(\frac{z - \frac{L_g}{2}}{L_g}\right)^2\right] \tag{19}$$

where, z is the position of the grating, L_g is the grating length [21].

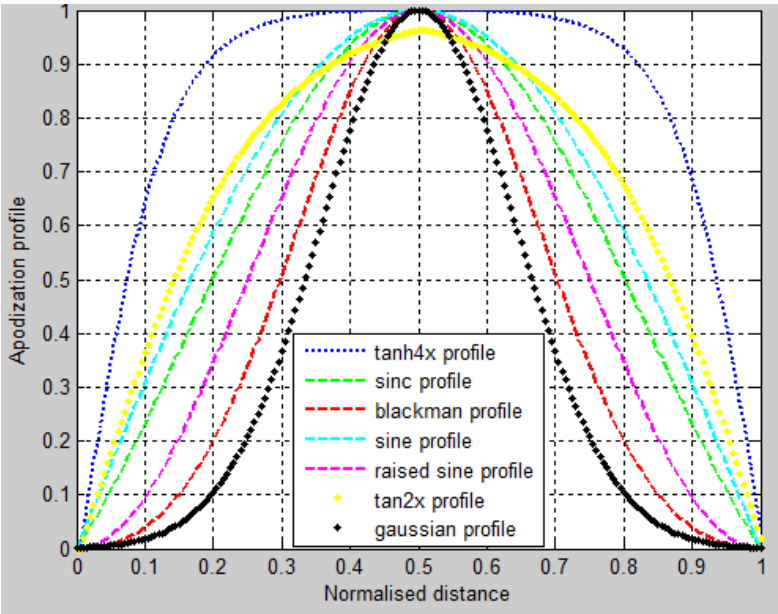

Figure 4.6: Apodisation profiles

For each profile an apodisation parameter, a_{eff} can be defined, with an unapodised grating having apodisation parameter value 1. The value of a_{eff} for raised sine, sinc, sine and positive tanh (a=4) profiles are 0.5, 0.589, 0.636 and 0.826 respectively [20]. The smaller the value of a_{eff}, the tighter would be its apodisation profile.

g) Raised cosine profile [16] is given by:

$$f(z) = \alpha\left(1 + cos\left[\frac{\pi\left(z - \frac{L_g}{2}\right)}{L_g}\right]\right) \tag{20}$$

where, α is the raised-cosine parameter or roll-off factor.

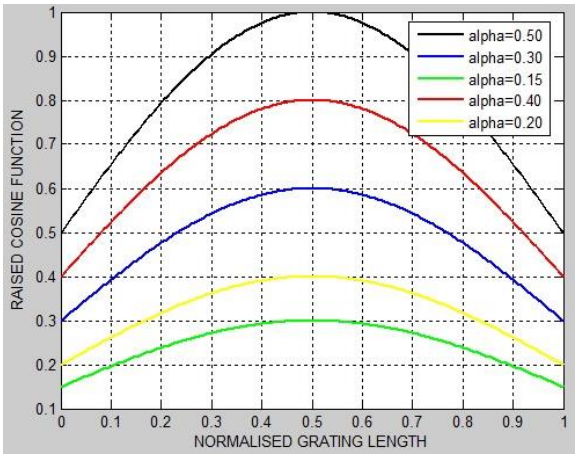

Figure 4.7: Raised cosine apodisation profile for different alpha values

Figure 4.7 is the plot of raised cosine modulation function. It can be observed that, with an increase in raised cosine parameter (α), the amplitude of the reflectivity curve and its spectral bandwidth response also increases.

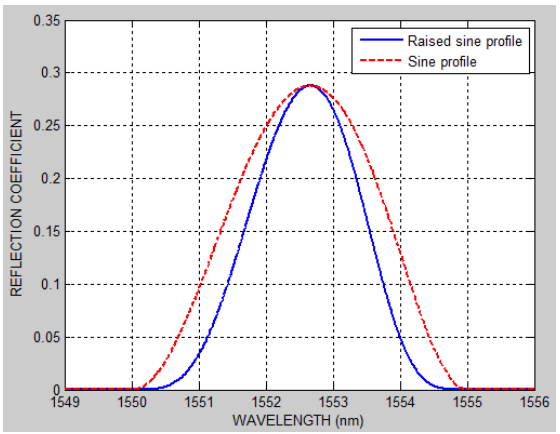

Figure 4.8: Sine and Raised sine apodisation applied to chirped FBG

Figure 4.8 demonstrates the effect of apodisation on a linearly chirped grating of fixed length and fixed refractive index modulation depth. The length of the grating is taken as, L_g= 5 cm and number of gratings, N=200. Other parameters are: design wavelength, λ_d = 1550 nm, effective refractive index, n_{eff} = 1.45, modulation depth, $\Delta n_{eff} = 10^{-4}$ and chirp value = 0.5 nm/cm.

4.4 Theoretical investigations on FBG temperature and strain sensitivities

Shift in Bragg wavelength due to temperature change is given by [18-22]:

$$\frac{\Delta\lambda_b(T)}{\lambda_b} = (\alpha + \xi)\Delta T \tag{21}$$

where, $\alpha = \frac{1}{\Lambda_g}\frac{\partial\Lambda_g}{\partial T}$ is the thermal expansion coefficient, $\xi = \frac{1}{n_{eff}}\frac{\Delta n_{eff}}{\partial T}$ is the thermo-optic coefficient and ΔT is the change in temperature.

Fractional change in Bragg wavelength for applied strain $\left(\varepsilon = \frac{\Delta\Lambda_g}{\Lambda_g}\right)$ is given by [18-22]:

$$\frac{\Delta\lambda_b(\varepsilon)}{\lambda_b} = (1 - \rho_e)\Delta\varepsilon \tag{22}$$

where ρ_e is the photo-elastic coefficient and $\Delta\varepsilon$ is the variation in strain value.

When temperature and strain both simultaneously acts on a fibre grating [18-22], their effects are additive. And Bragg wavelength change is given by:

$$\frac{\Delta\lambda_b(T,\varepsilon)}{\lambda_b} = (\alpha + \xi)\Delta T + (1 - \rho_e)\Delta\varepsilon \tag{23}$$

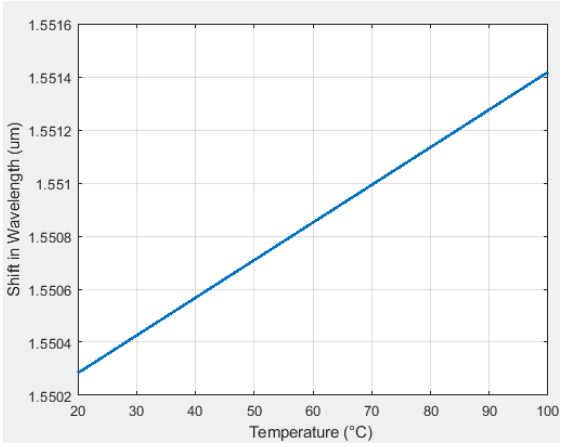

Figure 4.9: FBG temperature sensitivity graph

Figure 4.9 shows the FBG temperature sensitivity graph, which is the plot of shift in Bragg wavelength to temperature change. FBG temperature sensitivity factor calculated theoretically varies linearly with applied strain.

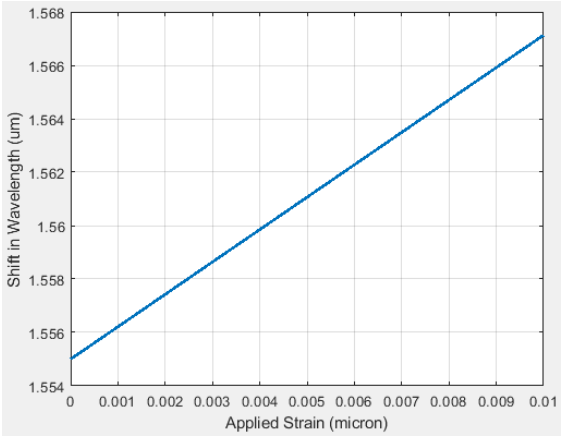

Figure 4.10: FBG strain sensitivity graph

Figure 4.10 shows the FBG strain sensitivity graph, which is the plot of shift in Bragg wavelength and change in applied strain. FBG strain sensitivity factor calculated theoretically varies linearly with applied strain. The strain sensitivity of FBG occurs mainly due to the compression and expansion of its grating period and also the strain-optic effect; which is defined as the strain-induced change in glass refractive index [23]. For experimental evaluation of FBG strain sensitivity, cantilever vertical displacement due to load is considered, which is again directly proportional to applied strain.

4.5 Experimental analysis of FBG sensors

Experimental analysis of FBGs were carried out to understand its response to different sensing modalities like temperature, strain, acoustic signal, etc. Experiments were carried out using high wavelength resolution, high dynamic range instruments like Optical Spectrum Analysers (OSA) and broad band light sources, in order to characterise the FBGs. OSAs measure optical power spectra typically over the wavelength range of 600 to 1750 nm, achieving a spectral resolution of approximately 0.01 nm. Optical spectrum gives information about the features of the grating and also the shift in wavelength with changes in physical parameters.

Based on the identified optimal grating parameters through simulation, suitable FBGs (>80% reflectivity, polyamide coated for high temperature conditions suiting O&G applications) were procured for conducting the experimental analysis and sensor development. Experiments were then carried out on the polyimide coated FBG sensor to characterise its response to different forms of strains and temperature and also to analyse it performances. Generally, performance of any sensor is defined by parameters like linearity, sensitivity, reversibility and hysteresis, repeatability, accuracy, range, response time, etc.

4.5.1 FBG Temperature Analysis

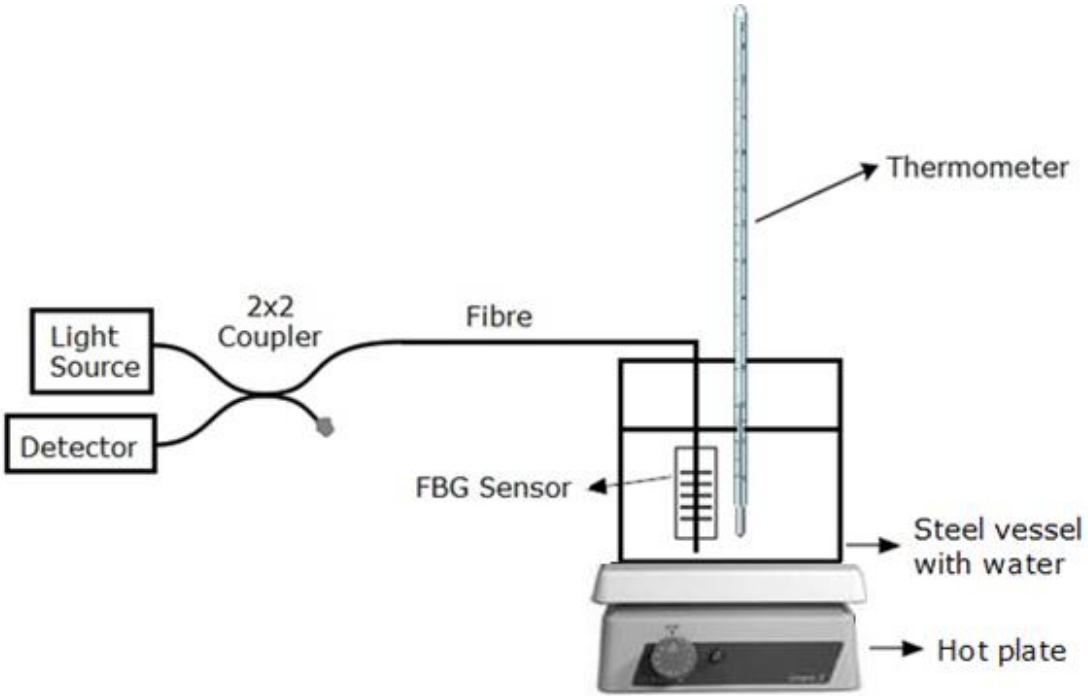

Figure 4.11: Pictorial view of experimental setup for temperature sensing

Figure 4.11 shows the laboratory setup used for calibration of FBG temperature sensor. Here the sensor is submerged in water (at 19 °C), which is then heated on a hotplate until it boils (up to 100°C). The optical fibre containing the FBG sensor was submerged in water, and the available pigtail was connected down

to the output port of the fibre coupler. The input ports were connected to the broad band light source as well as the OSA which acts as the detector for the reflected signals from the FBG sensors.

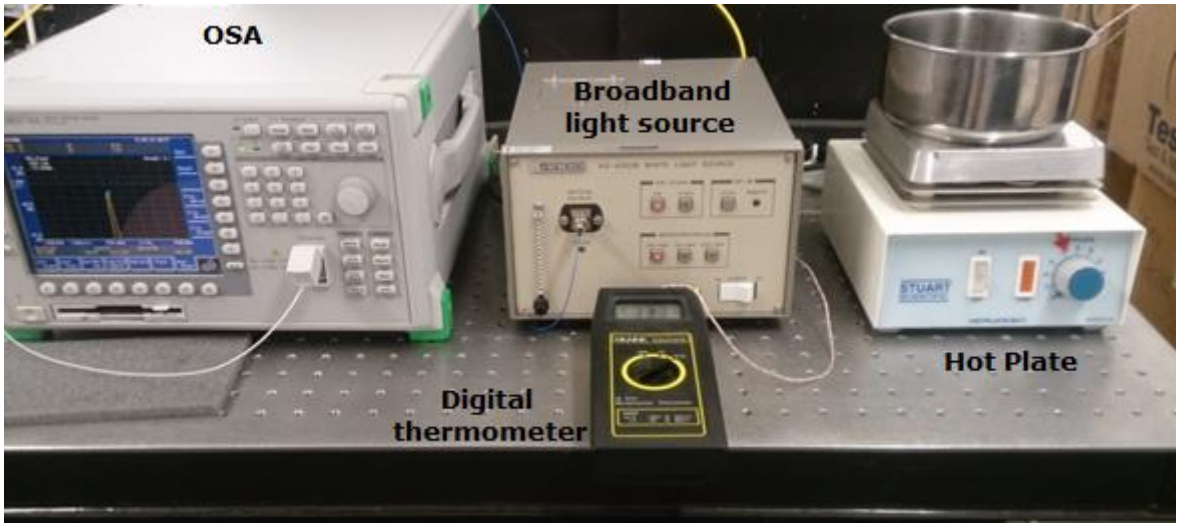

Figure 4.12: Experimental set up for FBG temperature analysis

Figure 4.12 shows the picture of the actual experimental setup used to carry out the FBG temperature analysis. Ando AQ-4303B and Anritsu OSA - MS9710C was used as the light source and detector respectively. The temperature of the water in the vessel was precisely monitored using a digital thermometer and the Stuart Scientific hot plate used is capable of imparting controlled temperature values (0 – 100 °C) in steps of 10 °C.

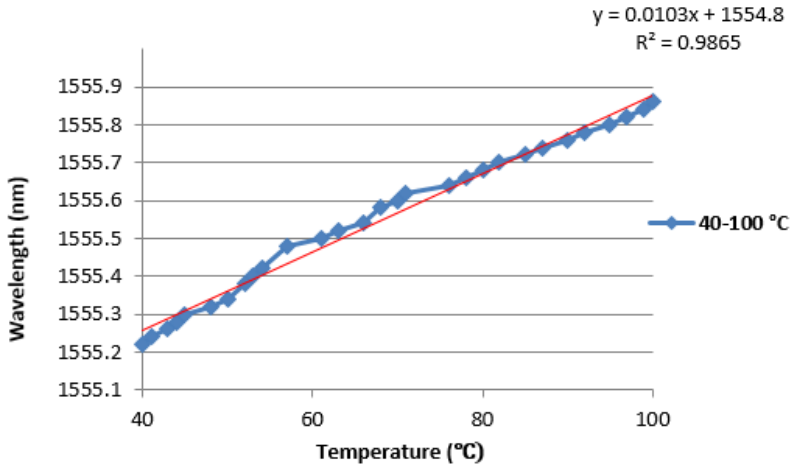

Figure 4.13: Wavelength vs Temperature with FBG sensor in water medium

From Figure 4.13 it is evident that, FBG reflected signal shifts in the longer wavelength direction with increase in temperature. The FBG sensor showed a linear trend for increasing temperatures. FBG temperature sensitivity depends on the thermal expansion coefficient of the fibre and also the thermo-optic effect, which is defined as the temperature induced variation in glass refractive [23-24].

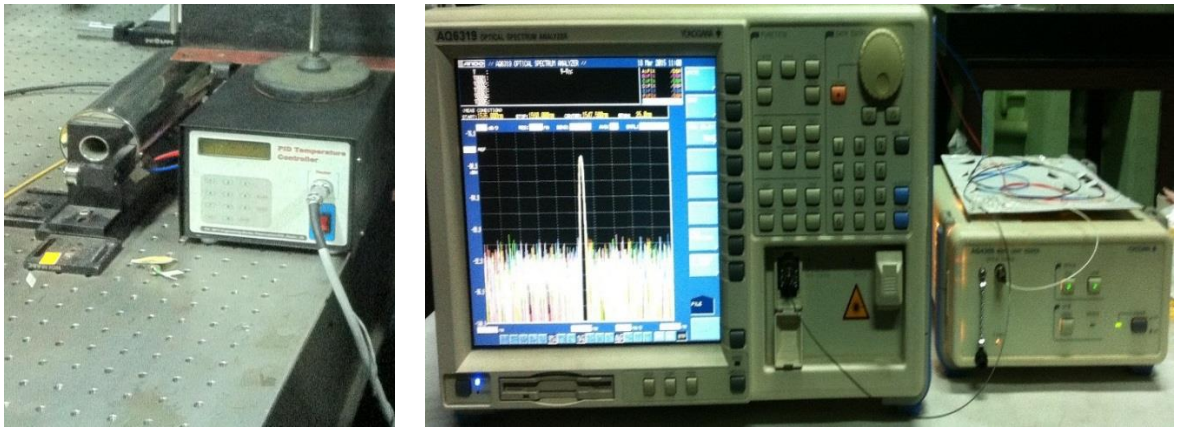

Figure 4.14: Experimental set up used for FBG temperature analysis for temperatures above 100 °C

Figure 4.14 shows the experimental setup used to characterise the FBG temperature sensor for temperatures above 100 °C. To obtain the temperature sensitivities, the FBG sensor was positioned inside the temperature controllable oven, and the temperature was varied in the PID (proportional-integral-derivative) digital temperature controller from about 30 °C to 170 °C. In Figure 4.14, the spectrum that can be seen on the OSA screen shows the level of background noise that appears along the FBG signal. This signifies the need for SNR improvement in FBG sensors for long distance remote sensing applications.

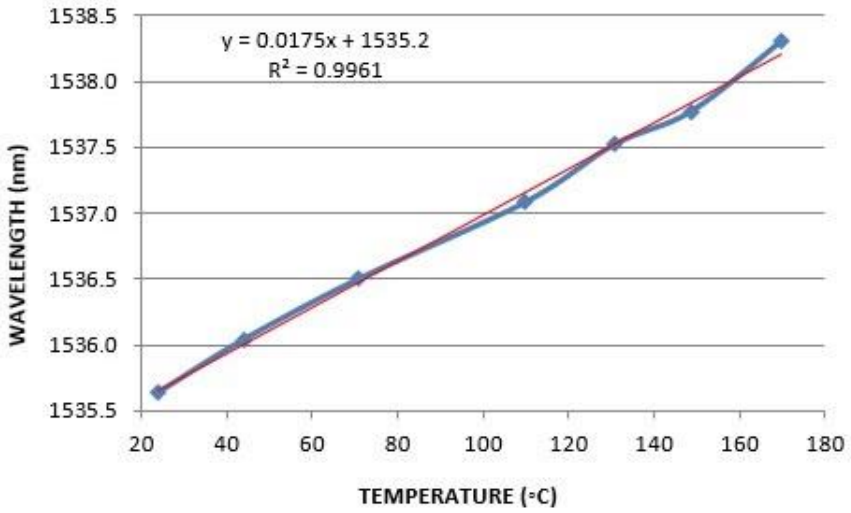

Figure 4.15: Wavelength vs Temperature with FBG sensor in air medium

From Figure 4.15, it can be observed that the FBG reflected wavelength increases steadily for temperatures above 100 °C as well. Despite changes in medium and increase in temperature, the FBG temperature sensor maintains its trend in wavelength shift.

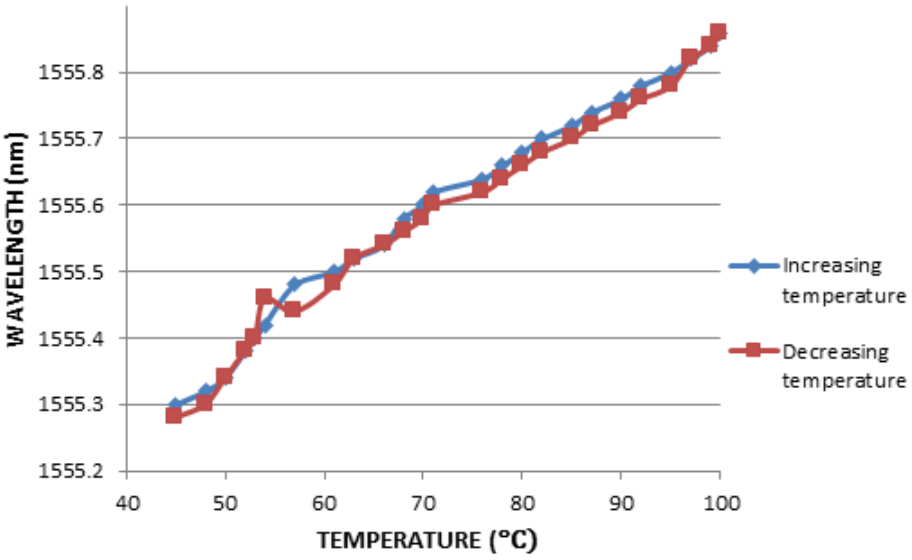

Figure 4.16: FBG temperature Reversibility

Figure 4.16 depicts the reversibility feature of the FBG temperature sensor. From the graph, it can be observed that the FBG sensor follows similar paths for increasing and decreasing temperature values.

4.5.2 FBG Tensile and Compressive Strain Analysis

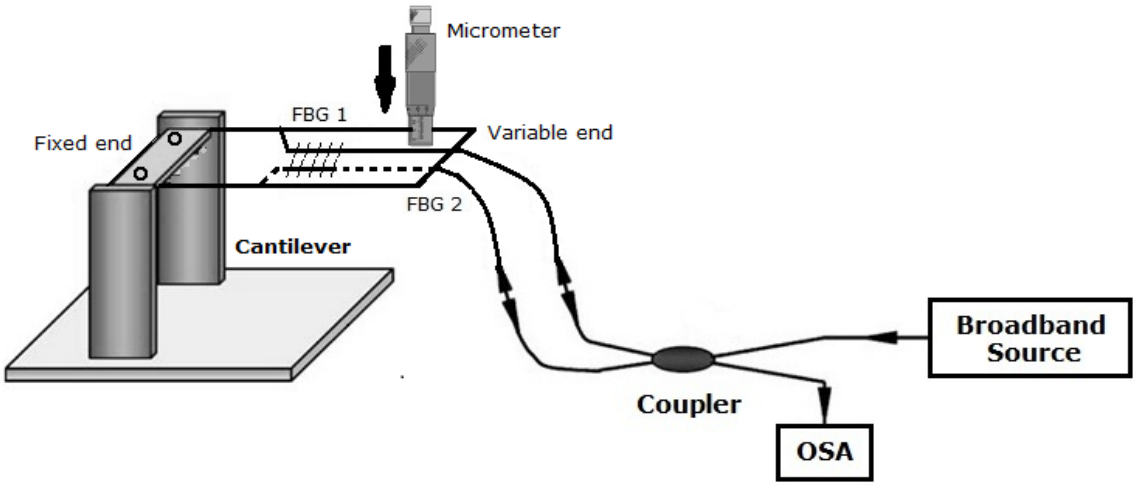

Figure 4.17 Pictorial view of FBG strain analysis experimental setup

Cantilever based strain analysis were carried out to understand the response of the FBG sensor to tension and compression. The objective behind this study was to validate its suitability for O&G condition monitoring applications.

Figure 4.17 shows the pictorial view of the cantilever setup used to carry out the micro-displacement based compressive and tensile strain analysis. In order to analyse both types of strains a dual FBG sensor configuration [25] was used. Two FBGs with reflectivity wavelength 1555 nm and 1540 nm were glued on to the cantilever metal plate with, one above and one below the cantilever respectively. The cantilever plate was made of Aluminium material with dimensions of 30 cm x 3 cm x 0.3 cm. One end of the cantilever was fixed and to the other end strain was applied by a micrometer which is fixed on to a translational stage. The micrometer was varied in steps of 0.05 mm in order to take the readings.

In the FBG strain sensor system shown in Figure 4.17, output from the broad band source is coupled into the 2 x 2 fibre coupler, where the power is equally distributed in both the arms of the waveguides. From each of the output ports of the coupler, the light beam goes into the FBGs and the reflected signals from

the sensor gratings are analysed in the OSA. By examining the reflected spectrum, the shift in wavelength and its grating parameters can be monitored.

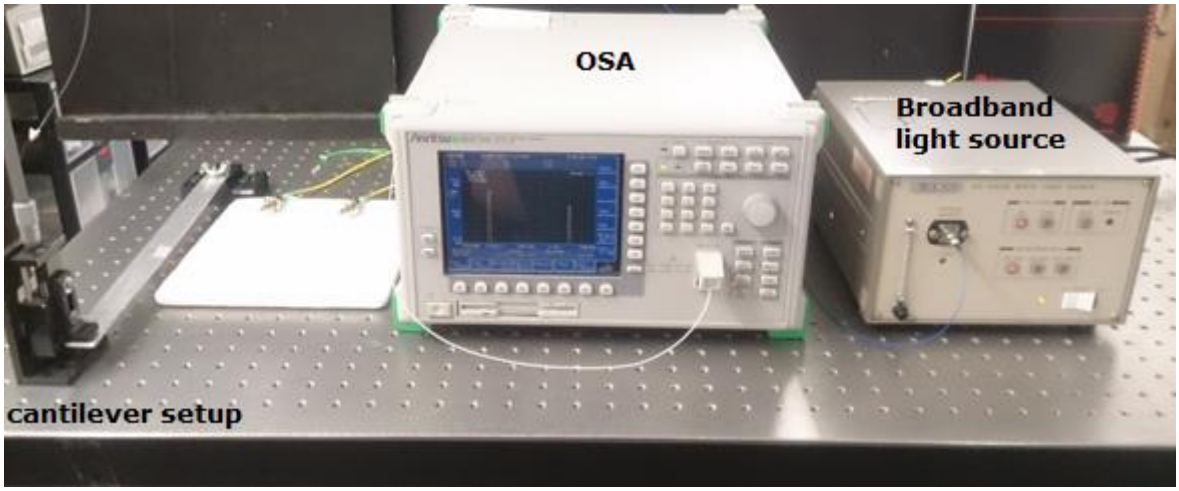

Figure 4.18: Experimental set up for FBG strain analysis

Figure 4.18 shows the picture of the cantilever setup used to carry out the micro-displacement based compressive and tensile strain analysis. White light source from Ando (AQ-4303B) was coupled to the FBGs using a 50:50 coupler and the reflected signal from FBGs were detected and analysed in the Anritsu (MS9710C) OSA.

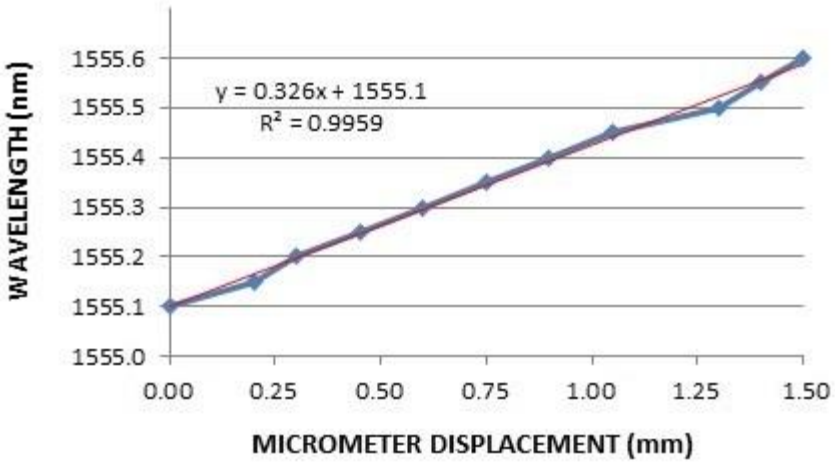

Figure 4.19: Wavelength vs Displacement on application of tensile strain

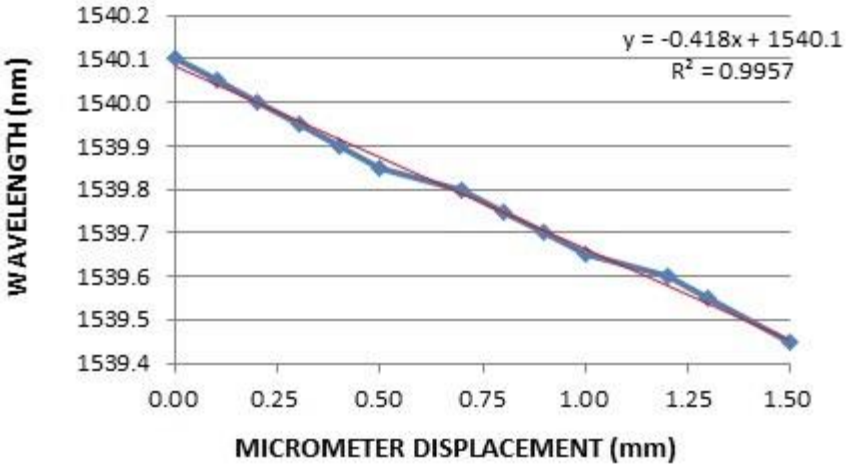

Figure 4.20: Wavelength vs displacement on application of compressive strain

From the graph shown in Figures 4.19 and 4.20, it can be observed that the reflected wavelength from FBG linearly increases with tensile strain and linearly decreases with compressive strain. The reflectivity curve of the FBGs experiences a upward and downward wavelength shift on application of the micrometer displacement for tensile and compressive strain respectively. The strain measurements were taken under constant temperature conditions (room temperature $= 20℃$), in order to avoid errors due to temperature coupling in strain measurements. The strain sensitivity of FBG occurs mainly due to the compression and expansion of its grating period and also the strain-optic effect; which is defined as the strain-induced change in glass refractive index [23-24].

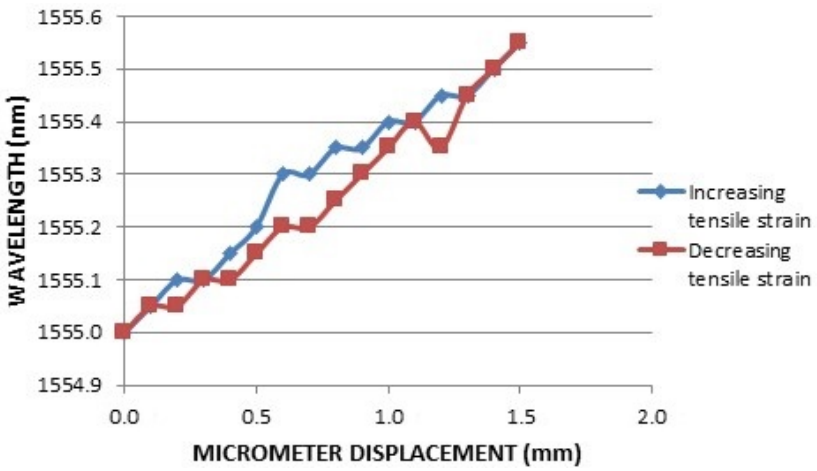

Figure 4.21: FBG Strain Reversibility

The graph in Figure 4.21 depicts the reversibility feature of the FBG sensor on application of strain. Reversibility of a sensor measures its capability to follow the changes of the input parameter regardless of which direction the change is made. From the graph, it can be observed that the FBG sensor follows almost similar paths for increasing and decreasing strain values. Analysis of repeatability of the sensor gives an idea of its stability against constantly varying and challenging environmental conditions. Further analysis was carried out by varying the positions of strain application on the cantilever plate.

4.5.3 Investigations of positional influence of FBG sensors

This section investigates the effect of FBG sensor positions on its reflected signal, in order to optimise the sensor positioning plan for structural health monitoring of O&G structures. Theoretical (refer appendix) and experimental studies was carried, to evaluate FBG strain sensitivities with varying positions. Cantilever beam structure was used to study the effect of strain under different applied load conditions [26-28]. The position of load applied to the cantilever beam was varied to evaluate the strain at various positions along the beam to optimise the placement of sensors on such structures.

Strain was applied at 3 different positions, each at a distance of 7.5 cm from each other. Figure 4.22 illustrates the different positions on the cantilever were strain was applied using the micrometer.

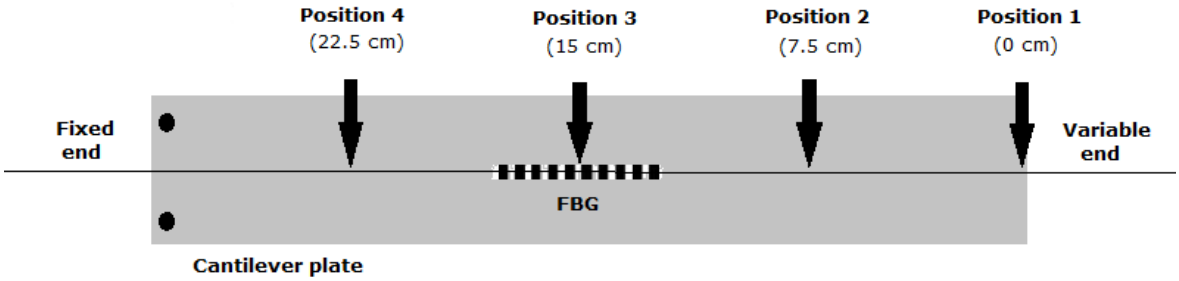

Figure 4.22: Illustration of cantilever positions

A micro-displacement-based strain analysis was carried out using a rectangular cantilever beam, in order to analyse the positional influence of FBG on the sensing signal. A cantilever setup was used for the experimental investigation of strain because it resembles most of the elongated offshore structures like flare booms, cranes, etc. Experiments were carried out using cantilever beam of Aluminium material with dimensions of 300 mm x 30 mm x 3 mm. One end of the cantilever was fixed and strain was applied at different positions of the cantilever by a micrometer. The micrometer was varied in steps of 0.05 mm in order to take the readings. FBG sensor was attached on to the cantilever beam to analyse the impact of varying positions of strain application on the reflected signal from FBG. Optical instruments like OSAs, broad band light sources and coupler were used in the experiment to obtain the shift in Bragg wavelength for any strain transferred on to the FBG sensor from the cantilever beam.

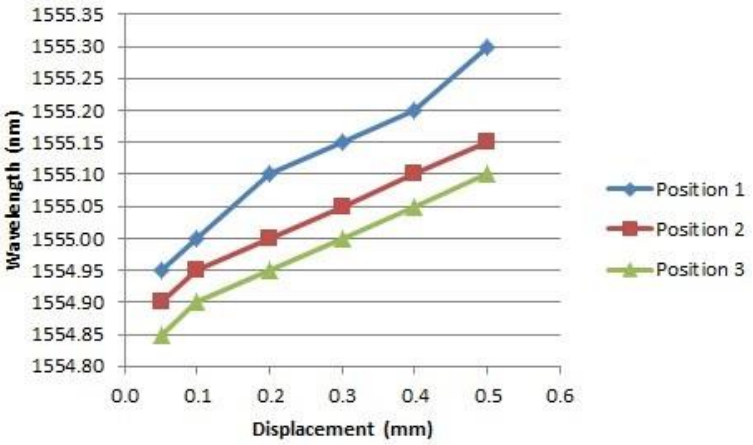

Figure 4.23: FBG strain responses at different cantilever positions

From the graph shown in Figure 4.23, it is clear that FBG reflected wavelength decreases with increasing distance from the cantilever free end, maintaining the linear trend. The reflected wavelength experienced a shift with changing positions of strain application. From the graph, it is also clear that FBG's strain sensitivity is dependent on the position of strain application.

For validating the FBG results, experiments were carried out using strain gauges. Three strain gauges were fixed on the stainless-steel cantilever (25 mm x 1 mm x 300 mm) at 275 mm (strain gauge 1), 250 mm (strain gauge 2) and 225 mm (strain gauge 3) position from the fixed end. Strain measurements were performed by varying the displacement of the cantilever. As the displacement increased, higher strain values were observed along the cantilever at all the positions as shown in Figure 4.24. A higher strain was observed towards the fixed end of the cantilever for each displacement.

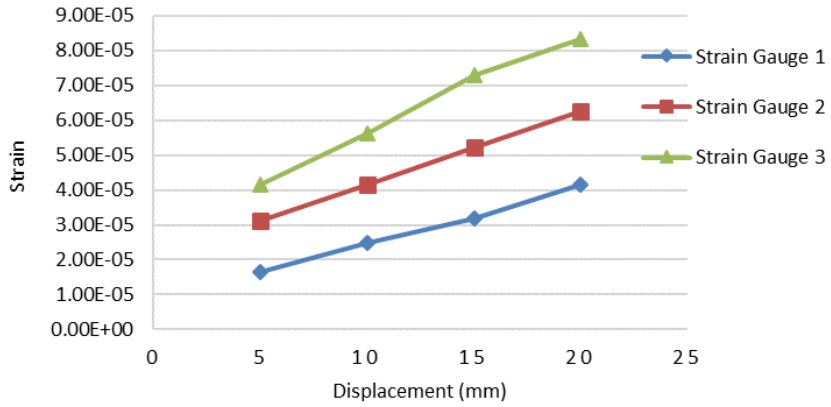

Figure 4.24: Strain measured along the rectangular cantilever beam for the different displacements

Hence, by properly positioning the FBG sensor, a stronger reflected signal can be obtained, which in turn improves the SNR of the sensor. This positional influence of FBG sensors can be utilised in the structural health and condition monitoring of different offshore and subsea structures.

4.5.4 FBG based acoustic sensing

In recent years, an increasing number of offshore platforms are being operated unmanned, considering the cost implications of the asset operations and maintenance. Being unmanned, the conventional inspection and monitoring techniques are no longer effective and there arises a need for new monitoring

strategies. Consequently, remote monitoring of offshore platforms and critical subsea structures like christmas tree, subsea manifolds, etc., are gaining considerable attention, as it can provide valuable information to predict potential damages occurring on these structures due to the highly corrosive and harsh environment. In addition, collision between offshore platforms and vessels is another serious problem confronted by the oil companies which is structurally more destructive than the environmental impact. Therefore, a continuous, real-time and remote condition monitoring system is vital to provide a reliable means of structural inspection at a minimal cost.

Optical fibre technology offers immense potential and capabilities for real time and remote monitoring of O&G structures. FBG sensors have not been extensively studied for structural health monitoring of submerged or dynamic offshore structures. The current research work focusses on how FBG sensors can be used to detect micro-cracks from within the offshore and subsea structures.

During the initial stage of any fatigue crack creation from within the structure, acoustic signals are emitted. Detecting these crack initiations using FBG sensors based on acoustic emission signal allows the early detection and prediction of the time to failure of the structure under monitoring. This is a very useful, non-destructive and smart sensing technique for continuous monitoring of offshore structures to identify the structural integrity issues, identify its impact and mitigate failures.

The features of a smart condition monitoring system include: ability to monitor structures remotely on a real-time basis, no battery power requirements, ability to return stronger sensing signals (High SNR), ability to operate in a harsh

marine environment, high reliability (continuously monitor with high accuracy and precision) and higher sensor lifetime.

This section studies the effect of crack induced acoustic emissions on FBG reflected signal, for structural health monitoring of subsea structures. Acoustic emissions were initiated via a Pencil Lead Break (PLB) test carried out on the fixed rectangular metal plate attached with the FBG sensor. PLB source also termed as Hsu-Nielsen (HSN) source is a widely used, reproducible artificial acoustic source for test signals in acoustic emission applications [29-30]. In PLB test a pencil lead (usually 2H, 0.3 mm) is broken against the test structure which is the rectangular metal plate in this experiment under a defined angle. [31]. A special shoe aids in breaking the lead consistently. The frequency spectrum of a PLB source ranges from 40 kHz to 600 kHz [32]. A reference FBG was kept close to the metal plate, to account for any ambient condition changes.

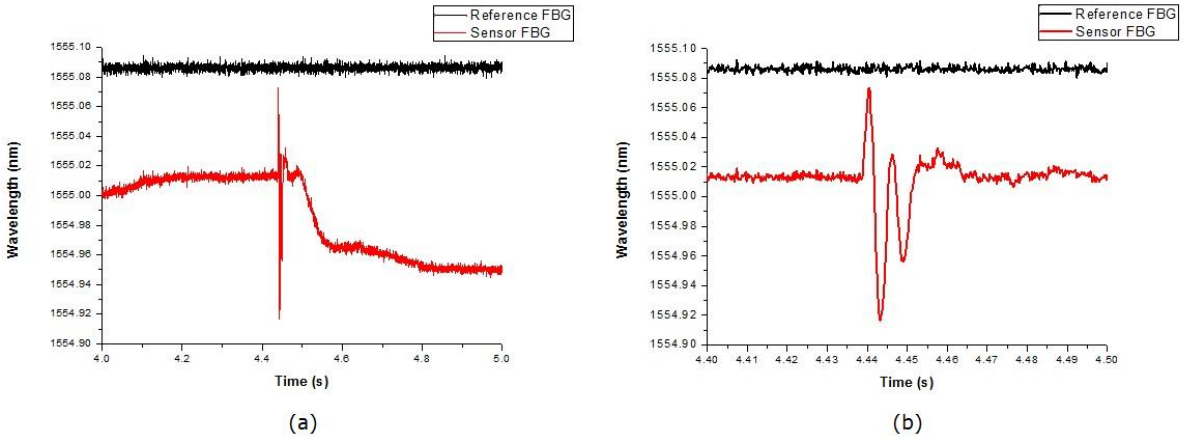

Figure 4.25: FBG sensor responses to pencil lead break experiment

Figure 4.25 shows that the FBG sensor responses to the pencil lead break experiment. Through the experiment it was proved that the FBG is sensitive to detect acoustic emissions initiated from the lead crack. The PLB initiates acoustic emissions which in turn generates elastic waves on the metal plate. These elastic waves interacts with the electromagnetic or optical waves propagating

through the optical fibre via the FBG sensor. The longitudinal acoustic wave generated from the pencil lead break creates a strain on the FBG sensor, which in turn affect its Bragg reflected wavelength. This strain induced on the FBG consists of a tensile strain component and a compressive strain component. FBG's reflected wavelength linearly increases with tensile strain and linearly decreases with compressive strain [33].

To sum up, the investigations carried out proved that, the FBG sensors can be effectively used for the early identification of cracks, prediction and prevention of failure scenarios of the huge offshore and subsea structures.

4.6 Summary

The investigations carried out in this chapter looked at different ways of using FBG in O&G applications. The detailed study carried out helped in understanding the operation of FBG sensors, the issues associated with O&G sensing environment and also the different ways of achieving signal enhancement. The investigations carried out identified the relevance of proper positioning of FBG sensors for condition monitoring of offshore structures, as a properly positioned FBG experiences an enhancement in its sensitivity. The experimental study conducted using the cantilever set-up helped in identifying the changing response of FBG with different types of strain application (compressive and tensile strain) and also with varying strain positions. MATLAB simulations conducted on FBG sensor revealed the possibility of optimising its grating parameters to achieve higher accuracy, improved sensing range and increased number of sensors down-hole by tuning its reflectivity and spectral width. To sum up, identifying the right position of FBG sensors with respect to pipeline axis and other subsea infrastructures and optimisation of its various grating

parameter enhances its capabilities for structural health monitoring, as FBG sensors records highest amplitude and peak sensitivity at specific points. Optimised positioning of FBG sensors aids in precise and accurate measurement of physical parameters and also improves the sensor range within ultra-deep oil well. Hence, PCF-FBG sensor configuration with optimised capabilities of FBG along with the remarkable features of microstructured fibres make them a better solution compared to existing down-hole electrical sensors. However, even though PCF-FBG sensors are capable of sensing various physical parameters, it has got few downsides like cross-sensitivity and difficulty in sensing multiple parameters simultaneously. Hence, additional spectroscopic techniques are investigated in Chapters 5 and 6 to realise multimodal sensors without any cross-sensitivities.

4.7 References

[1] Martelli C, Canning J, Groothoff N and Lyytikainen K. Bragg gratings in photonic crystal fibers: strain and temperature chacterization. *17th International Conference on Optical Fibre Sensors*: International Society for Optics and Photonics. 2005; 302-306.

[2] Jollivet C, Guer J, Hofmann P, Schulzgen A. Monolithic fiber lasers combining active PCF with Bragg gratings in conventional single-mode fibers. *IEEE Journal of Selected Topics in Quantum Electronics.* 2014; 20(5):36-41.

[3] Zhao Y, Zhang Y, Wu D, Wang Q. Magnetic field and temperature measurements with a magnetic fluid-filled photonic crystal fiber Bragg grating. *Instrumentation Science & Technology.* 2013; 41(5):463-472.

[4] Inaudi D, Glisic B. Long-range pipeline monitoring by distributed fiber optic sensing. *Journal of Pressure Vessel Technology.* 2010; 132(1):011701.

[5] Habel WR, Schukar V and Hofmann D. Requirements to establish fibre-optic sensors for monitoring of structures. *EWSHM-7th European Workshop on Structural Health Monitoring*; 2014.

[6] Othonos A. Bragg gratings in optical fibers: fundamentals and applications. *Optical Fiber Sensor Technology.* Springer. 2000; 79-187.

[7] Hill KO, Meltz G. Fiber Bragg grating technology fundamentals and overview. *Journal of Lightwave Technology.* 1997; 15(8):1263-1276.

[8] Aulakh NS, Kaler R. *Investigations on fiber bragg gratings for fiber optic communication systems.* Doctoral dissertation, Thapar University; 2010.

[9] Sipe J, Poladian L, De Sterke CM. Propagation through nonuniform grating structures. *Journal of the Optical Society of America A.* 1994; 11(4):1307-1320.

[10] Kashyap R. *Fiber bragg gratings.* Academic Press; 2009.

[11] Erdogan T. Fiber grating spectra. *Journal of Lightwave Technology.* 1997; 15(8):1277-1294.

[12] Ivorra B, Mohammadi B, Redont P, Dumas L, Durand O. Semi-deterministic versus genetic algorithms for global optimisation of multichannel optical filters. *International Journal of Computational Science and Engineering.* 2006; 2(3-4):170-178.

[13] Yariv A. Coupled-mode theory for guided-wave optics. *IEEE Journal of Quantum Electronics.* 1973; 9(9):919-933.

[14] Kogelnik H. Theory of optical waveguides. *Guided-wave optoelectronics*: Springer. 1988; 7-88.

[15] Poladian L. Graphical and WKB analysis of nonuniform Bragg gratings. *Physical Review E.* 1993; 48(6):4758.

[16] Karim F, Seddiki O. Numerical analysis of raised cosine sampled chirped Bragg grating for dispersion compensation in dense wavelength division multiplexing systems. *International Journal of Communication.* 2009; 3:9-16.

[17] Rao Y. In-fibre Bragg grating sensors. *Measurement Science and Technology.* 1997; 8(4):355.

[18] Othonos A. Fiber bragg gratings. *Review of Scientific Instruments.* 1997; 68(12):4309-4341.

[19] Benameur S, Kandouci M, Aupetit-Berthelemot C, Joti A. Dense Wavelength Division (De) Multiplexers Based on Fiber Bragg Gratings. *Sensors & Transducers.* 2014; 27(5):62.

[20] Ennser K, Zervas N, Laming R. Optimization of apodized linearly chirped fiber gratings for optical communications. *IEEE Journal of Quantum Electronics.* 1998; 34(5):770-778.

[21] Sun N, Liau J, Kiang Y, Lin S, Ro R, Chiang J, et al. Numerical analysis of apodized fiber Bragg gratings using coupled mode theory. *Progress in Electromagnetics Research.* 2009; 99:289-306.

[22] Werneck MM, Allil RC, Ribeiro BA, de Nazaré FV. A guide to fiber Bragg grating sensors. *Current Trends in Short-and Long-period Fiber Gratings.* InTech; 2013.

[23] Mihailov SJ. Fiber Bragg grating sensors for harsh environments. *Sensors.* 2012; 12(2):1898-1918.

[24] Kersey AD, Davis MA, Patrick HJ, LeBlanc M, Koo K, Askins C, et al. Fiber grating sensors. *Journal of Lightwave Technology.* 1997; 15(8):1442-1463.

[25] Zhao Y, Yu C, Liao Y. Differential FBG sensor for temperature-compensated high-pressure (or displacement) measurement. *Optics & Laser Technology.* 2004; 36(1):39-42.

[26] Bansal R. *A textbook of strength of materials.* Laxmi Publications; 2010.

[27] Zhang Y, Ren Q, Zhao Y. Modelling analysis of surface stress on a rectangular cantilever beam. *Journal of Physics D: Applied Physics.* 2004; 37(15):2140.

[28] Johny J, Summers J, Bhavsar K, Joseph GP, Fung WK and Prabhu R. Theoretical investigation of positional influence of FBG sensors for structural health monitoring of offshore structures. *OCEANS 2017-Aberdeen: IEEE*. 2017; 1-5.

[29] Van Dam J and Bond LJ. Acoustic emission monitoring of wind turbine blades. *Smart Materials and Nondestructive Evaluation for Energy Systems 2015*: International Society for Optics and Photonics. 2015; 94390C:1-15.

[30] Sause MG. Investigation of pencil-lead breaks as acoustic emission sources. *Journal of Acoustic Emission.* 2011; 29.

[31] Vallen H. AE testing fundamentals, equipment, applications. *Journal of Nondestructive Testing.* 2002; 7(9):1-30.

[32] Falcetelli F, Romero MB, Pant S, Troiani E, Martinez M. Modelling of Pencil-Lead Break Acoustic Emission Sources using the Time Reversal Technique. *Proceedings of the 9th European Workshop on Structural Health Monitoring, Manchester.* 2018; 10-13.

[33] Johny J, Prabhu R, Fung WK and Watson J. Investigation of positioning of FBG sensors for smart monitoring of oil and gas subsea structures. *OCEANS 2016-Shanghai: IEEE.* 2016; 1-4.

5. PHOTOLUMINESCENCE SPECTROSCOPIC INVESTIGATIONS ON RARE EARTH DOPED GLASSES

5.1 Introduction

Rare earth material is a widely researched and unique class of optical material, owing to their wide range of potential applications in the field of different photonic devices including lasers, amplifiers, light sources and optical sensors. Even though many research studies have been carried out on rare earth doped materials and rare earth doped sensors for many years, there are not many studies reported that utilise their capabilities for fibre optic based O&G sensing applications.

The choice of different absorption-emission bands provided by various rare earth elements and the ease of doping these elements into appropriate host matrices makes them a suitable candidate for fibre optic sensing applications [1-2]. Important advantages of rare earth doped fibre optic sensors include wide range of wavelength tunability, covering the visible and near infrared spectral ranges, compatibility with existing optical fibres and its materials and higher pulse peak power [3]. Furthermore, the applications of rare earth doped sensors include temperature sensing, chemical sensing, biological sensing, etc., [4-5].

This chapter concentrates on the spectroscopic characterisation of rare earth doped glass materials with the aim of enhancing the signal and realizing PCF-rare earth-FBG based multi-parameter sensor configuration.

Absorption and photoluminescence spectroscopic studies have been carried out on the fabricated rare earth doped glasses in order to analyse the effect of different rare earth concentrations and excitation wavelengths on the photoluminescence signal intensity. Material composition and surface quality of

the glass samples have been investigated using energy dispersive X-ray analysis (EDXA) and scanning electron microscopy (SEM) respectively.

5.2 Theoretical Background

Photoluminescence is the light emission caused when a material is irradiated with light (normally ultraviolet or visible light). Among different light matter interaction phenomenon's like absorption, reflection, etc., photoluminescence is a very important class; as it is a source of new wavelength of light [6]. Normally, photoluminescence or fluorescence emissions occur at a longer wavelength after a small interval of time (termed as fluorescence lifetime), as a result of the absorption of shorter wavelength (also called as excitation wavelength) [7]. Typically, fluorescence emission occurs within a nanosecond to millisecond time span after light irradiation.

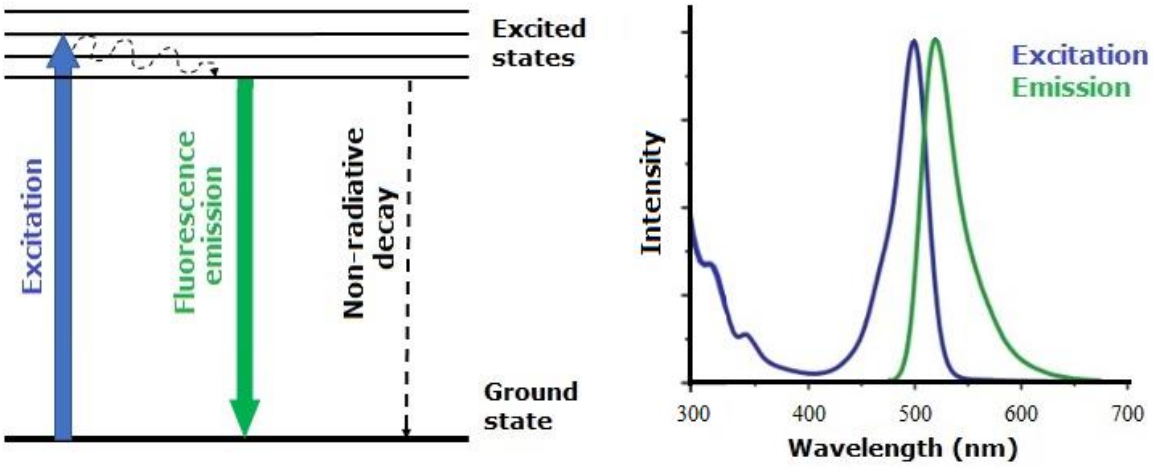

Figure 5.1: (a) Illustration of energy state transitions (b) excitation and photoluminescence emission profile

Photoluminescence involves the excitation of electrons from a lower vibrational energy state to a higher energy state with the irradiation of light, from where radiative decay is possible. The optimal or most efficient excitation wavelength usually corresponds to the absorption maximum [8]. During the excitation

process, photon absorption happens instantaneously and very soon the photoluminescence molecule relaxes to the lowest vibrational energy level within the excited state. Following this, next transition occurs, and the molecule goes back to its ground state either through spontaneous emission or non-radiative decay process. In spontaneous emission, energy is released in the form of photon; whereas in non-radiative decay process, energy is released in the form of heat. The emitted photon has lower energy than excitation photon, as some energy was lost during the relaxation process. This results in a shift in the photoluminescence wavelength with respect to the excitation wavelength and is known as the Stokes shift [9]. Usually photoluminescence profile experiences a red shift relative to the excitation profile, wherein spectral shifting occurs towards the higher wavelength (i.e. lower energy and lower frequency) [10].

The rare earth dopant ions belong to the transition metal or lanthanide series and are characterised by unfilled $4f$ shells in the interior of the ion. The rare earth elements possess sharp and well-defined photoluminescence spectral features, dominated by sharp zero-phonon lines [11]. This is because the outer shell $(5S^2 \; and \; 5P^6)$ electrons of the rare earth ions screen the inner unfilled $4f$ shell from outside perturbing influences, which protects the optically active electrons from the influence of the crystal field to some extent [11-12]. However, many phenomena like multi-phonon relaxation, (phonon assisted) energy transfer, cooperative luminescence and cross relaxation are possible mainly due to interaction of the 4f electrons and their surroundings [13]. The electron—phonon coupling strength for rare earth ions can be analysed from its temperature dependent line broadening. At elevated temperatures the line width of the zero-phonon lines increases due to phonon induced relaxation

processes [14]. Generally, for temperature sensors based on lanthanides doped materials, low phonon energy materials are preferred, because in hosts with low cut-off phonon energies, the emission intensity of rare-earth ions introduced as doping is enhanced by several times [15].

Rare earth ions doped within the optical glass invokes photoluminescence and can be detected using a suitable photodetector or spectrometer. Important advantages of rare earth materials over other photoluminescence materials include: unique excitation-emission patterns, narrow photoluminescence emission profiles, laser Stokes shift providing wavelength differentiation and wave guidance properties.

5.3 Fabrication of rare earth doped glasses

Different rare earth doped glasses were fabricated using the melt-quench and sol-gel glass production techniques for carrying out various spectroscopic investigations [16-17]. Spectroscopic studies of rare earth doped glasses were carried out to understand the effect of rare earth doping concentration and excitation wavelengths on photoluminescence signal intensity. Furthermore, photoluminescence spectroscopy-based temperature studies of the rare earth doped glasses were carried out to verify its suitability for high temperature sensing as needed for the O&G industry.

From the different glass host systems available such as borate glass, soda lime glass, borosilicate glass, phosphate glass, etc., borosilicate glass was chosen as the base glass for rare earth doping [18]. Zinc borosilicate glass (ZBSG) host system was chosen as it is a well-established candidate material for phosphorescence applications [19]. The glass matrix with ZnO enhances its glass forming ability and ensures low rates of crystallization [20]. Furthermore,

ZnO addition enhances the emission cross-section and the intensity of emission of the doped glass which could be due to better solubility of rare earth ion in the glass host system [21].

For the first batch of glass samples, 3 rare earth doping elements – terbium (Tb), erbium (Er) and ytterbium (Yb) were selected. Er and Yb elements were chosen mainly because Er doped fibres and Yb doped fibres are commercially available which would aid in multimodal sensor development and Tb was picked because through literature review it was identified that they possess temperature sensitivity [22]. Photoluminescence glass materials of different concentrations were fabricated by carefully doping these rare earth elements into the borosilicate glass host matrix. The starting materials used for the preparation of different concentrations of rare earth doped borosilicate glasses were zinc oxide (ZnO), boron oxide (B_2O_3), silicon dioxide (SiO_2), terbium III chloride hexahydrate $(TbCl_3.6H_2O)$. All chemicals were purchased from Sigma Aldrich with greater than 99% purity [23].

The batch mixture of zinc borosilicate glass was:

$$60ZnO + 20B_2O_3 + 20SiO_2\ (mol\%)$$

The weighed chemical batches consist of 4.5717 g ZnO, 1.3034 g B_2O_3 and 1.1253 g SiO_2, giving a total weight of 7 g.

The rare earth doped borosilicate glass batch mixture was:

$$(60 - x)ZnO + 20B_2O_3 + 20SiO_2 + xLa^{3+}$$ (where La^{3+}= Tb, Er, Yb)

where x value relates to the decrease in ZnO composition and the corresponding rare earth concentration increase from 0.5, 1.0, 1.5, and 2.0 mol% [24].

Figure 5.2: Image of (a) sample weighing, (b) milling machine, (c) agate ball mill and (d) powdered sample mixture

As can be observed in Figure 5.2 (a) and (b), the weighed batches each of 7 g were ground on an agate ball mill for 7 minutes using the Glen Creston milling machine. Figure 5.2 (c) shows the picture of the agate vial or jar used. After the ball milling process the homogenous powder mixture (Figure 5.2 (d)) was transferred into a platinum crucible and was introduced into the Carbolite 1400 high temperature furnace (Figures 5.3 (a) and (b)) at a starting set temperature of 550 °C. After 30 minutes the temperature was increased to 900 °C and maintained for an hour. Following this the temperature was increased to 1000, 1100 and 1200 °C, for one hour at each stage. Finally, at 1200 °C the fully melted powdered chemicals forming the glass melt was poured onto a brass mould to obtain the glass samples of uniform thickness. The brass mould was heated to an annealing temperature of 100 °C on a hot plate (Figure 5.3 (c)) to reduce chances of glass cracking due to thermal stresses. Figure 5.3 (d) shows the obtained glass sample within the mould.

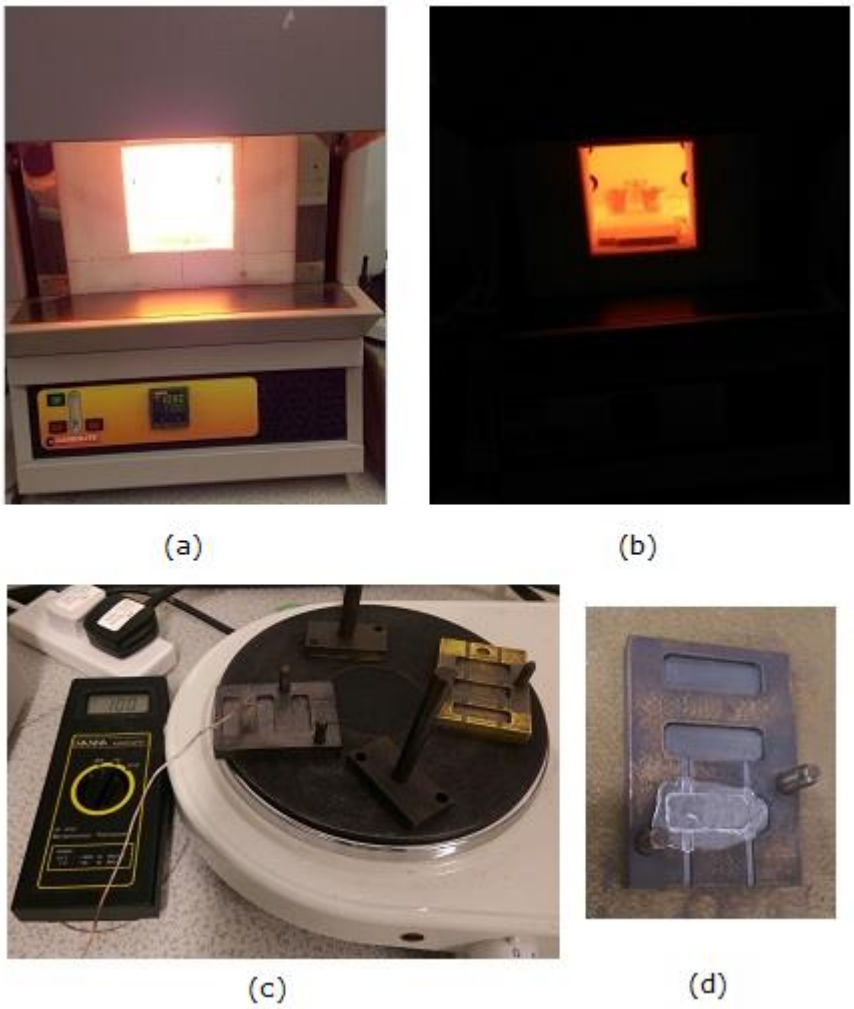

Figure 5.3: Image of: (a) hot furnace, (b) Platinum crucibles containing powdered chemicals kept inside hot furnace, (c) heated brass mould and (d) glass sample formed in the mould

Subsequently, the rare earth doped glass preform was pulled into micron diameter sized fibres for developing rare earth doped fibres.

5.4 SEM and EDAX analysis of rare earth doped glasses

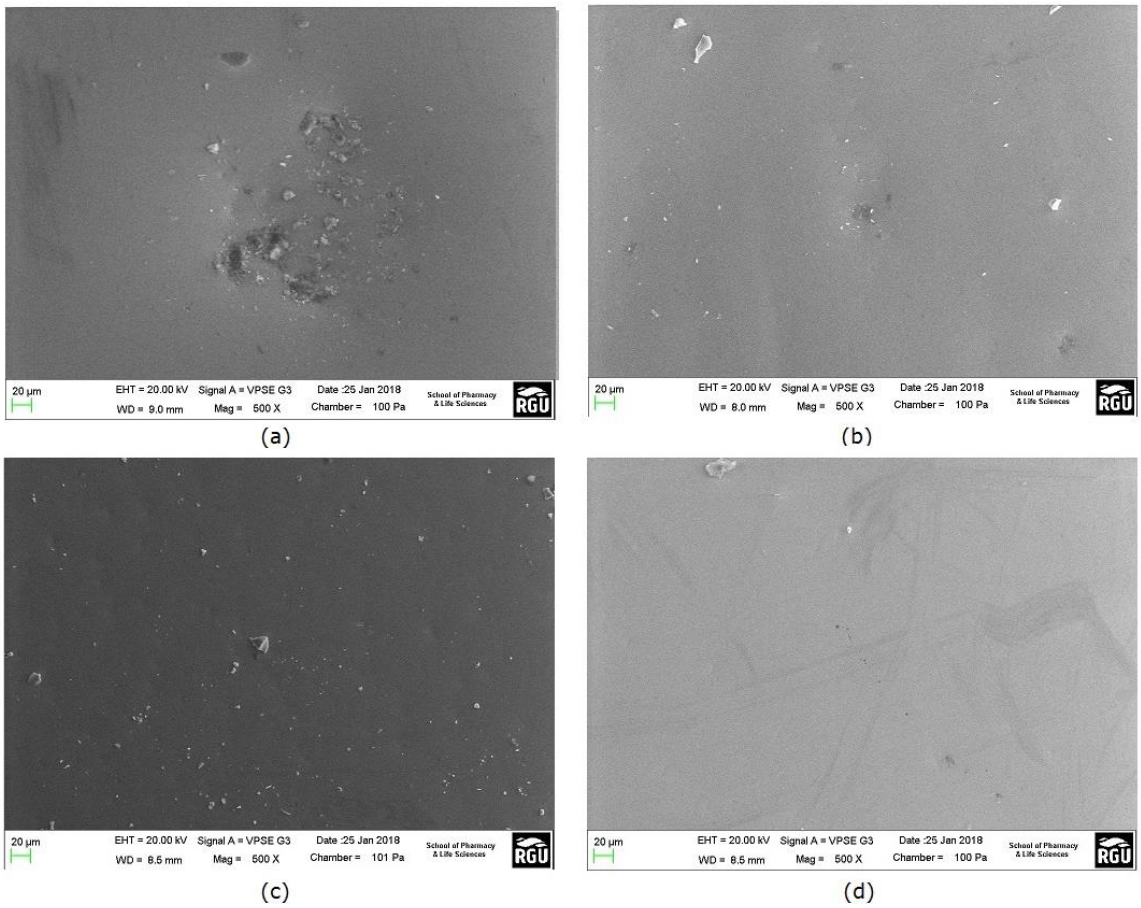

Figure 5.4: SEM image of: (a) ZBSG, (b) 2 mol% Tb doped ZBSG, (c) 2 mol% Er doped ZBSG, (d) 2 mol% Yb doped ZBSG at 500X magnification

The surface quality of the fabricated rare earth doped glass samples has been analysed by imaging it under the Carl Zeiss EVO LS10 SEM. Figure 5.4 and 5.5 shows the SEM images of blank ZBSG, Tb doped ZBSG, Er doped ZBSG and Yb doped ZBSG with rare earth concentration 2 mol%, at different scales $(20\ \mu m, 1\ \mu m)$ and magnifications (500X, 10.00 KX). From the SEM images shown in the figures, it can be observed that the surface of the glass samples are without any cracks. Some small particles seen on the surface might be pieces of broken glass chips and glass powders stuck on to the glass surface. It is important to understand the smoothness of the glass surface, as these doped glass preforms will be used for fibre drawing, and therefore it is important to avoid any chances of breakages of the fibre during the fibre drawing process.

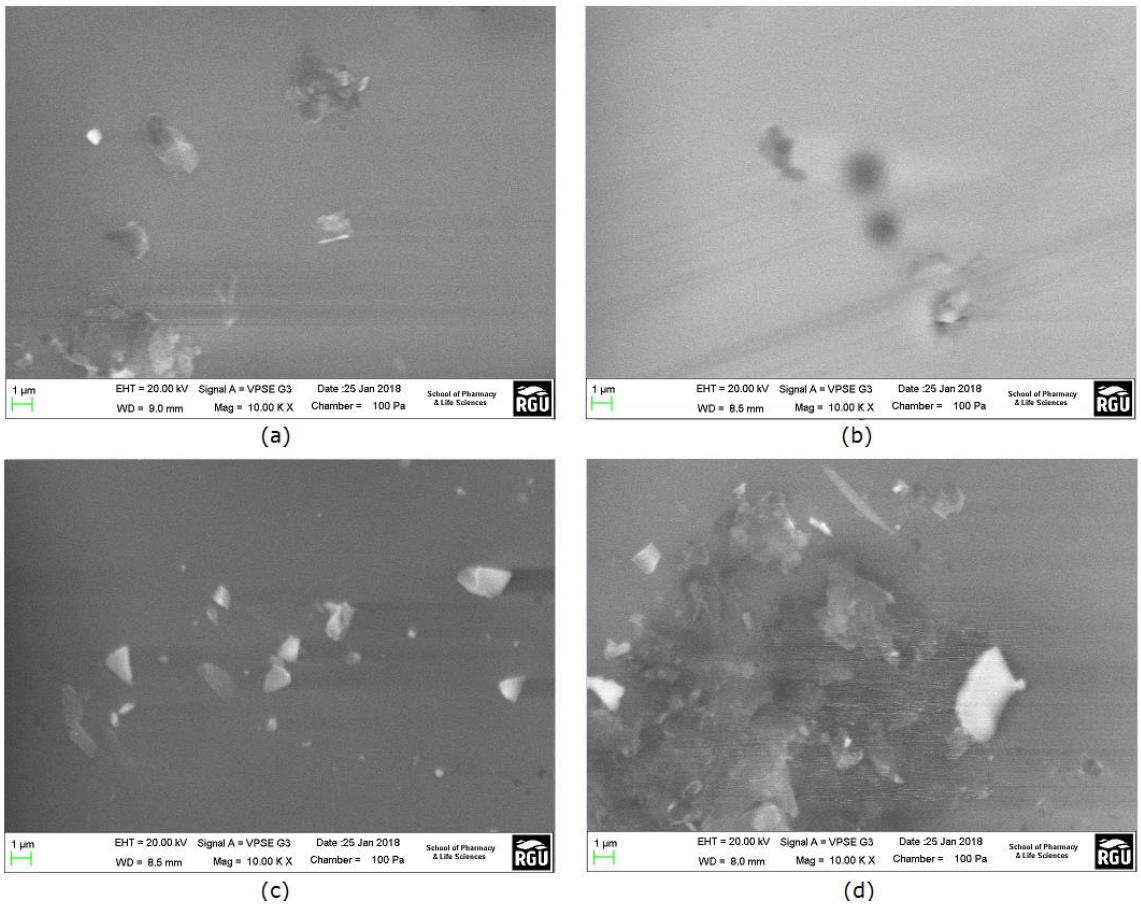

Figure 5.5: SEM image of: (a) ZBSG, (b) 2 mol% Tb doped ZBSG, (c) 2 mol% Er doped ZBSG, (d) 2 mol% Yb doped ZBSG at 10.00KX magnification

Further analysis was carried out using the Oxford Instruments INCA EDXA coupled with the Carl Zeiss EVO LS10, to verify the material composition of the different glass samples. The EDXA graphs confirmed the presence of the corresponding rare earth dopant ions and other constituent atoms of the blank ZBSG, Tb doped ZBSG, Er doped ZBSG and Yb doped ZBSG samples respectively. In the EDXA graph shown in Figure 5.6 (a), the elements present in the fabricated ZBSG was verified. It was observed that in addition to the B (boron), O (oxygen), Zn (zinc) and Si (silica) elements coming from the base or starting materials (ZnO, B_2O_3 and SiO_2) some traces of C (carbon) were also obtained. Similar elements were also found on the EDXA graphs of the rare earth doped glasses with rare earth elements Tb, Er and Yb as shown in Figures 5.6 (b), (c) and (d). Figures 5.6 (b), (c) and (d) also confirms the presence of

the corresponding rare earth elements within the fabricated glass samples. Basically, EDXA was carried out to understand if the rare earth is well doped into the glass matrix.

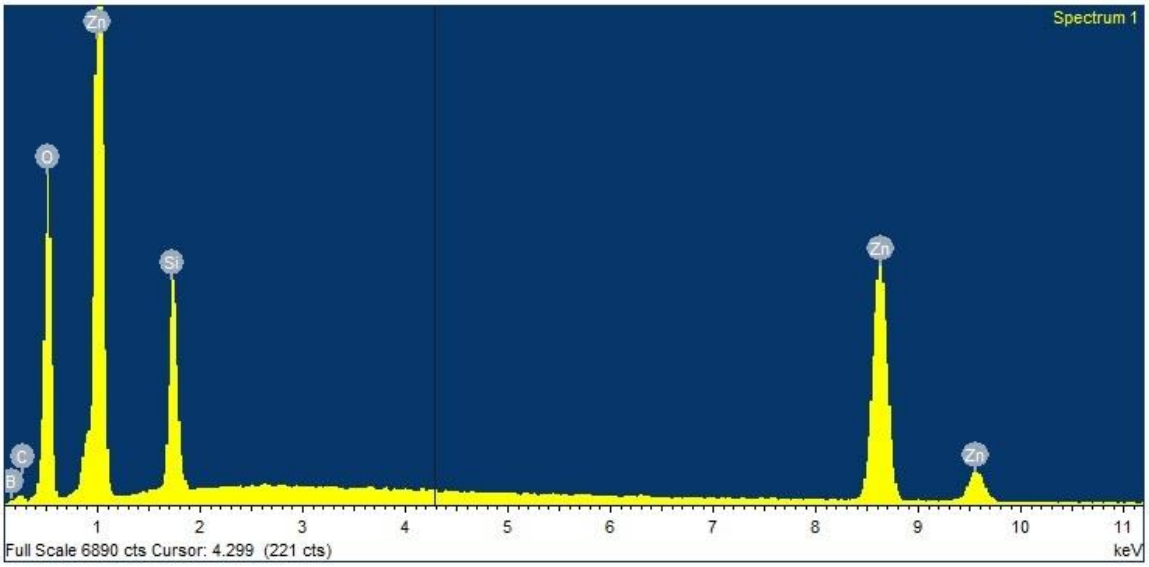

(a)

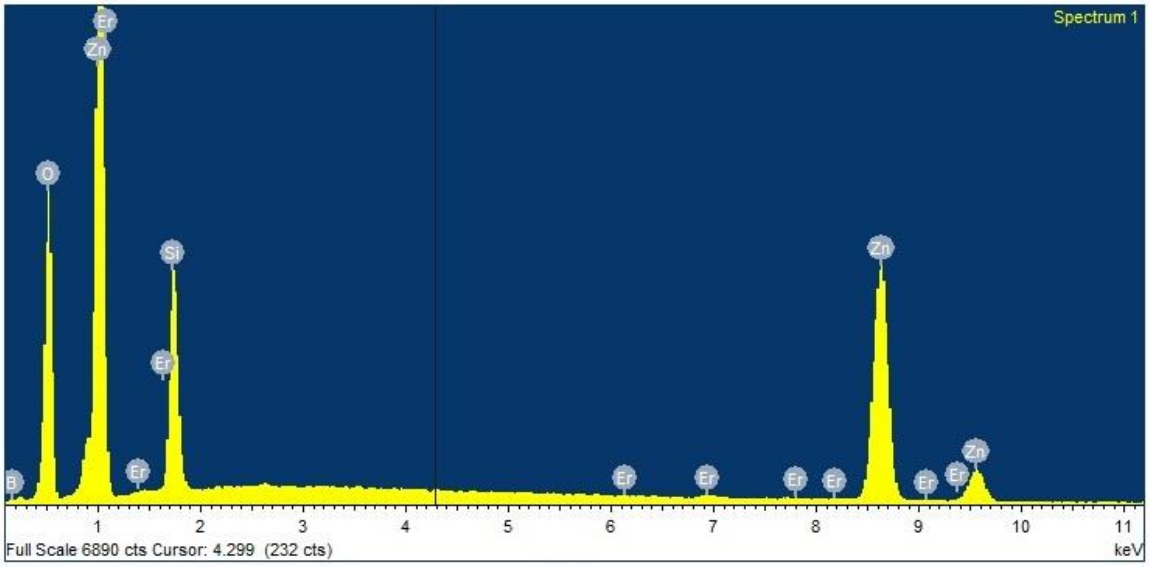

(b)

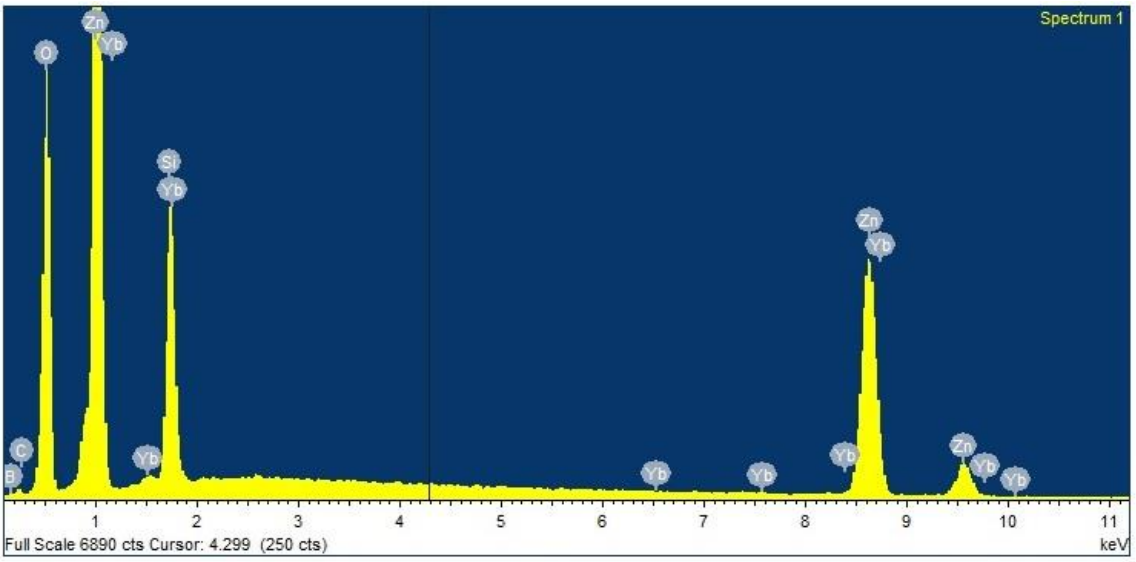

(c)

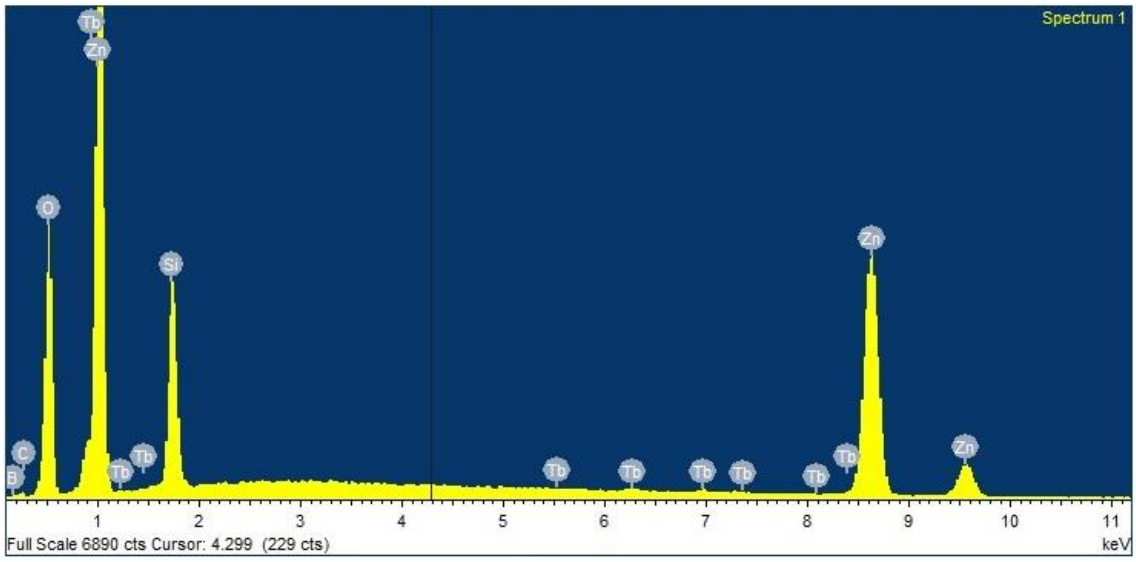

(d)

Figure 5.6: EDAX spectrum of: (a) ZBSG, (b) 2 mol% Er doped ZBSG, (c) 2 mol% Yb doped ZBSG and (d) 2 mol% Tb doped ZBSG

5.5 UV-VIS-NIR Absorption studies of rare earth doped glasses

The principle of absorption spectroscopy is - when light beam travels through a medium like glass, its intensity gets reduced. This is because absorption happens, when the energy of light photon matches with the energy needed to excite an electron within the glass to its higher energy state, and hence the photon is absorbed by the glass. Absorbance value normally depends on the

glass composition, thickness and the wavelength of incident light. Absorbance is given by the (Beer-Lambert law) [25-26].

(a) (b)

Figure 5.7: Picture of (a) absorption spectrometer and (b) glass sample fixed on the cuvette introduced into the sample compartment

Absorption studies were carried out using the Perkin Elmer Lambda 950 Spectrophotometer (Figure 5.7 (a)). Each of the glass sample (~ 2 mm size) was fixed vertically in a small cuvette in order to hold the sample perpendicular to the incident beam. Following this, the glass sample fixed on the cuvette was inserted vertically into the cuvette holder compartment (Figure 5.7 (b)) for absorption analysis. The samples were scanned for the full wavelength range 190 nm – 2300 nm, covering the ultra-violet (UV, < 400 nm) visible (VIS, 400-800 nm) and near infrared (NIR, > 800 nm) wavelengths. Absorption studies were carried out after performing background corrections and the spectra obtained corresponding to each glass composition is explained in the following paragraphs.

Though the Beer-Lambert law accommodates both concentration and optical path length dependencies, absorption analysis is not a great approach for making concentration comparisons. This is because the proportion of the light absorbed will depend on how many molecules it interacts with. Hence,

concentration dependencies of the rare earth doped glass samples are not analysed using the obtained absorption results.

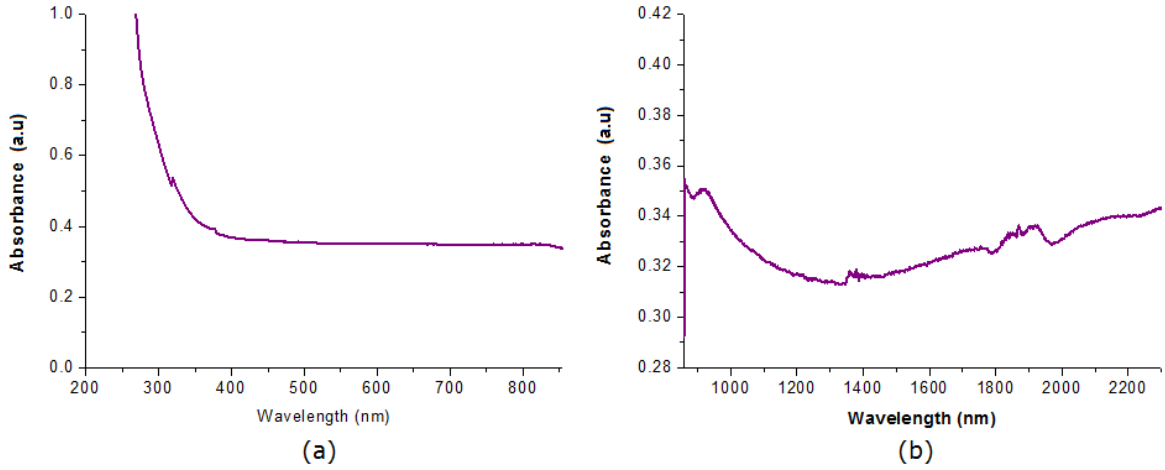

Figure 5.8: Absorption spectrum of blank ZBSG: (a) UV-VIS range, (b) NIR range

Figure 5.8 shows the absorption spectrum for blank ZBSG in the UV-VIS and NIR wavelength range. Figure 5.8 (a) shows the high UV absorption characteristics of the borosilicate glass and the transparency of glass in the visible wavelengths. The origin of absorption peaks around 1400 nm and 1800 nm is attributed to the presence of OH group [16]. The absorbance value of blank ZBSG sample was obtained around 0.35. Slight deviations in the absorbance values in other glass samples is probably due to unpolished glass sample. Hence, the choice of BSG as the host for rare earth ions was appropriate as the characteristic photoluminescence signatures of the rare earth dopants will not be affected by any interference effects. The energy level diagram for Tb, Er and Yb is shown in figure 5.9.

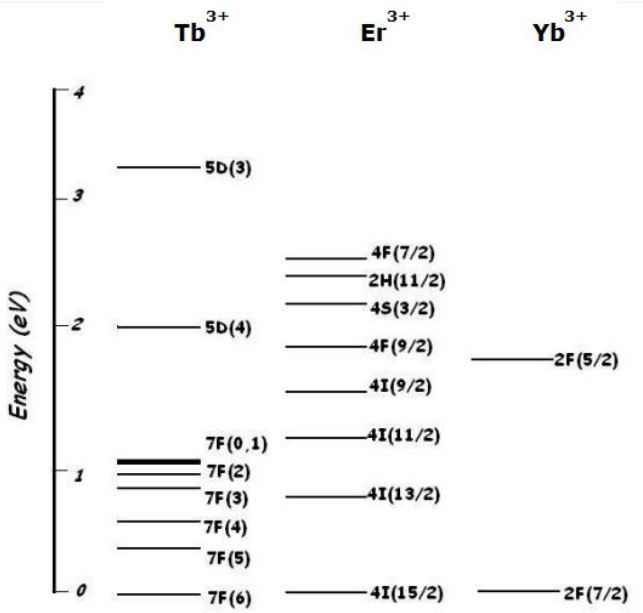

Figure 5.9: Energy level diagrams corresponding to Tb^{3+}, Er^{3+} and Yb^{3+} [27]

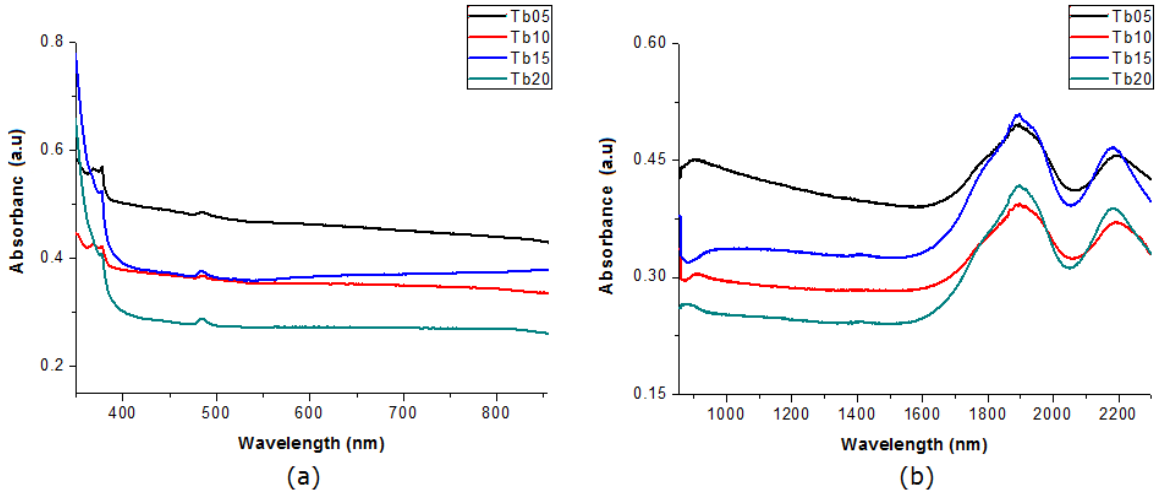

Figure 5.10: Absorption spectrum of different concentrations of Tb doped ZBSG: (a) UV-VIS range and (b) NIR range

Figure 5.10 shows the absorption spectrum for Tb doped ZBSG samples in the UV-VIS and NIR wavelength range. In the graphs Tb05, Tb10, Tb15 and Tb20 represent the glass codes for the 0.5, 1.0, 1.5 and 2.0 mol% Tb doped ZBSG. From Figure 5.10 (a) a high UV absorption can be observed owing to the BSG host matrix and the characteristic absorption peaks of Tb dopants can be seen at 376 nm $(^5D_3 \rightarrow {}^7F_6)$ and 486 nm $(^5D_4 \rightarrow {}^7F_6)$[28-31]. The spectral peaks observed in the NIR (1800-2300 nm) range are the glass peaks from the BSG host.

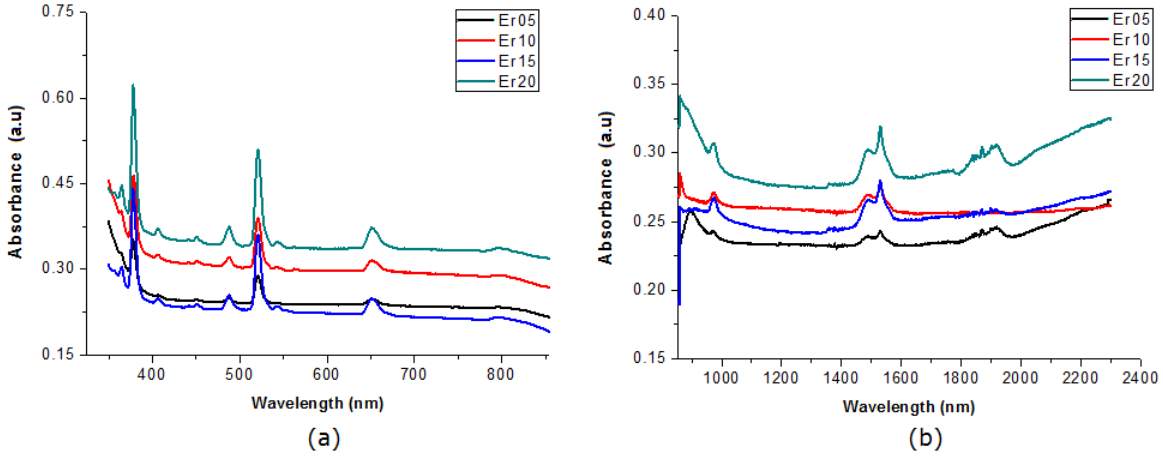

Figure 5.11: Absorption spectrum of different concentrations of Er doped ZBSG: (a) UV-VIS range, (b) NIR range

Figure 5.11 shows the absorption spectrum for Er doped ZBSG samples in the UV-VIS and NIR wavelength range. In the graphs Er05, Er10, Er15 and Er20 represent the glass codes for the 0.5, 1.0, 1.5 and 2.0 mol% Er doped ZBSG. It can be observed that, the characteristic absorption bands of the Er dopants centred around 365 nm (Energy level transition: ${}^4I_{15/2} \rightarrow {}^4G_{9/2}$), 378 nm (${}^4I_{15/2} \rightarrow {}^4G_{11/2}$), 406 nm (${}^4I_{15/2} \rightarrow {}^2H_{9/2}$), 451 nm (${}^4I_{15/2} \rightarrow {}^4F_{3/2,5/2}$), 488 nm (${}^4I_{15/2} \rightarrow {}^4F_{7/2}$), 520 nm (${}^4I_{15/2} \rightarrow {}^2H_{11/2}$), 543 nm (${}^4I_{15/2} \rightarrow {}^4S_{3/2}$), 651 nm (${}^4I_{15/2} \rightarrow {}^4F_{9/2}$), 797 nm(${}^4I_{15/2} \rightarrow {}^4I_{9/2}$), 971 nm (${}^4I_{15/2} \rightarrow {}^4I_{11/2}$), 1530 nm (${}^4I_{15/2} \rightarrow {}^4I_{13/2}$) [32-34]. Other small peaks observed in the wavelength range 1800-2300 nm are the glass peaks of the host matrix as explained earlier.

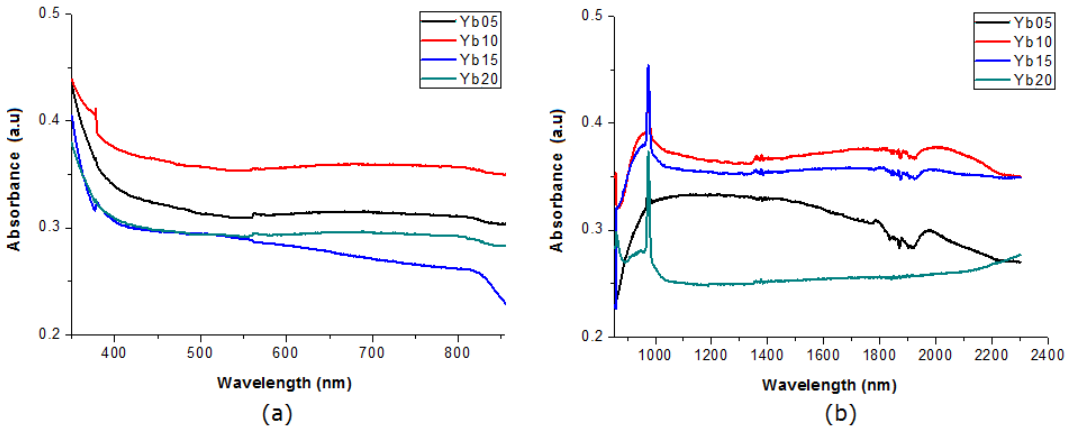

Figure 5.12: Absorption spectrum of different concentrations of Yb doped ZBSG: (a) UV-VIS range, (b) NIR range

From figure 5.12 (a), it can be observed that there are no evident absorption peaks for Yb doped ZBSG in the UV-VIS spectral regions and the high UV absorption arises from the BSG host system. Yb05, Yb10, Yb15 and Yb20 represent the glass codes for the 0.5, 1, 1.5 and 2 mol% Yb doped ZBSG. The sharp absorption peak of Yb doped ZBSG centred around 975 nm (Figure 5.12 (b)) corresponds to the $^2F_{7/2} \rightarrow {}^2F_{5/2}$ energy level transition of the Yb^{3+} ion [35-37]. The broad absorption of Yb is due to electronic transitions involving the Stark sublevels of the $^2F_{7/2}$ and $^2F_{5/2}$ levels [36].

5.6 Photoluminescence spectroscopic studies of rare earth doped glasses

photoluminescence properties of the fabricated rare earth doped glasses were characterised using the Edinburgh Instruments fluorescent spectrometer (F900) shown in Figure 5.13 (a). Figure 5.13 (b) shows the sample fixed on the glass holder introduced on to the sample compartment of the photoluminescence spectrometer. Xenon light source (Xe900) and the Hamamatsu blue PMT were used as the source and detector respectively.

Figure 5.13: Picture of (a) Edinburgh instrument photoluminescence spectrometer and (b) glass sample with the sample holder introduced into the sample compartment

Excitation and emission scans were run on the glass samples to obtain their excitation peak wavelengths and their corresponding photoluminescence signatures. The excitation and emission slit widths were set to 5 nm for the excitation-emission scans. The light excitation at lower or higher wavelengths affects the intensity of emitted light or the photoluminescence. Hence, it is important to find the wavelength corresponding to the excitation maximum to obtain the maximum photoluminescence emission intensity.

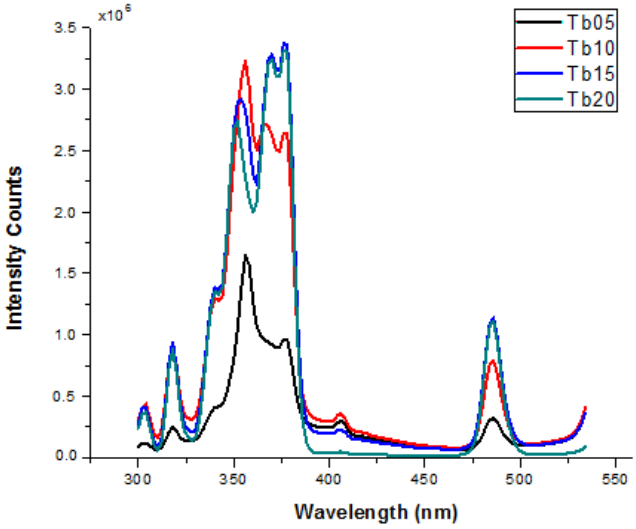

Figure 5.14: Excitation spectra for different Tb concentrations corresponding to 544 nm photoluminescence emission

Figure 5.14 shows the measured excitation spectra of different concentrations of Tb doped BSG recorded in the wavelength range 300 – 525 nm, corresponding to the green photoluminescence emission at 544 nm. In the graphs Tb05, Tb10, Tb15 and Tb20 represent the glass codes for the 0.5, 1.0, 1.5 and 2.0 mol% Tb doped BSG. The excitation spectrum displayed peaks at 304, 318, 354, 376, 406 and 486 nm. However, the bands at 304 and 406 nm were weaker compared to other excitation peaks. The most intense peak at 376 nm corresponds to the transition from the Tb ground state $^7F_6$ to the higher excited level ($^5D_3$, $^5G_6$) [38] suggests the suitability of UV LEDs for irradiating

the Tb doped glass and obtaining its corresponding photoluminescence emission.

Figure 5.15 (a) depicts the optical photoluminescence spectra of the Tb doped glass in response to an optical excitation of 376 nm. This analysis was carried out in order to understand the effect of terbium concentration on its photoluminescence intensity and thereby optimise the Tb doping concentration level within the waveguide. The Tb characteristic photoluminescence peak was obtained at 544 nm corresponding to its green emission $(^5D_4 \rightarrow {}^7F_5)$ [39]. The intensity variation of 544 nm Tb photoluminescence as a function of its concentration, for 376 nm excitation, is shown in Figure 5.15 (b). From the graph, it can be observed that the Tb doped borosilicate glass exhibits a strong luminescence at 1.5 mol% concentration. Further increase of the rare earth concentration to 2 mol% did not improve the photoluminescence signal intensity. Hence, 1.5 mol% is the optimum doping concentration for the earth doped waveguide to obtain maximum signal intensity.

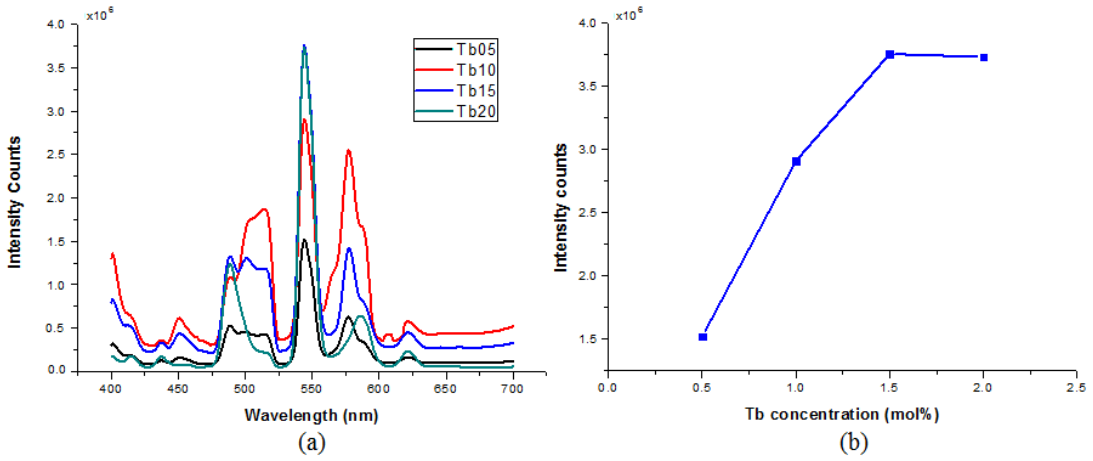

Figure 5.15: (a) Emission spectra for different Tb concentrations corresponding to 376 nm excitation and (b) photoluminescence intensity vs Tb concentration for 544 nm emission under 376 nm excitation

Besides, in order to analyse the effect of different excitation wavelengths on the photoluminescence intensity of the Tb doped BSG, the emission scan was

recorded for different excitation wavelengths as depicted in Figure 5.16 (a). In Figure 5.16 (b), the variation in photoluminescence intensity is plotted as a function of excitation wavelengths for the 544 nm Tb emission. For the different excitation wavelengths tried, highest photoluminescence intensity was obtained for 376 nm excitation followed by 354 nm, 486 nm and 318 nm.

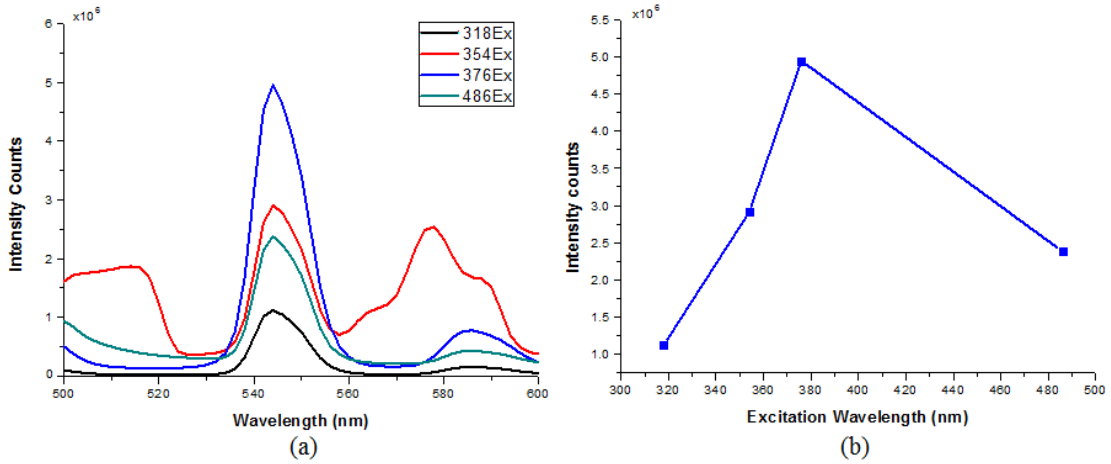

Figure 5.16: (a) Emission spectra of 1.5 mol% Tb for different excitation wavelengths and (b) intensity variation of 1.5 mol% Tb for different excitation wavelengths

After characterising Tb doped glass samples, similar excitation-emission studies were carried out on Er doped samples. Figure 5.17 (a) shows the obtained excitation spectra corresponding to different concentrations of Er doped ZBSG recorded in the wavelength range 300 – 530 nm, corresponding to the 550 nm visible photoluminescence emission. A strong excitation peak was observed at 360 nm, followed by a weaker peak at 392 nm. The most intense peak at 360 nm corresponds to the transition from the Er ground state $^4I_{15/2}$ to the higher excited level ($^4G_{9/2}$) [40].

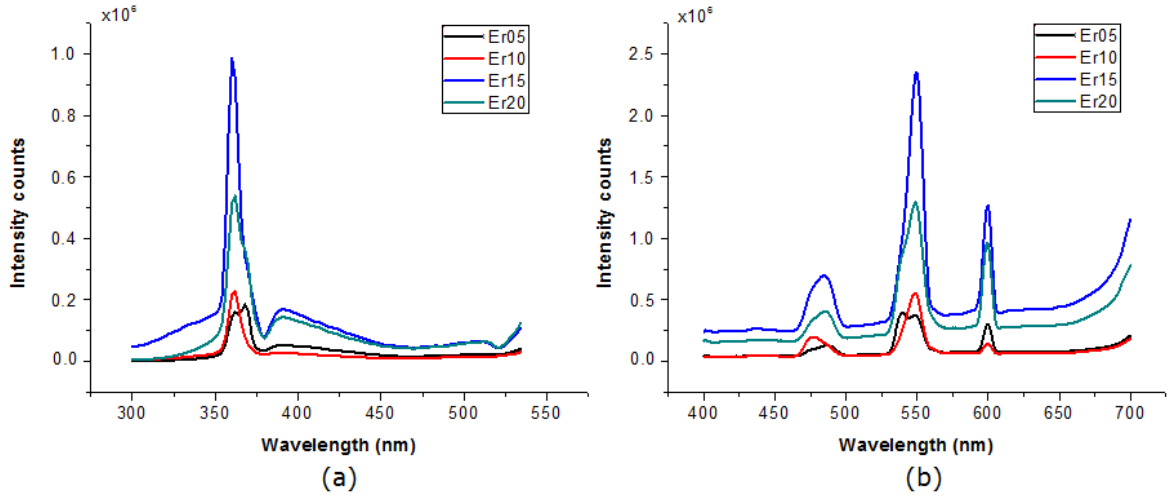

Figure 5.17: (a) Excitation spectra of Er doped glasses corresponding to 550 nm photoluminescence emission and (b) emission spectra of Er doped glasses for 360 nm excitation

Figure 5.17 (b) depicts the optical photoluminescence spectra of the Er doped ZBSG in response to an optical excitation of 360 nm. The characteristic visible photoluminescence peak of Er doped glass was obtained at 550 nm which represents the $^4S_{3/2} \rightarrow {}^4I_{15/2}$ transition [41-42]. From the graph, it is confirmed that the Er doped borosilicate glass exhibits a strong luminescence at 1.5 mol% concentration. Further increase of the rare earth concentration to 2 mol% did not improve the photoluminescence signal intensity. Hence, 1.5 mol% is the optimum doping concentration for the earth doped waveguide to obtain maximum signal intensity.

Another batch of rare earth doped glasses with dysprosium (Dy), cerium (Ce) and holmium (Ho) as doping elements were synthesised for carrying out Raman spectroscopic analysis (Chapter 6). The following section explains the absorption and photoluminescence characteristics of the new batch of glass samples. The energy level diagram for Dy is shown in Figure 5.18.

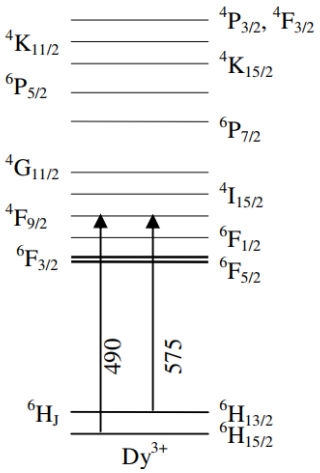

Figure 5.18: Energy level diagram corresponding to Dy^{3+} [43]

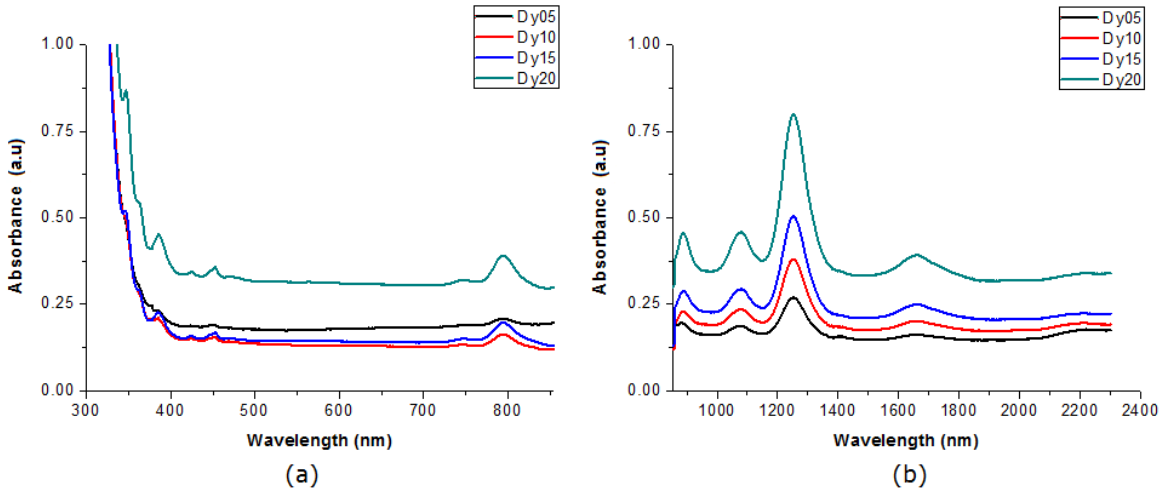

Figure 5.19: Absorption spectrum of different concentrations of Dy doped ZBSG: (a) UV-VIS range, (b) NIR range

Figure 5.19 shows the absorption spectrum of Dy doped ZBSG covering the UV, VIS and NIR wavelengths. Many weak and sharp absorption peaks can be observed within the spectrum. The different Dy signature peaks are located around the wavelengths: 453 nm ($^6H_{15/2} \rightarrow {}^4I_{15/2}$), 473 nm ($^6H_{15/2} \rightarrow {}^4F_{9/2}$), 745 nm ($^6H_{15/2} \rightarrow {}^6F_{3/2}$), 794 nm ($^6H_{15/2} \rightarrow {}^6F_{5/2}$), 888 nm ($^6H_{15/2} \rightarrow {}^6F_{7/2}$), 1078 nm ($^6H_{15/2} \rightarrow {}^6F_{9/2}$), 1252 nm ($^6H_{15/2} \rightarrow {}^6F_{11/2}$) and 1654 nm ($^6H_{15/2} \rightarrow {}^6H_{11/2}$) [43-46]. Figure 5.20 shows the excitation spectra obtained for different concentrations of Dy doped BSG in the spectral range 300 – 500 nm, corresponding to the 575 nm photoluminescence emission. Dy05, Dy10, Dy15 and Dy20 represent the

glass codes for 0.5, 1.0, 1.5 and 2.0 mol% Dy doped BSG. The excitation spectrum shows different peaks at 350, 364, 388, 424, 452 and 470 nm among which the 388 nm peak that corresponds to the transition from the Dy ground state ($^6H_{15/2}$) to the higher energy level ($^4I_{13/2}$, $^4F_{7/2}$) [47], has the highest intensity, hence the same UV LED can be used for illuminating the Dy doped waveguide to obtain its respective photoluminescence emission.

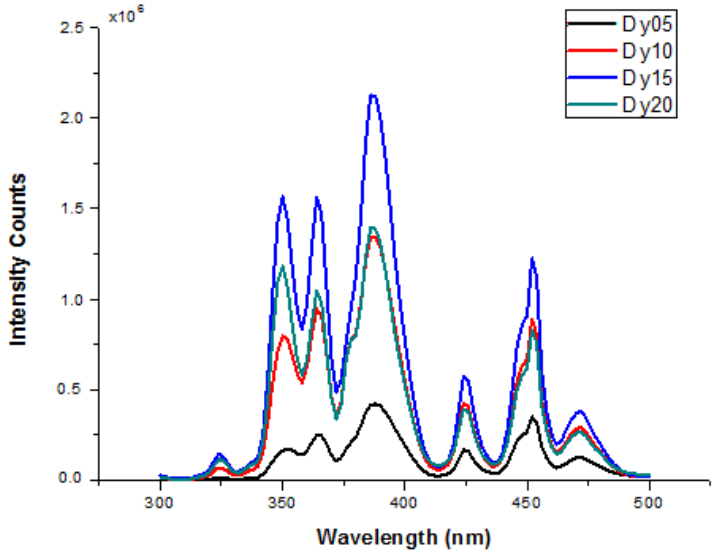

Figure 5.20: Excitation spectra for different Dy concentrations corresponding to 575 nm photoluminescence emission

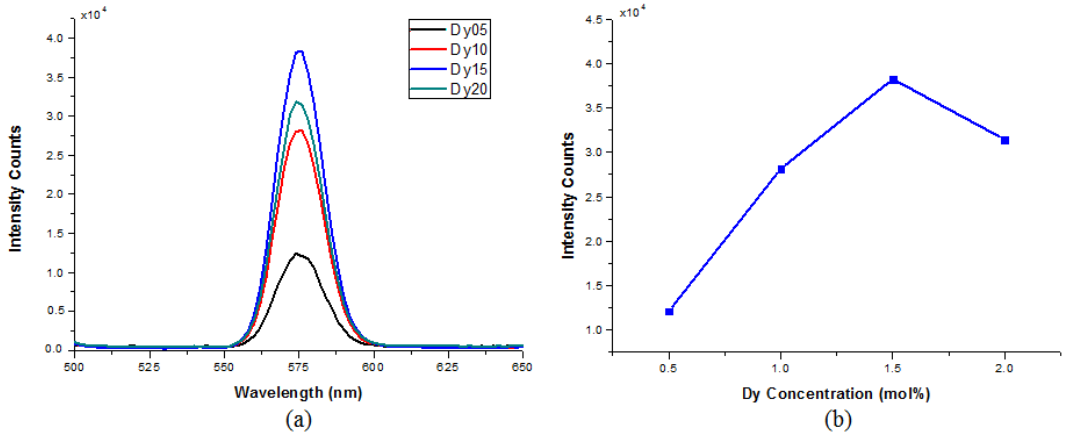

Figure 5.21: (a) Emission spectra for different Dy concentrations corresponding to 388 nm excitation and (b) photoluminescence intensity vs Dy concentration for 575 nm emission under 388 nm excitation

Figure 5.21 (a) shows the photoluminescence emission spectra of Dy doped borosilicate glass for 388 nm excitation. The dysprosium signature peak was

obtained around 575 nm corresponding to its yellowish photoluminescence emission. The intensity variation of 575 nm Dy photoluminescence ($^4F_{9/2} \rightarrow {}^6H_{13/2}$), as a function of its concentration, is shown in Figure 5.21 (b), when the glass sample was excited at 388 nm. From the graph it is very clear that the Dy doped BSG exhibits a strong luminescence at 1.5 mol% concentration and further increase of Dy concentration did not improve the photoluminescence signal. Hence, 1.5 mol% was the optimum doping concentration for the Dy doped glass sample.

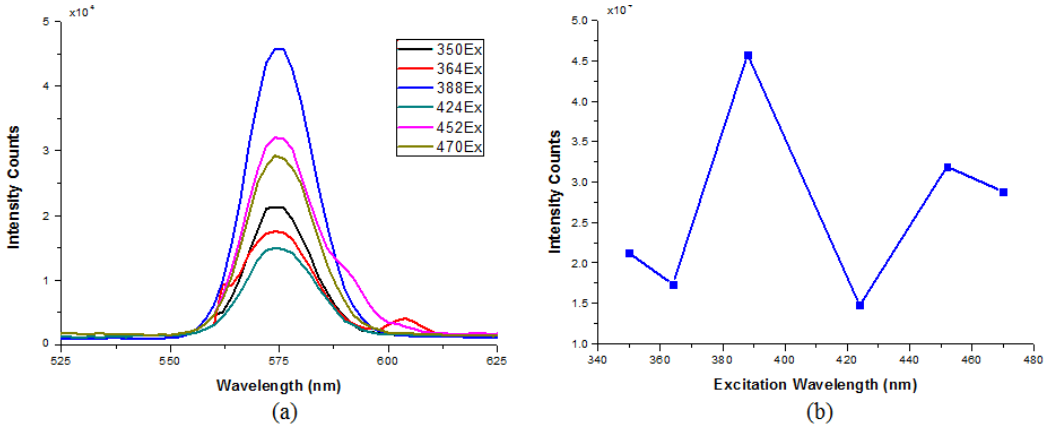

Figure 5.22: (a) Emission spectra of 1.5 mol% Dy for different excitation wavelengths and (b) Intensity variation of 575 nm emissions for different Dy concentrations under 452 nm excitation

Furthermore, to analyse the effect of different excitation wavelengths on the photoluminescence intensity of Dy doped BSG waveguide, the emission scan was recorded for different excitation wavelengths as depicted in Figure 5.22 (a). In Figure 5.22 (b), the respective variation in photoluminescence intensity is plotted as a function of excitation wavelengths corresponding to the 575 nm Dy emission. For the 6 excitation wavelengths tried, the highest photoluminescence intensity was obtained for 388 nm excitation followed by 452, 470, 350, 364 and 424 nm.

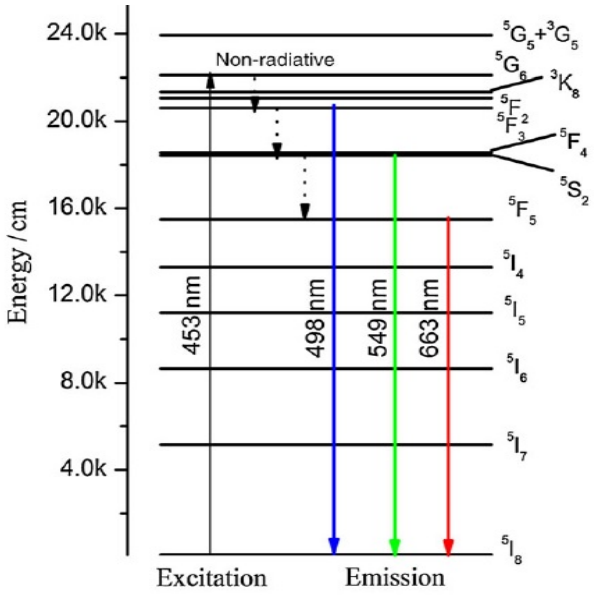

Figure 5.23: Energy level diagram corresponding to Ho^{3+} [48]

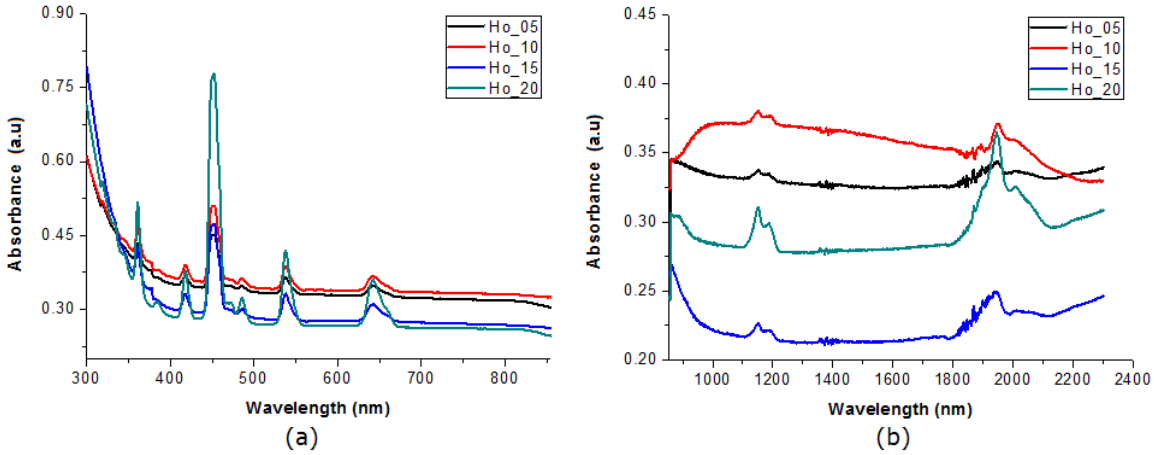

Figure 5.24: Absorption spectrum of different concentrations of Ho doped ZBSG: (a) Visible range, (b) NIR range

The energy level diagram for Ho is shown in figure 5.23. Figure 5.24 shows the absorption spectrum of Ho doped ZBSG covering the UV, VIS and NIR wavelengths. Many weak and sharp absorption peaks can be observed within the spectrum. The different Ho signature peaks are located around the wavelengths: 360 nm ($^5I_8 \rightarrow {}^3H_5 + {}^3H_6\,(^5G_2)$), 378 nm ($^5I_8 \rightarrow {}^5G_4$), 418 nm($^5I_8 \rightarrow {}^5G_5$), 452 nm($^5I_8 \rightarrow {}^5G_6 + {}^5F_1$), 486 nm($^5I_8 \rightarrow {}^5F_3$), 538 nm($^5I_8 \rightarrow {}^5S_2 + {}^5F_4$), 642 nm ($^5I_8 \rightarrow {}^5F_5$), 888 nm ($^5I_8 \rightarrow {}^5I_5$), 1151 nm ($^5I_8 \rightarrow {}^5I_6$), 1947 nm ($^5I_8 \rightarrow {}^5I_7$) [49-51].

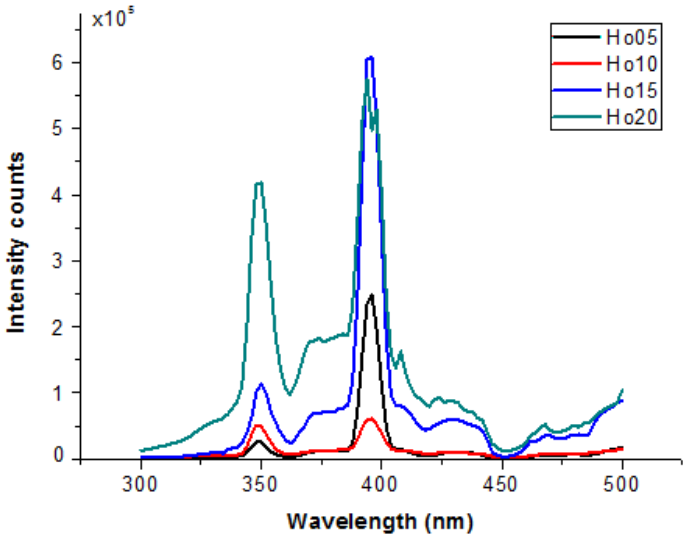

Figure 5.25: Excitation spectra for different Ho concentrations corresponding to 532 nm photoluminescence emission

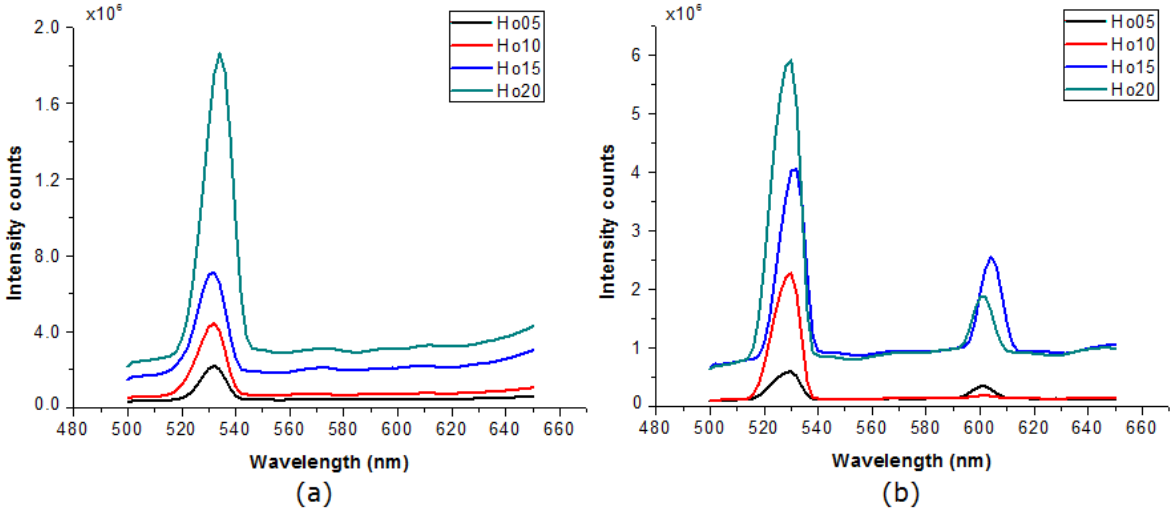

Figure 5.26: Emission spectra for different Ho concentrations (a) for 348 nm excitation and (b) for 394 nm excitation

The excitation spectra acquired in the wavelength range 300-500 nm corresponding to 532 nm photoluminescence emission for different concentrations of Ho doped ZBSG is shown in Figure 5.25. The excitation scan identified two peaks at wavelengths 348 nm and 394 nm. Figures 5.26 (a) and (b) shows the emission scan for 348 nm and 394 nm excitations respectively. With 348 nm excitation only green emission (532 nm) was obtained owing to ${}^5S_2 + {}^5F_4 \rightarrow {}^5I_8$ energy level transition. On the other hand, using 394 nm excitation

two emission peaks were obtained at 532 nm ($^5S_2 + {}^5F_4 \rightarrow {}^5I_8$) and around 606 nm ($^5F_5 \rightarrow {}^5I_8$) [52].

Further photoluminescence studies carried out on Ho doped glass produced 550 nm emission ($^5S_2 + {}^5F_4 \rightarrow {}^5I_8$) corresponding to 364 nm excitation and 658 nm emission ($^5F_5 \rightarrow {}^5I_8$) for 328 nm excitation wavelength [53-54].

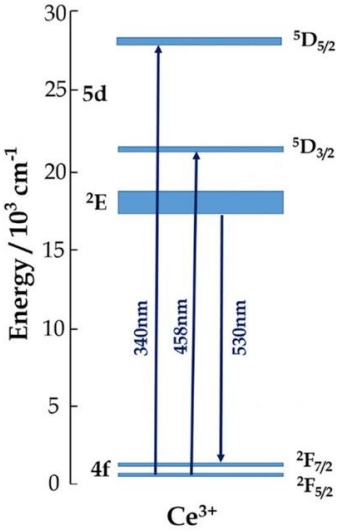

Figure 5.27: Energy level diagram corresponding to Ce^{3+} [55]

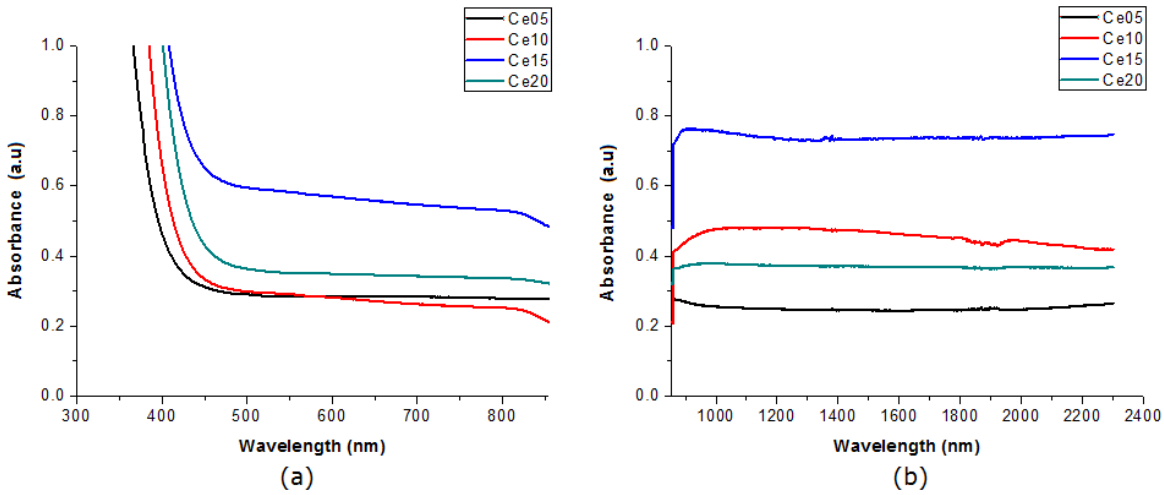

Figure 5.28: Absorption spectrum of different concentrations of Ce doped ZBSG: (a) Visible range and (b) NIR range

The energy level diagram for Ce is shown in Figure 5.27. Figure 5.28 shows the absorption spectrum of Ce doped ZBSG in the visible and NIR wavelengths range. As can be observed from Figure 5.28 (a), Ce doped ZBSG shows a very strong absorption close to 350 nm wavelength due to 5d-4f transition [56].

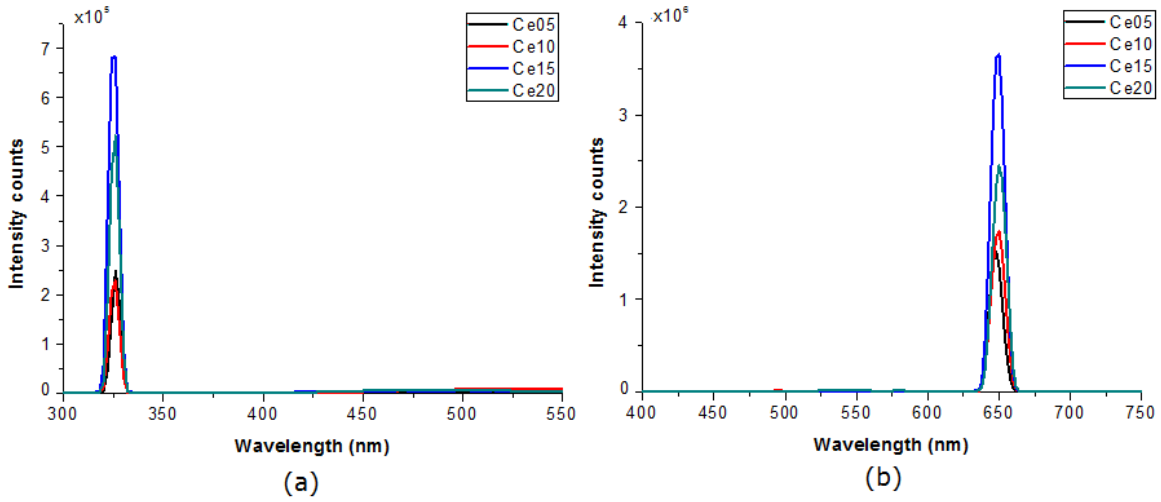

Figure 5.29: Emission spectra for different Ho concentrations for 348 nm excitation

Figure 5.29 shows the photoluminescence emission spectrum of Ce doped ZBSG corresponding to 348 nm excitation. It was observed that for 325 nm excitation, 650 nm emission was obtained [57-58].

5.7 Photoluminescence spectroscopy-based temperature studies of rare earth doped glasses

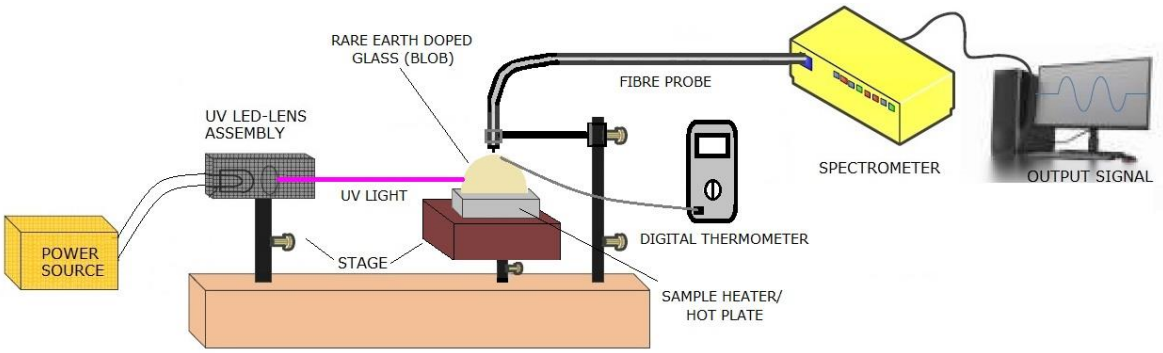

Figure 5.30: Schematic picture of experimental setup used for photoluminescence spectroscopy-based temperature sensing

Figure 5.30 shows the schematic picture of the experimental setup used for rare earth photoluminescence-based temperature sensing.

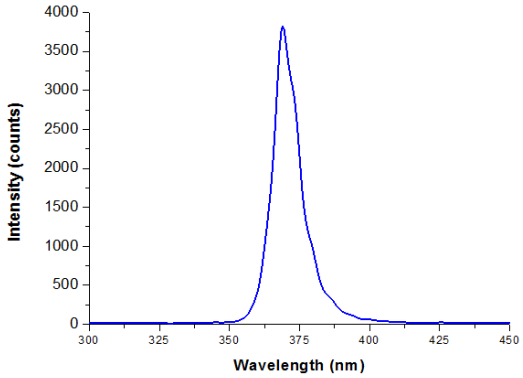

Figure 5.31: UV LED excitation spectra with peak at 370 nm

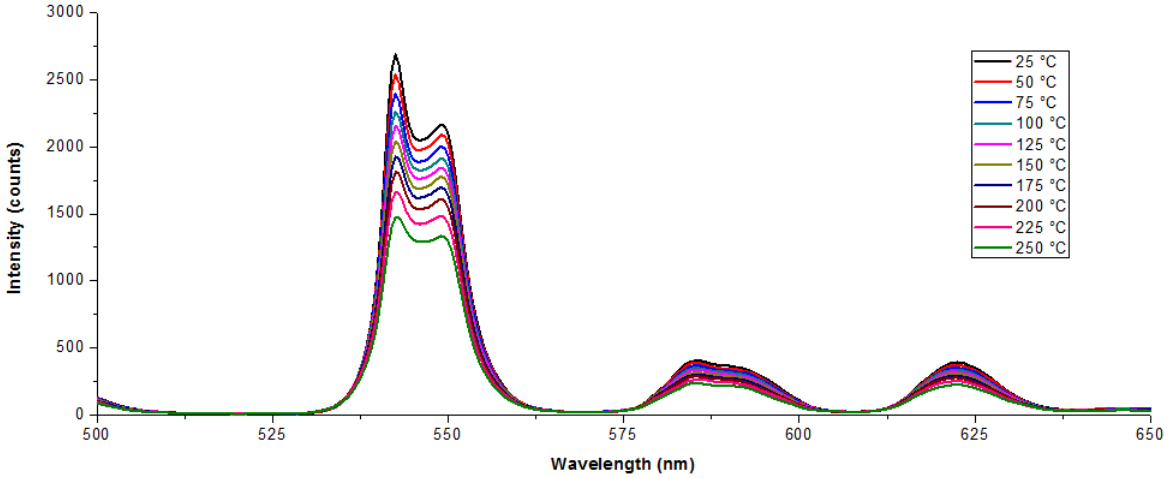

Figure 5.32: Photoluminescence emission spectra of Tb doped ZBSG corresponding to different temperatures

Figure 5.32 depicts the optical photoluminescence spectra of the Tb doped glass for 370 nm UV LED excitation (Figure 5.31). The Tb characteristic photoluminescence green emission peak was obtained at 544 nm, corresponding to the $^5D_4 \rightarrow {}^7F_5$ transition [33]. Temperature studies carried out on the UV excited Tb glass sample demonstrated a linear trend, as can be observed in the graph shown in Figure 5.33. Tb doped glass was characterised for higher temperatures in the range 20-250 °C and followed the linear trend throughout. The most intense 543 nm Tb peak is characterised by a narrower emission line as opposed to other peaks in the $^5D_4 \rightarrow {}^7F_J$ series [50]. Furthermore, the electron-phonon coupling strength and phonon energy of Tb doped glass is also higher [59].

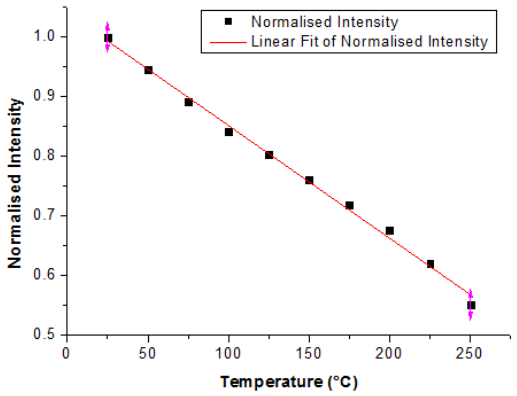

Figure 5.33: Normalised photoluminescence intensity (I_signal/I_max) vs temperature change of Tb doped ZBSG

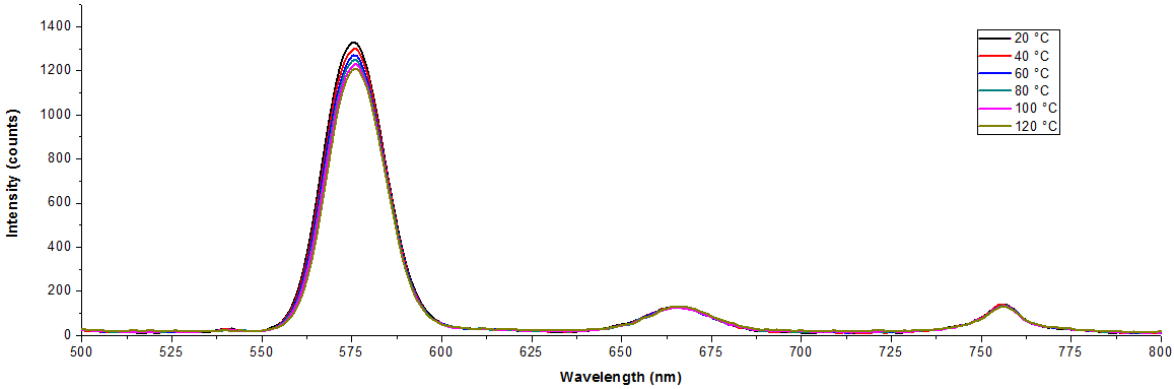

Figure 5.34: Photoluminescence emission spectra of Dy doped ZBSG corresponding to different temperatures

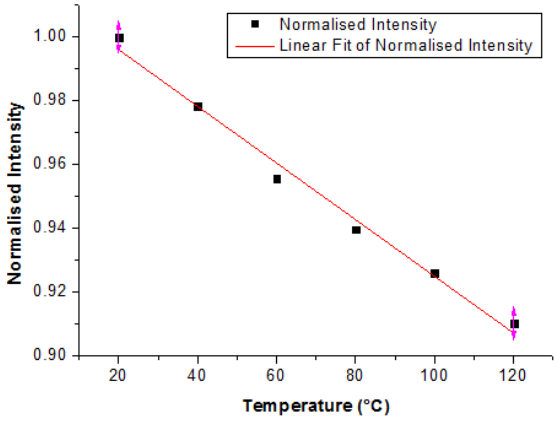

Figure 5.35: Normalised photoluminescence intensity (I_signal/I_max) vs temperature change of Dy doped ZBSG

Figure 5.34 shows the photoluminescence spectra of Dy doped glass for 370 nm UV LED excitation. The yellowish Dy characteristic photoluminescence was obtained at 575 nm, corresponding to $^4F_{9/2} \rightarrow {}^6H_{13/2}$ transition. Though the temperature studies carried out on the UV excited Dy glass sample demonstrated a linear trend, (Figure 5.35), however the sensitivity was

comparatively lower, and the photoluminescence signal intensity drop was not very significant. This can be due to the lower thermal coupling between the ${}^4F_{9/2} - {}^6H_{13/2}$ energy levels. Moreover, the energy difference between level ${}^6H_{15/2}$ and ${}^4F_{9/2}$ of Dy^{3+} (478 nm emission) is around 1000 cm^{-1} which is within the thermal coupling range (200-2000 cm^{-1}), which would be better for temperature sensing applications [60].

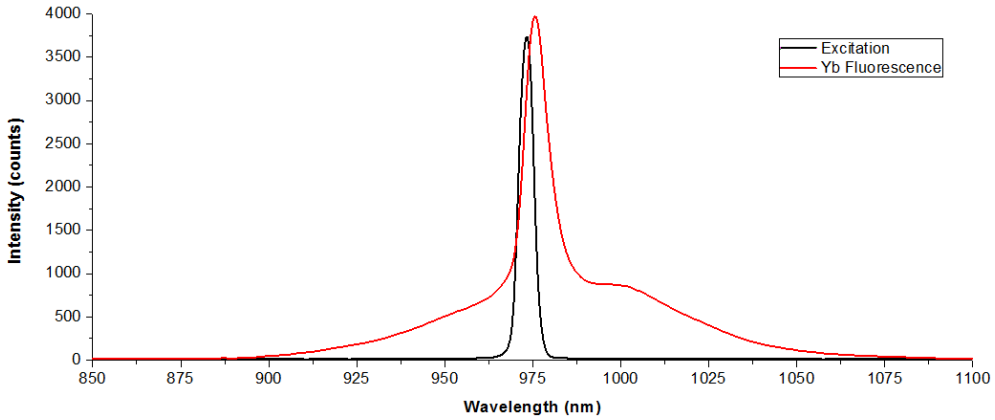

Figure 5.36: Excitation and photoluminescence emission spectra of Yb doped ZBSG

Figure 5.36 shows the excitation and photoluminescence emission peaks of Yb doped glass sample A laser diode with centre wavelength 974 nm was used as excitation source. As the excitation and emission wavelength ranges of Yb was close-by, the emission signal was collected at an orthogonal point from the excitation plane, in order to avoid source signal. The Yb photoluminescence emission peak was obtained around 975 nm corresponding to ${}^2F_{5/2}$ to ${}^2F_{7/2}$ transitions [61-62] along with a sideband in the 1000 nm range.

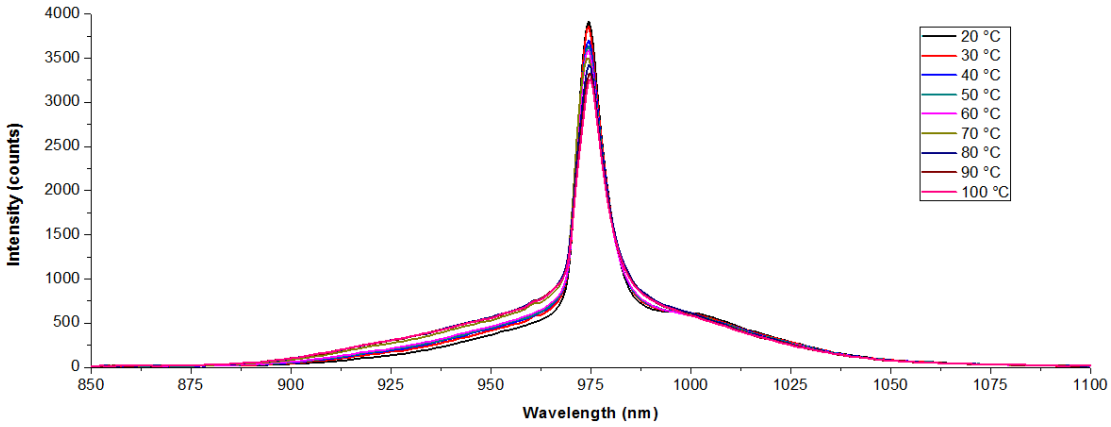

Figure 5.37: Photoluminescence emission spectra of Yb doped ZBSG corresponding to different temperatures

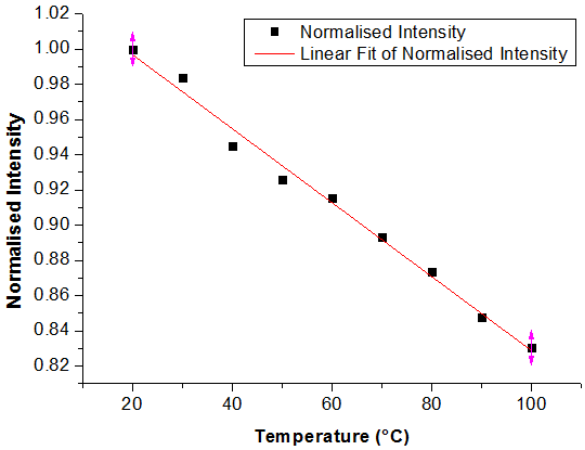

Figure 5.38: Normalised photoluminescence intensity (I_signal/I_max) vs temperature change of Yb doped ZBSG

Figure 5.37 shows the photoluminescence spectra of Yb doped glass sample for 974 nm laser diode excitation. The Yb characteristic photoluminescence was obtained at 975 nm. The triply ionized Yb ion (Yb^{3+}) has only two levels, one ground state $(^2F_{7/2})$ and other excited state $(^2F_{5/2})$ separated by ~10,000 cm^{-1} and the temperature sensitivity arises from the Stark components within the sublevels in $^2F_{5/2}$ [15]

The temperature studies carried out on the Yb glass sample also demonstrated a linear trend, as can be observed in the graph shown in Figure 5.38, however the sensitivity was lower compared the Tb glass samples as the photoluminescence signal intensity drop was not very significant. This is

because, the electron-phonon coupling of Tb^{3+} is higher compared to other rare earths due to the low energy of their $4f^{n-1}\,5d$ state [13].

5.8 Characterisation of Tb doped fibre

In this section, the characterisation of the Tb doped optical fibre developed is carried out. The doped fibre was obtained using the fibre drawing technique of rare earth doped glass preforms. Figure 5.39 shows the SEM images corresponding to the cross-sectional and lateral view of the developed Tb doped fibre. From the SEM images, the circular waveguide diameter was measured to be around 50 µm.

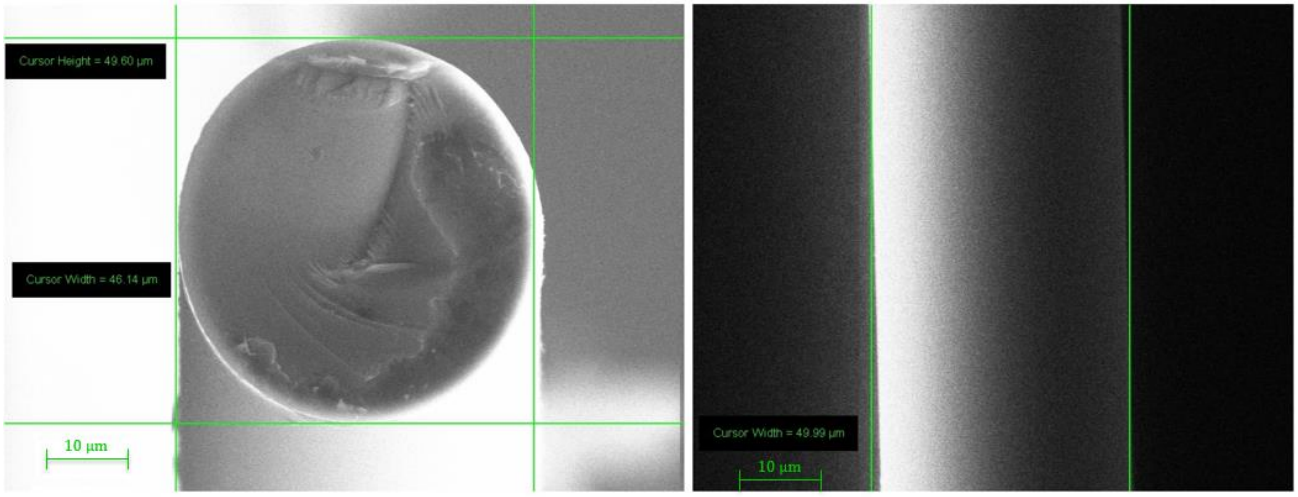

Figure 5.39: SEM images showing the (a) cross-section and (b) lateral view of the rare earth doped waveguide

In Figure 5.40, a green photoluminescence emission can be observed from the Tb doped fibre ($\lambda_{em} = 544\,nm$), when irradiated using a UV LED of peak wavelength, λ_p=385 nm.

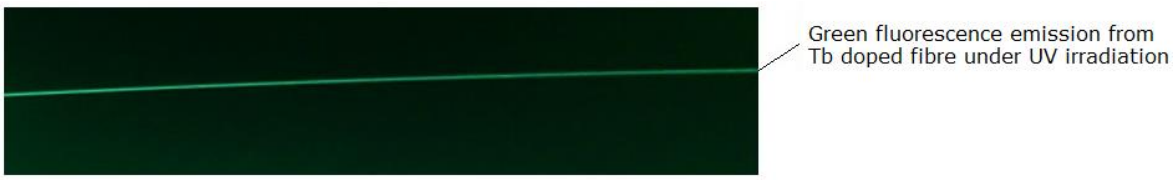

Figure 5.40: Green photoluminescence emission from Tb doped fibre when irradiated using UV LED in a dark room

5.9 Summary

The investigations carried out in this chapter provided many new insights for rare earth doped glass materials. These insights can be utilised within the new sensor configuration consisting of rare earth doped microstructured FBG for the development of the multimodal sensor with improved SNR and enhanced sensitivity needed for the O&G industry. The various spectroscopic investigations carried out on the synthesised rare earth doped samples identified the possibility of signal intensity enhancement through optimum rare earth doping concentrations and appropriate signal excitation. Signal enhancement will contribute to the overall SNR improvement. Furthermore, the temperature dependant studies carried out on different rare earth doped glasses identified its suitability for O&G high temperature applications. The different rare earth doped glasses exhibited different levels of sensitivity to the temperature changes, among which Tb doped glasses depicted the highest sensitivity. The obtained results show a promising future for the rare earth doped fibre optic sensors for O&G applications. Furthermore, the integrated sensor configuration consisting of rare earth doped PCF-FBG further improves the sensor capabilities in terms of multi-point multimodal sensing, SNR enhancement and reduced cross sensitivities. The following Chapter 6 will investigate the Raman signatures of different rare earth doped glasses and how it can be utilised for O&G DTS applications in the multimodal fibre optic sensor configuration.

5.10 References

[1] Potter BG, Sinclair MB. Photosensitive and Rare-Earth Doped Ceramics for Optical Sensing: A Review. *Journal of Electroceramics.* 1998; 2(4):295-308.

[2] Hewak D. *Properties, processing and applications of glass and rare earth-doped glasses for optical fibres.* London: IEE, INSPEC; 1998.

[3] Myers JD, Wu R, Chen T, Myers MJ, Hardy CR, Driver JK, et al. New high-power rare-earth-doped fiber laser materials and architectures. *Advances in Fiber Lasers*: International Society for Optics and Photonics. 2003; 177-184.

[4] Quoi KW, Lieberman RA, Cohen LG, Shenk DS, Simpson JR. Rare-earth doped optical fibers for temperature sensing. *Journal of Lightwave Technology.* 1992; 10(6):847-852.

[5] Jha A, Jiang X, Lousteau J, Richards B, Li H, Macpherson WN, et al. Recent advances in mid-IR optical fibres for chemical and biological sensing in the 2-15μm spectral range. *Photonics North 2009*: International Society for Optics and Photonics. 2009; 73860V: 1-11.

[6] Vasconcelos HC, Pinto AS. Fluorescence Properties of Rare-Earth-Doped Sol-Gel Glasses. *Recent Applications in Sol-Gel Synthesis.* InTech; 2017.

[7] Albrecht C. Joseph R. Lakowicz: Principles of fluorescence spectroscopy. *Analytical and Bioanalytical Chemistry.* 2008; 390(5):1223-1224.

[8] Albani JR. *Structure and dynamics of macromolecules: absorption and fluorescence studies.* Elsevier; 2011.

[9] Ishikawa-Ankerhold H, Ankerhold R, Drummen G. *Advanced Fluorescence Microscopy Techniques-FRAP, FLIP, FLAP, FRET and FLIM.* Molecules. 2012;17(4):4047-132.

[10] Sauer M, Hofkens J, Enderlein J. Basic principles of fluorescence spectroscopy. *Handbook of fluorescence spectroscopy and imaging: From single molecules to ensembles.* 2011; 1-30.

[11] Walsh BM. Judd-Ofelt theory: principles and practices. Advances in spectroscopy for lasers and sensing, *Springer*. 2006; 403-433.

[12] Bünzli JC, Eliseeva SV. Basics of lanthanide photophysics. *Lanthanide Luminescence, Springer, Berlin*. 2010; 1-45

[13] Yu D, Ballato J, Riman RE. Temperature-dependence of multiphonon relaxation of rare-earth ions in solid-state hosts. *The Journal of Physical Chemistry C.* 2016;120(18):9958-64.

[14] Meijerink A, Blasse G, Sytsma J, de Mello Donegá C, Ellens A. Electron-phonon coupling in rare earth compounds. *Acta Physica Polonica A.* 1996;1(90):109-19.

[15] Pandey A, Rai VK, Dwivedi Y, Rai SB, Singh JP. Rare earth doped materials for temperature sensors. *Spectroscopic Techniques for Security Forensic and Environmental Applications.* 2014:279-92.

[16] Yadav AK, Singh P. A review of the structures of oxide glasses by Raman spectroscopy. *RSC Advances.* 2015; 5(83):67583-67609.

[17] Khimich N, Berdichevskii G, Poddenezhnyi E, Golubkov V, Boiko A, Ken'Ko V, et al. Sol-gel synthesis of an optical silica glass doped with rare-earth elements. *Glass Physics and Chemistry.* 2007; 33(2):152-155.

[18] Kurkjian CR, Prindle WR. Perspectives on the history of glass composition. *Journal of the American Ceramic Society.* 1998; 81(4):795-813.

[19] Hamilton EH, Waxler R, Nivert J. Properties of zinc borosilicate glasses. *Journal of Research of the National Bureau of Standards.* 1959; 62(2):59-62.

[20] Mohd Fudzi F, Mohamed Kamari H, Abd Latif A, Muhammad Noorazlan A. Linear Optical Properties of Zinc Borotellurite Glass Doped with Lanthanum Oxide Nanoparticles for Optoelectronic and Photonic Application. *Journal of Nanomaterials.* 2017; 2017.

[21] Lopez-Iscoa P, Petit L, Massera J, Janner D, Boetti NG, Pugliese D, et al. Effect of the addition of Al2O3, TiO2 and ZnO on the thermal, structural and

luminescence properties of Er3 -doped phosphate glasses. *Journal of Non-Crystalline Solids.* 2017; 460:161-168.

[22] Dong ZN, Wu YS, Wang Z, He A, Li M, Chen M, Du H, Ma Q, Liu T. Effect of temperature on the photoproperties of luminescent terbium sensors for homogeneous bioassays. *Luminescence.* 2013;28(2):156-61.

[23] Johny J, Bhavsar K, Officer S, Adams M and Prabhu R. Waveguide-based machine readable fluorescence security feature for border control and security applications. *Counterterrorism, Crime Fighting, Forensics, and Surveillance Technologies II*: International Society for Optics and Photonics; 2018. p. 1080209.

[24] Nkwoada A, Officer S. Novel Dysprosium and Terbium Doped Taggants for Hydrocarbon Identification. *Journal of Advanced Chemical Sciences.* 2016; :296-298.

[25] Swinehart D. The beer-lambert law. *Journal of Chemical Education.* 1962; 39(7):333.

[26] Fuwa K, Valle B. The Physical Basis of Analytical Atomic Absorption Spectrometry. The Pertinence of the Beer-Lambert Law. *Analytical Chemistry.* 1963; 35(8):942-946.

[27] Dieke GH. Spectra and energy levels of rare earth ions in crystals. *American Journal of Physics.* 1970;38(3):399-400.

[28] Zmojda J, Kochanowicz M, Miluski P, Dorosz D. Side-detecting optical fiber doped with Tb3 for ultraviolet sensor application. *Fibers.* 2014; 2(2):150-157.

[29] Caldino U, Speghini A, Berneschi S, Bettinelli M, Brenci M, Pelli S, et al. Optical spectroscopy and waveguide fabrication in Sm3 /Tb3 doped zinc–sodium–aluminosilicate glasses. *Optical Materials.* 2012; 34(7):1067-1071.

[30] Lin H, Meredith G, Jiang S, Peng X, Luo T, Peyghambarian N, et al. Optical transitions and visible upconversion in Er 3 doped niobic tellurite glass. *Journal of Applied Physics.* 2003; 93(1):186-191.

[31] Nandi P, Jose G. Spectroscopic properties of Er3 doped phospho-tellurite glasses. *Physica B: Condensed Matter.* 2006; 381(1-2):66-72.

[32] Kaky KM, Lakshminarayana G, Baki S, Lira A, Caldiño U, Meza-Rocha A, et al. Structural and optical studies of Er3 -doped alkali/alkaline oxide containing zinc boro-aluminosilicate glasses for 1.5 μm optical amplifier applications. *Optical Materials.* 2017; 69:401-419.

[33] Goyal P, Sharma YK, Pal S, Bind UC, Huang S, Chung S. The effect of SiO2 content on structural, physical and spectroscopic properties of Er3 doped B2O3–SiO2–Na2O–PbO–ZnO glass systems. *Journal of Non-Crystalline Solids.* 2017; 463:118-127.

[34] Chen F, Xu S, Wei T, Wang F, Cai M, Tian Y, et al. Mid-infrared emission and Raman spectra analysis of Er 3 -doped oxyfluorotellurite glasses. *Applied Optics.* 2015; 54(11):3345-3352.

[35] Venkata Krishnaiah K, Rajeswari R, Upendra Kumar K, Surendra Babu S, Martín IR, Jayasankar CK. Spectroscopy and radiation trapping of Yb3+ions in lead phosphate glasses. *Journal of Quantitative Spectroscopy and Radiative Transfer.* 2014; 140:37-47.

[36] Pinheiro A, Freitas A, Silva G, Bell M, Anjos V, Carmo A, et al. Laser performance parameters of Yb3 doped UV-transparent phosphate glasses. *Chemical Physics Letters.* 2014; 592:164-169.

[37] Dai N, Hu L, Yang J, Dai S, Lin A. Spectroscopic properties of Yb3 -doped silicate glasses. *Journal of Alloys and Compounds.* 2004; 363(1-2):1-5.

[38] Sontakke AD, Biswas K, Annapurna K. Concentration-dependent luminescence of Tb3 ions in high calcium aluminosilicate glasses. *Journal of Luminescence.* 2009; 129(11):1347-1355.

[39] Hussain NS, Reddy YP, Buddhudu S. Emission properties of Tb3 -doped zinc boro-silicate glasses. *Materials Letters.* 2001; 48(5):303-308.

[40] Kaczmarek F, Malak H. Lifetime Measurements of the $4S_{3/2}$ Level in Erbium Pentaphosphate Monocrystal. *Acta Physica Polonica-Series A General Physics.* 1996; 89(5):669-674.

[41] Lakshminarayana G, Qiu J, Brik M, Kumar G, Kityk I. Spectral analysis of RE3 (RE= Er, Nd, Pr and Ho): GeO2–B2O3–ZnO–LiF glasses. *Journal of Physics: Condensed Matter.* 2008; 20(37):375104.

[42] Paez G, Strojnik M. Erbium-doped optical fiber fluorescence temperature sensor with enhanced sensitivity, a high signal-to-noise ratio, and a power ratio in the 520–530-and 550–560-nm bands. *Applied Optics.* 2003; 42(16):3251-3258.

[43] Chiodini N, Fasoli M, Martini M, Morazzoni F, Rosetta E, Scotti R, et al. Rare-earth doped sol-gel silicate glasses for scintillator applications. *Radiation Effects and Defects in Solids.* 2003; 158(1-6):463-467.

[44] Rao V, Satyanarayana T, Veeraiah N. Spectroscopic studies of Dy3 ion doped tellurite glasses for solid state lasers and white LEDs. *Spectrochimica Acta Part A: Molecular and Biomolecular Spectroscopy.* 2018; 188:516-524.

[45] Suthanthirakumar P, Marimuthu K. Investigations on spectroscopic properties of Dy3 doped zinc telluro-fluoroborate glasses for laser and white LED applications. *Journal of Molecular Structure.* 2016; 1125:443-452.

[46] Thomas V, Jose G, Jose G, Biju P, Rajagopal S, Unnikrishnan N. Structural evolution and fluorescence properties of Dy3: silica matrix. *Journal of Sol-Gel Science and Technology.* 2005; 33(3):269-274.

[47] Lakshminarayana G, Qiu J. Photoluminescence of Pr3, Sm3 and Dy3 - doped SiO2–Al2O3–BaF2–GdF3 glasses. *Journal of Alloys and Compounds.* 2009; 476(1-2):470-476.

[48] Rajesh D, Dhamodhara Naidu M, Ratnakaram Y, Balakrishna A. Ho3 - doped strontium–aluminium–bismuth–borate glasses for green light emission. *Luminescence.* 2014; 29(7):854-860.

[49] Rejikumar P, Vasudevan P, Karthika S, George J, Unnikrishnan N. Structural and spectroscopic characterization of Ho3 in sol-gel silica. *Journal of Optoelectronics and Advanced Materials.* 2010; 12(5):1065-1070.

[50] Wang X, Hu L, Xu W, Wang S, Zhang L, Yu C, et al. Spectroscopic properties of Ho3+ and Al3+ co-doped silica glass for 2-μm laser materials. *Journal of Luminescence.* 2015; 166:276-281.

[51] Zhang W, Yu D, Zhang J, Qian Q, Xu S, Yang Z, et al. Near-infrared quantum splitting in Ho3:LaF3 nanocrystals embedded germanate glass ceramic. *Optical Materials Express.* 2012; 2(5):636-643.

[52] Prasad VR, Damodaraiah S, Devara S, Ratnakaram Y. Photoluminescence studies on holmium (III) and praseodymium (III) doped calcium borophosphate (CBP) phosphors. *Journal of Molecular Structure.* 2018; 1160:383-392.

[53] Damak K, Al-Shihri A, Seo H, Rüssel C, Maâlej R. Quantifying Raman and emission gain coefficients of Ho3 doped TeO2· ZnO· PbO· PbF2· Na2O (TZPPN) tellurite glass. *Solid State Sciences.* 2014; 28:74-80.

[54] Rajesh D, Dhamodhara Naidu M, Ratnakaram Y, Balakrishna A. Ho3 -doped strontium–aluminium–bismuth–borate glasses for green light emission. *Luminescence.* 2014; 29(7):854-860.

[55] Ma R, Ma C, Zhang J, Long J, Wen Z, Yuan X, et al. Energy transfer properties and enhanced color rendering index of chromaticity tunable green-yellow-red-emitting $Y_3Al_5O_{12}$: Ce^{3+}, Cr^{3+} phosphors for white light-emitting diodes. *Optical Materials Express.* 2017; 7(2):454-467.

[56] Liu L, Shao C, Zhang Y, Liao X, Yang Q, Hu L, et al. Scintillation properties and X-ray irradiation hardness of Ce3+-doped Gd2O3-based scintillation glass. *Journal of Luminescence.* 2016; 176:1-5.

[57] Le Toquin R, Cheetham A. Red-emitting cerium-based phosphor materials for solid-state lighting applications. *Chemical Physics Letters.* 2006; 423(4-6):352-356.

[58] Ghosh D, Karmakar P, Biswas K, Balaji S, Sontakke AD, Annapurna K. Variance of energy transfer dynamics in Ce3 sensitized Eu3 and Tb3 doped alkali free Ba–Al metaphosphate glass: role of the host matrix. *Physics and Chemistry of Glasses-European Journal of Glass Science and Technology Part B.* 2014; 55(5):196-206.

[59] Ebendorff-Heidepriem H, Ehrt D. Spectroscopic properties of Eu3+ and Tb3+ ions for local structure investigations of fluoride phosphate and phosphate glasses. *Journal of non-crystalline solids.* 1996;208(3):205-16.

[60] Cao Z, Zhou S, Jiang G, Chen Y, Duan C, Yin M. Temperature dependent luminescence of Dy3+ doped BaYF5 nanoparticles for optical thermometry. *Current Applied Physics.* 2014;14(8):1067-71.

[61] Dong J, Bass M, Mao Y, Deng P, Gan F. Dependence of the Yb 3 emission cross section and lifetime on temperature and concentration in yttrium

aluminum garnet. *Journal of the Optical Society of America* B. 2003; 20(9):1975-1979.

[62] Nandi P, Jose G. Superfluorescence from Yb-and Yb–Er-doped phosphotellurite glass fibres. *Optical Fiber Technology.* 2008; 14(4):275-280.

6. RAMAN SPECTROSCOPIC INVESTIGATIONS ON RARE EARTH DOPED GLASSES

6.1 Introduction

Rare earth materials possess some specific Raman signatures and spectral bands associated with them, in addition to the photoluminescence phenomena. Rare earth elements when doped into the glass host matrix introduces a change in their electronic energy level structure and thereby modifies its optical properties. The Raman lines/transitions have got a well-defined temperature dependency and the spectral bands associated with Raman effect is known as thermal bands. Hence, rare earth doped silica glass composition is a promising material for Raman based fibre-optic distributed temperature sensing (DTS).

The main advantage of Raman DTS is that it enables real-time measurement of the spatial distribution of temperature [1]. Furthermore, rare earth materials show high sensitivity for utilisation in DTS systems [2]. Moreover, Raman distributed sensors are not strain sensitive as the Raman anti-Stokes signal is insensitive to strain vibrations [3-5]. Hence, Raman scattering would be an ideal choice for distributed sensing if temperature is the only parameter of interest and the cross-sensitivity issues can be avoided. Also, Raman scattering based DTS systems have higher temperature sensitivity than that of Brillouin scattering-based systems [6]. With reference to the Rayleigh scattering peak, the anti-Stokes component (refer Figure 6.2) is temperature sensitive for the Raman scattering. However, the Stokes and the anti-Stokes components of the Brillouin scattering are temperature and strain sensitive [7-8].

Despite all these advantages, one main limitation of Raman DTS is the weak Raman signal intensity. Hence, this chapter focuses on the investigations carried

out on rare earth doped glass materials for fibre optic sensors, with the aim of achieving Raman signal intensity enhancement through rare earth doping and attaining multi-parameter distributed sensing. Raman spectroscopic studies has been carried out on different rare earth doped glasses in order to identify the temperature sensitive Raman bands and analyse the effect of rare earth concentrations on the Raman signal intensity. Detailed investigations were carried out to identify if the Raman peaks of glass (silica) as well as the rare earth signature Raman peaks are enhancing with increasing rare earth concentrations.

6.2 Theoretical Background

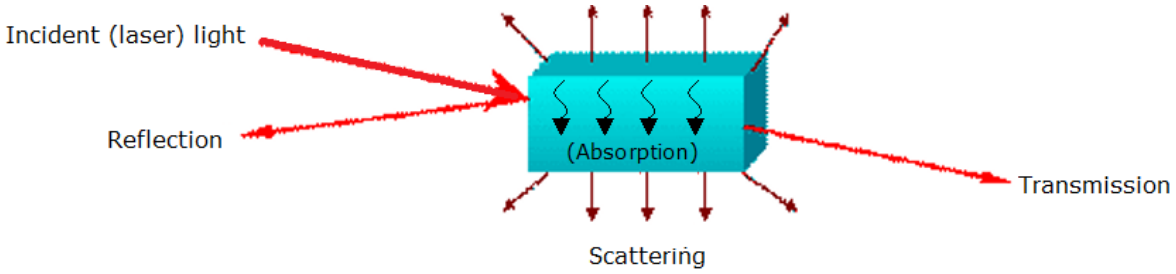

Figure 6.1: Illustration of the four reactions of light incident on a surface or medium

When light enters any medium, there are different possibilities (Figure 6.1): the light or electromagnetic radiation can merely undergo transmission or propagation without any interaction with the medium, it can experience reflection, it can have absorption and also scattering in the process of light-matter interaction. Most of these optical phenomena are utilised for different optical sensing applications.

As shown in Figure 6.2, the spectrum of backscattered light in optical fibres can mainly have three scattering components: Rayleigh, Raman and Brillouin [9]. Energy level transitions occur with the absorption and emission of a photon through the generation or recombination electron-hole pairs. The photo-excited

electron-hole pair can experience elastic scattering from the impurities or defects in the material before undergoing recombination, known as Rayleigh scattering mechanism. Rayleigh scattering is an energy conserving light scattering process as the molecule scatters exactly the same energy as incident light (as can be seen from Figure 6.3). Another possibility is inelastic light scattering wherein some energy transfers from the electrons to phonons.

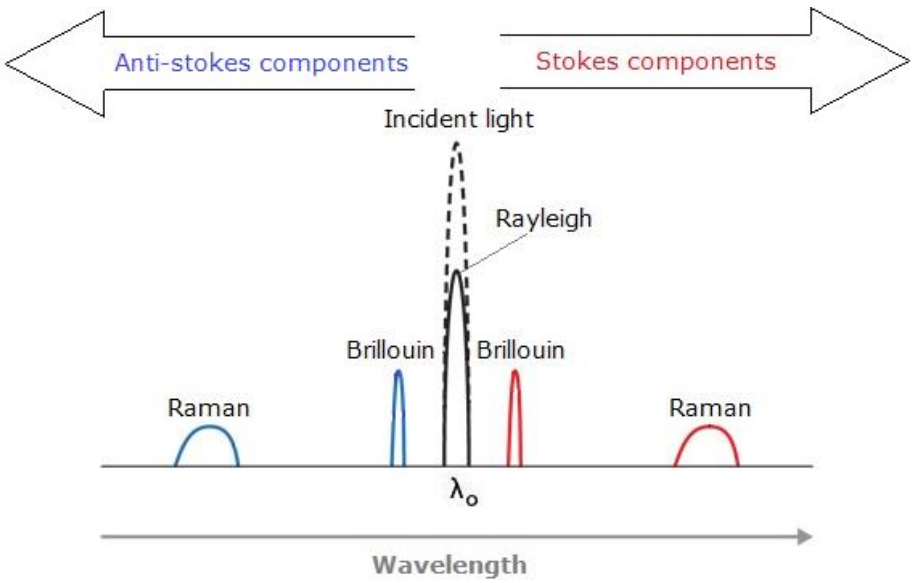

Figure 6.2: Spectral profile of Rayleigh, Raman and Brillouin scattering mechanisms

Raman and Brillouin are non-linear light scatterings, which comes under inelastic light scattering mechanism. The fundamental difference is that optical phonons are responsible for Raman scattering and acoustic phonons are responsible Brillouin scattering [10-11]. A phonon is defined as a quantum or definite discrete unit of vibrational mechanical energy, which arises due to the oscillations of atoms in the crystal lattice. The atom, owing to their own thermal energy or other external forces creates lattice vibrations, which in turn generates mechanical waves that transmits as heat and sound through the material.

The scattered light has a wavelength different from the incident light and has got 2 spectral components: anti-Stokes and Stokes components. In anti-Stokes scattering, the particle may lose some of its energy and the emitted photon will have a shorter wavelength than the incident photon. Whereas, in Stokes scattering, the particle absorbs energy and the emitted photon will have a wavelength longer than the incident photon.

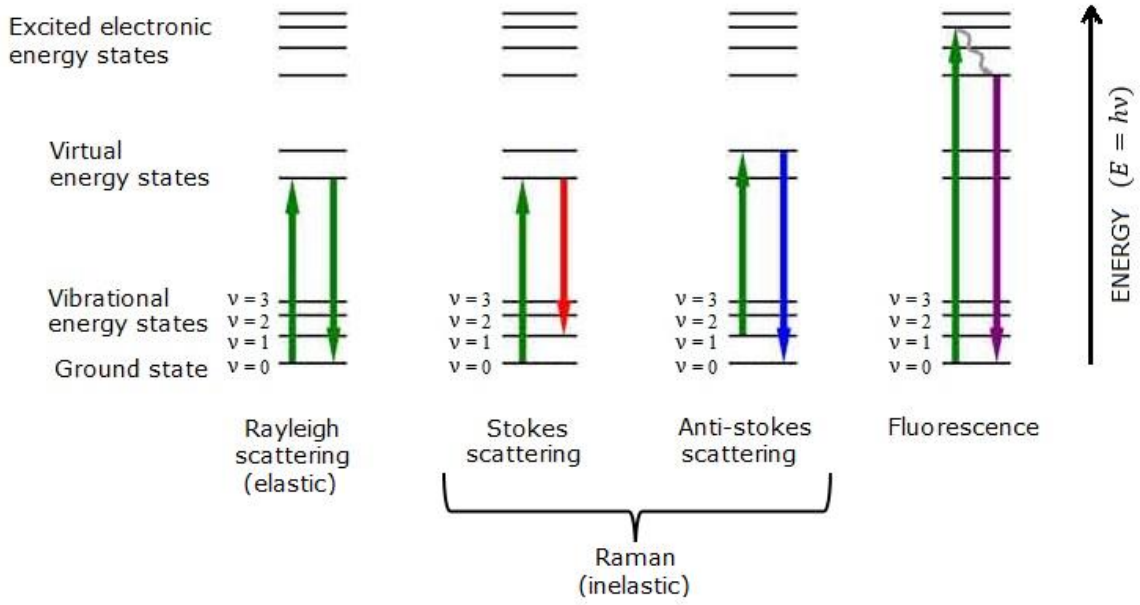

Figure 6.3: Energy level diagram showing: (a) Rayleigh scattering, (b) Raman Stokes scattering, (c) Raman anti-Stokes scattering and (d) fluorescence

In Raman spectroscopy the photon interacts with a molecule in its ground vibronic state or an excited vibronic state and the molecule makes a brief transition to a virtual energy state (imaginary intermediate state). The scattered emitted photon can be of lower energy (Stokes shift) than the incoming photon, leaving the molecule in an excited vibrational state. They can also have a transition from a vibrationally excited state to the virtual state. The molecule will then return to its ground-state, with the scattered photon carrying away more energy than the incident photon. This is called anti-Stokes scattering. Fluorescence or photoluminescence occurs due to real electronic transitions. On the other hand, Raman scattering occurs as a result of virtual electronic-

vibrational transitions. Raman shift ($\bar{\nu}$) is the energy difference between the initial and final vibrational levels and is given by [12]:

$$\bar{\nu}\,(cm^{-1}) = \frac{1}{\lambda_{incident}} - \frac{1}{\lambda_{scattered}} \qquad (1)$$

6.3 Fabrication of rare earth doped sol-gel glasses

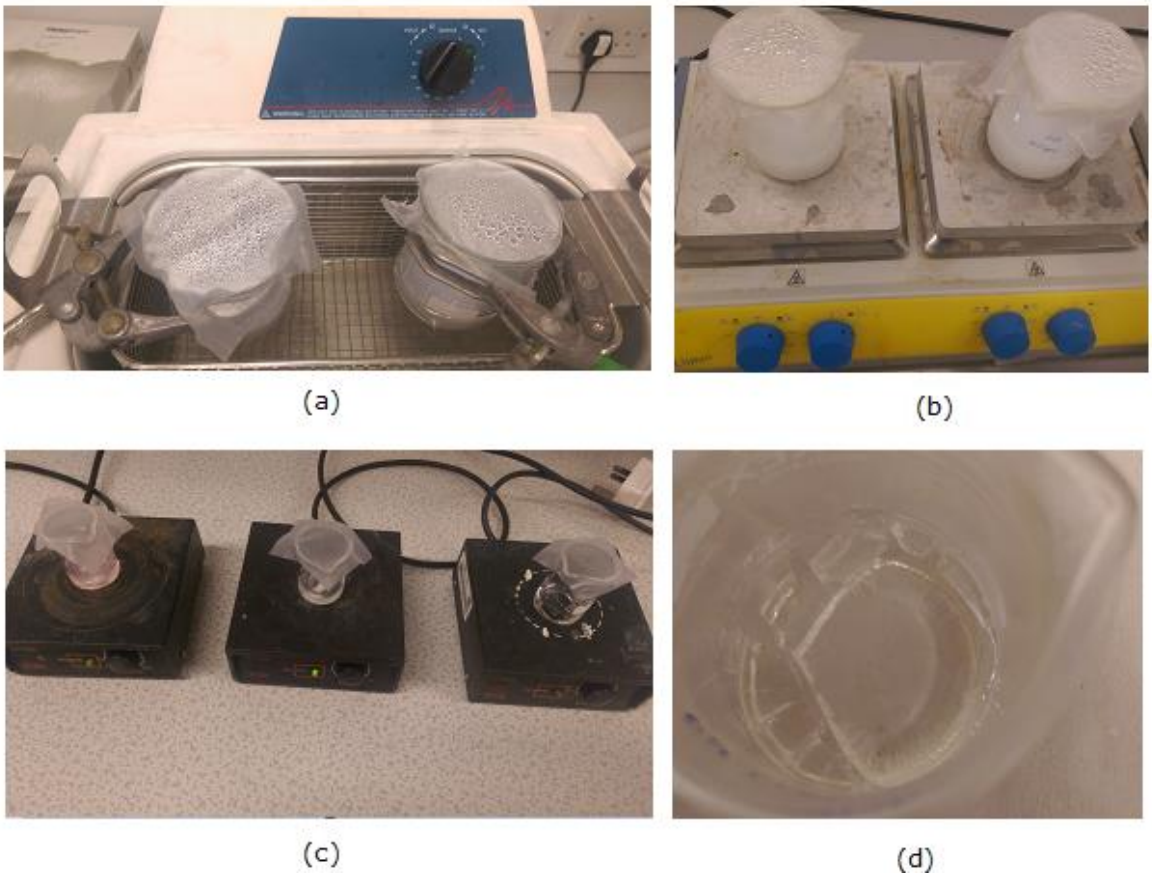

Figure 6.4: Image of: (a) sonication process, (b) magnetic stirring of sol, (c) dissolving rare earth salts using the magnetic stirrer and (d) sol-gel formed after the aging process

In addition to the rare earth doped glass samples synthesised using melt-quench technique (discussed in the Chapter 5), additional samples were synthesised using sol-gel technique for Raman spectroscopic analysis. The samples were synthesised using the two techniques to understand if there are any spectral changes in the Raman signatures of glasses fabricated using low temperature (sol-gel) and high temperature (melt-quench) processes.

The starting solution for the sol-gel synthesis contained: water (15 equiv), 0.01 N HCl (hydrochloric acid), TEOS (tetraethoxysilane – 1 equiv) and Aerosil A-380 (finely dispersed SiO_2 powder - 0.4 equiv). Sonication/ultrasonication was carried out on the solution for 1 hour, which is the act of applying sound energy to agitate the particles in a sample (Figure 6.4 (a)). The solution was then stirred using a magnetic stirrer (Figure 6.4 (b)) and the obtained sol was divided into 4 equal parts. To each of these portions rare earth salt solutions or the rare earth chlorides (2 mol%) dissolved in ethanol (5 ml) was added [13]. The resulting solution was again stirred for an hour for the uniform mixing of the rare earth salts into the sol (Figure 6.4 (c)). Ammonium hydroxide (NH_4OH) was added in to the obtained sol to adjust the pH and quicken the aging/ gelation process [14]. The obtained rare earth doped sol was casted onto small polypropylene dishes and kept for aging for a week. Figure 6.4 (d) shows the obtained sol-gel after the aging process. The obtained sol-gels were sintered by heating the sol-gel glass upto 1000 °C in the Carbolite 1400 high temperature furnace [15].

6.4 Raman spectroscopic studies of rare earth doped glasses

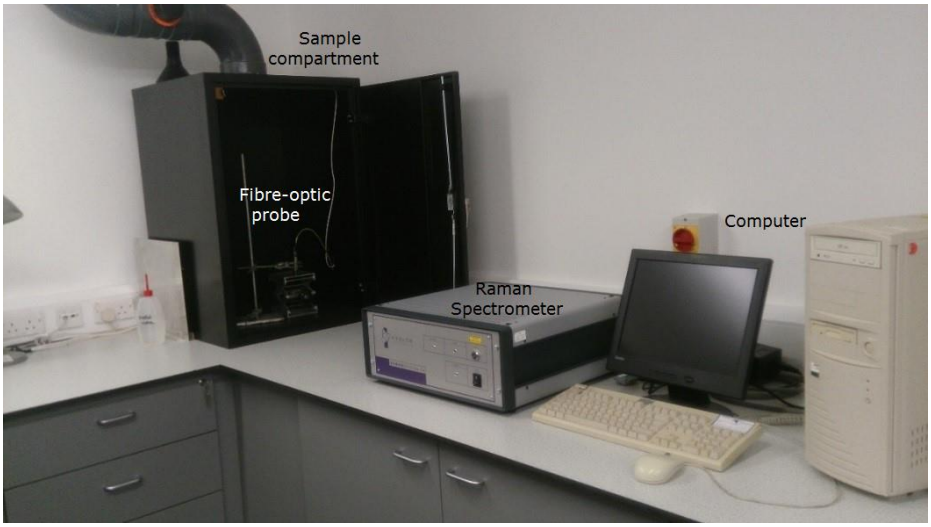

Figure 6.5: Image of the Avalon Raman station and the sample compartment

The fabricated rare earth doped glasses were analysed using the Avalon Instruments Raman Station (R3) which has the 785 nm diode laser used for excitation. As photoluminescence emission and Raman scatterings are two competing processes, the absorption studies carried out in Chapter 5 aided in understanding the non-absorbing wavelengths and thereby select an appropriate laser wavelength for inducing Raman scattering. Depending on laser wavelengths Raman or photoluminescence may or may not happen [16].

6.5 Raman spectroscopy-based temperature studies of rare earth doped glasses

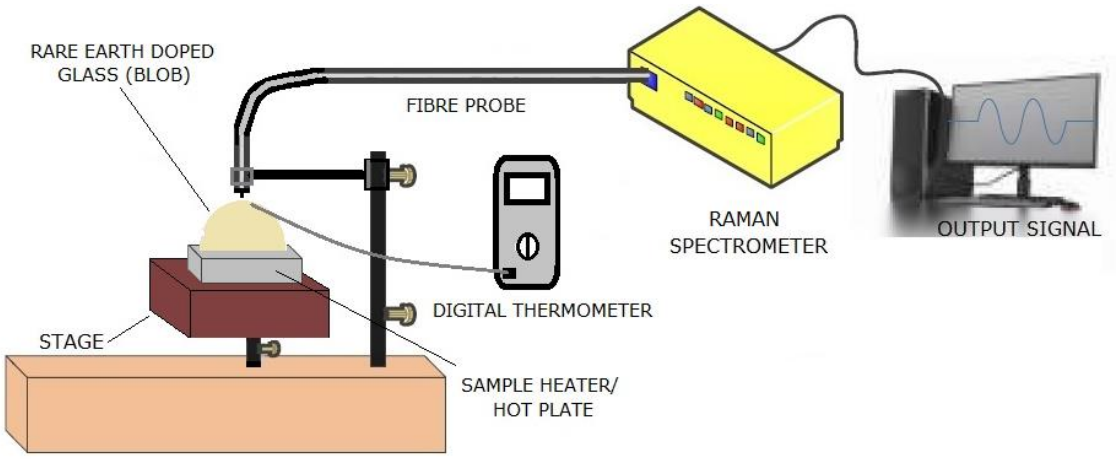

Figure 6.6: Schematic picture of experimental setup used for Raman spectroscopy-based temperature studies of rare earth doped glasses

Figure 6.6 shows the schematic picture of the experimental setup used to study the effect of temperature on Raman signatures of rare earth doped glasses.

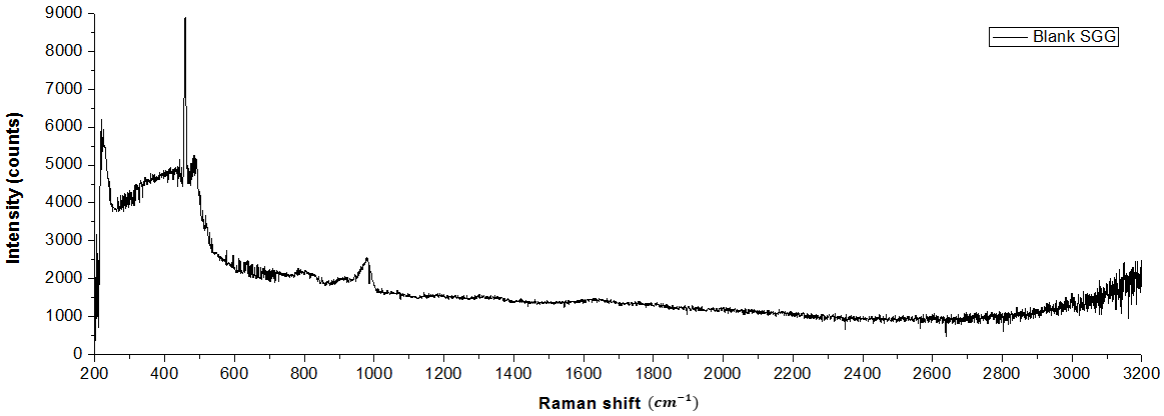

Figure 6.7: Raman spectra of blank SGG for 785 nm laser excitation

Figures 6.7 and 6.8 show the Raman spectra of blank SGG and Tb doped SGG for 785 nm laser excitation. In Figure 6.7, the peaks around 475 cm^{-1} is due to the $Si-O-Si$, $Si-O-B$ isolated vibrations, the small peak around 800 cm^{-1} arises from the boroxol rings and the peak around 950 cm^{-1} is caused by the stretching vibrations of $Si-O$ bond due to the presence of BO_4 unit [17]. The characteristic Raman peak corresponding to $Tb-O$ bond is normally observed in the frequency range 950-980 cm^{-1} [18-20]. Comparing the peaks in Figures 6.7 and 6.8, the Tb Raman characteristic peak around 950 cm^{-1} overlaps with the peak of the blank glass and also the weak band around 1645 cm^{-1} from the borate group becomes more prominent in the Tb doped SGG [19].

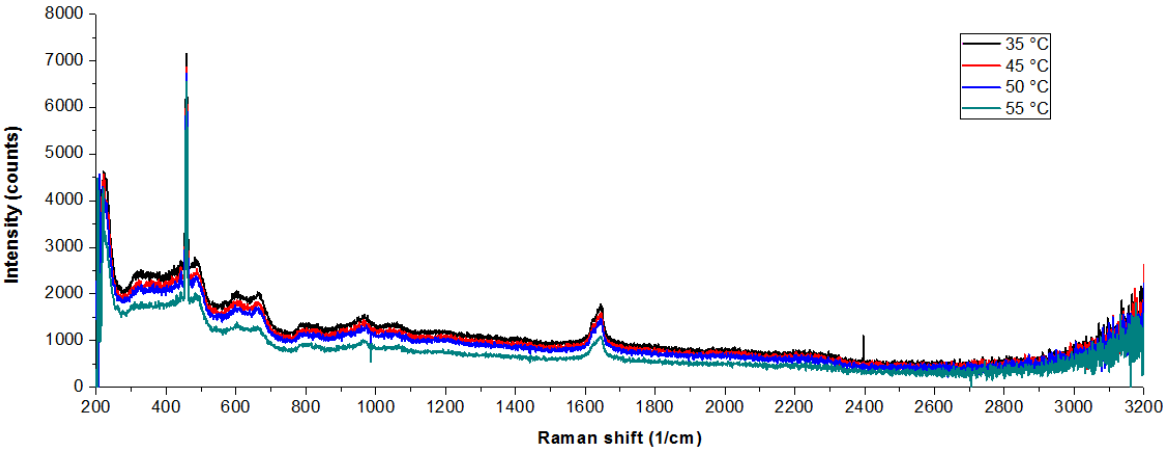

Figure 6.8: Raman spectroscopy-based temperature studies of Tb doped SGG for 785 nm laser excitation

Figure 6.8 also shows the temperature related Raman spectra changes when excited with 785 nm laser. It can be seen that the 1645 cm^{-1} peak observed in the Tb doped SGG sample was temperature sensitive as its Raman intensity was found decreasing with temperature. Figure 6.9 shows the variations in the normalised Raman intensity with respect to temperature, in the range 35-55 °C tracking the peaks 1645 cm^{-1} and 965 cm^{-1}.

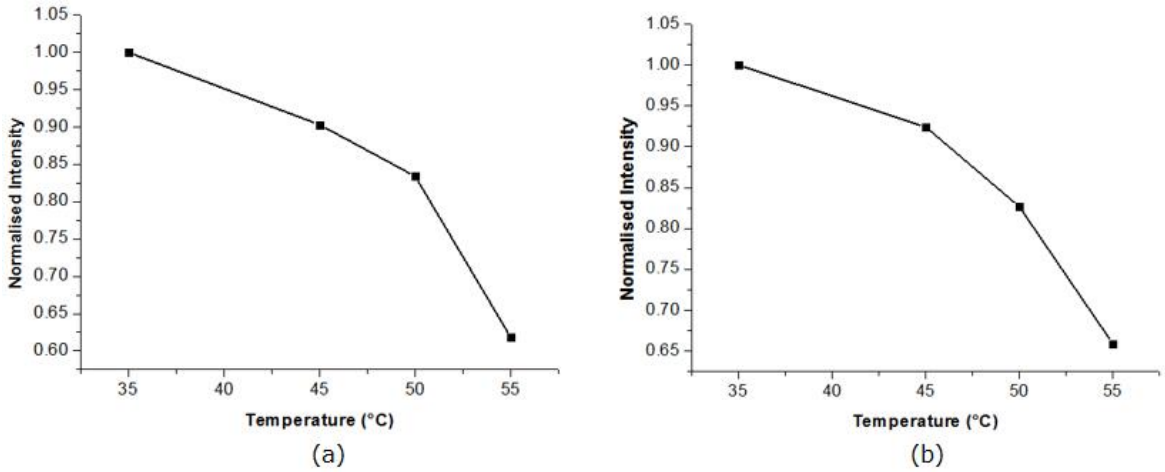

Figure 6.9: Normalised Raman intensity (I_signal/I_max) vs temperature change of Tb doped SGG (a) tracking 1645 cm^{-1}, and (b) tracking 965 cm^{-1}

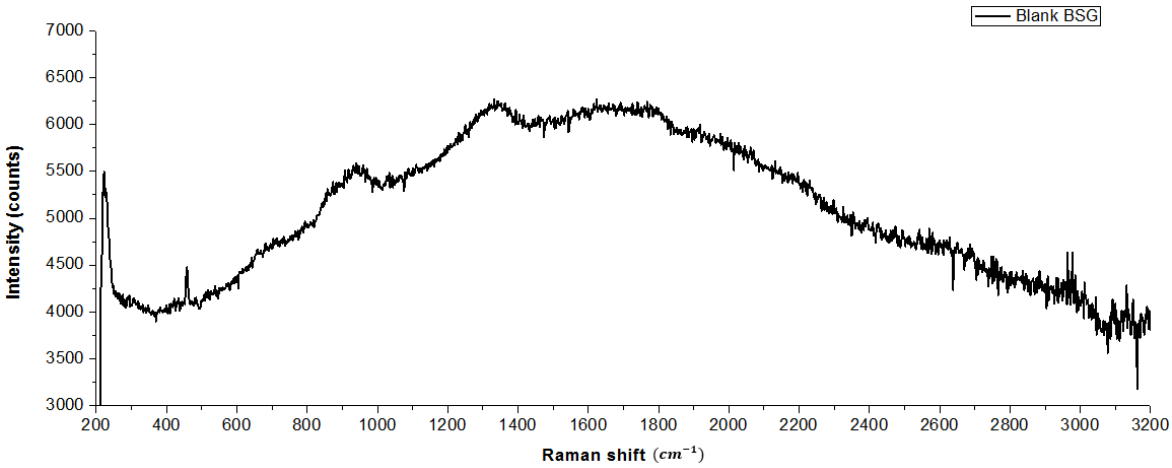

Figure 6.10: Raman spectra of blank BSG for 785 nm laser excitation

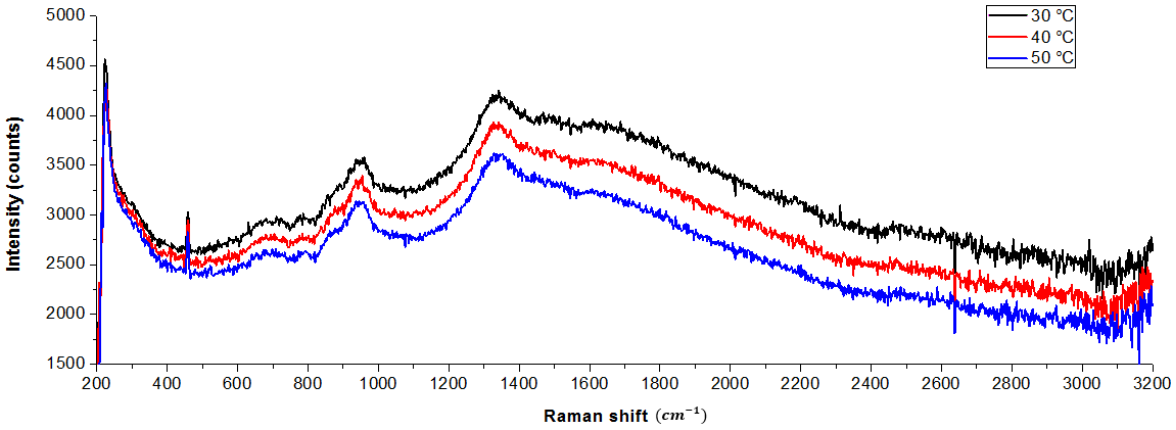

Figure 6.11: Raman spectra of Tb doped BSG corresponding to 785 nm laser excitation for increasing temperatures

Figure 6.10 and 6.11 shows the Raman spectra of blank BSG and Tb doped BSG for 785 nm laser excitation. The peak around 475-487 cm^{-1} arises from the $Si-O-Si, Si-O-B$ isolated vibrations, 947-955 cm^{-1} is due to the stretching vibrations of $Si-O$ bond due to the presence of BO_4 units, 1385-1397 cm^{-1} from the stretching vibrations of $B-O^-$ bond in BO_4 units from different borate groups [17-22]. The characteristic Tb Raman peak was found around 940 cm^{-1}, attributed to the $Tb-O$ bond [18]. Furthermore, with rare earth (Tb) doping the various Raman peaks found in the blank glass were found to get sharper.

Figure 6.11 shows the Raman spectra changes with temperature changes, when excited with 785 nm laser. Tracking the 940 cm^{-1} peak observed in the Tb doped BSG sample, the Raman intensity was found decreasing with temperature. Figure 6.12 shows the variations in the normalised Raman intensity with respect to temperature, in the range 30-50 °C tracking the peak at 940 cm^{-1}.

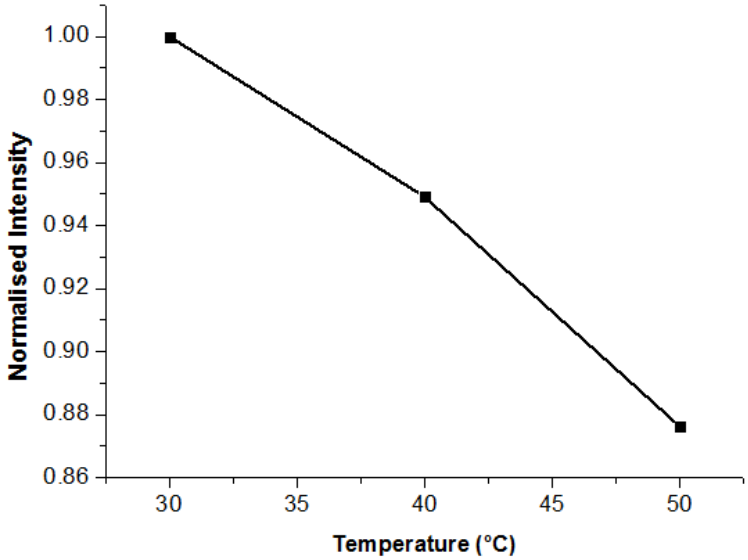

Figure 6.12: Normalised Raman intensity (I_signal/I_max) vs temperature change of Tb doped SGG tracking 940 cm^{-1} peak for increasing temperatures

The repeatability was verified by taking measurements both ways – increasing and decreasing temperatures. From Figures 6.12 and 6.14, it can be observed that the Raman signal intensity follows a linear trend both for increasing and decreasing temperatures. Figure 6.13 shows the Raman intensity variation for decreasing temperatures in the range 50-30 °C.

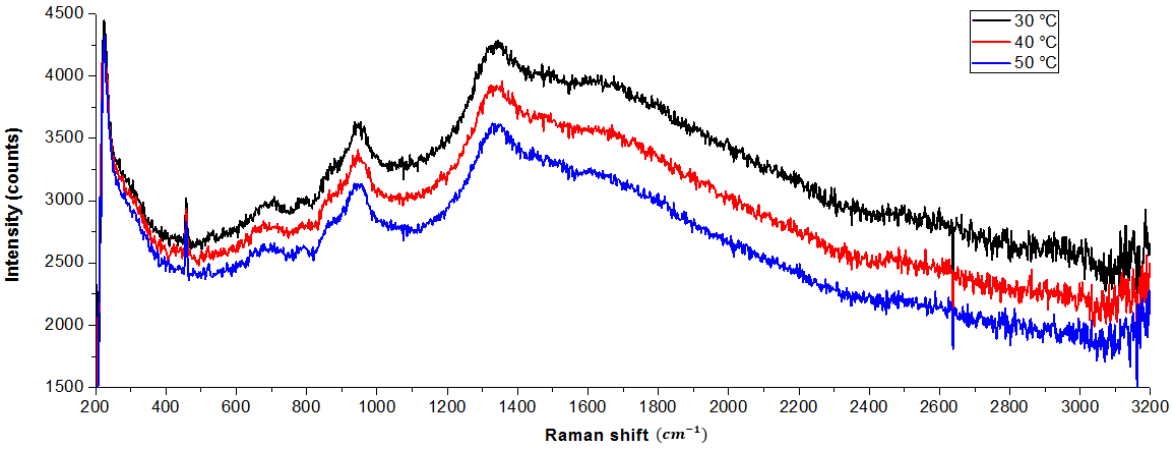

Figure 6.13: Raman spectra of Tb doped BSG corresponding to 785 nm laser excitation for decreasing temperatures

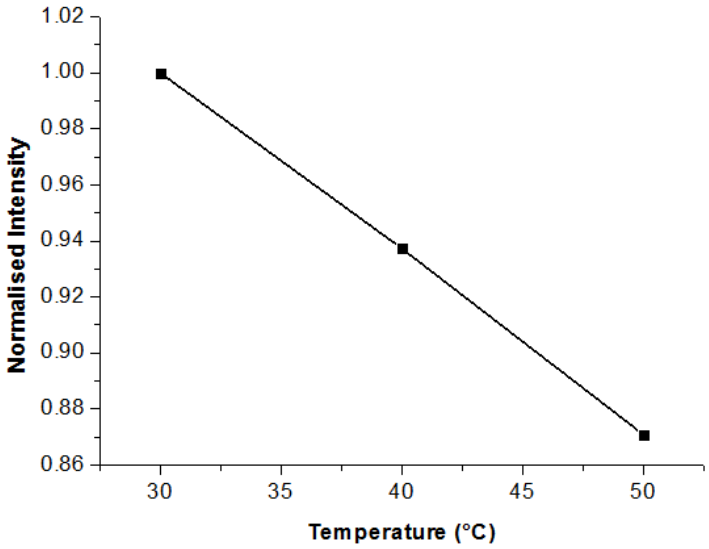

Figure 6.14: Normalised Raman intensity (I_signal/I_max) vs temperature change of Tb doped SGG tracking 940 cm^{-1} peak for decreasing temperatures

Through the Raman spectroscopic investigations carried out, it was identified that the respective Raman signatures were more prominent in rare earth doped SGGs than BSGs. This can be due to temperature differences in the glass making processes. BSG glasses fabricated using the melt-quench technique is a very high temperature process, whereas SGG making is a low temperature process. At higher temperatures, the Raman characteristics or signatures may get reduced. Hence, while analysing the rare earth doped BSGs it was difficult to differentiate the weak Raman signals from the strong background coming from the Raman spectrometer.

6.6 Summary

The investigations carried out in the present chapter identified the possibility of using rare earth doped glass materials for Raman based distributed temperature sensing applications. The Raman spectroscopic studies carried out on different rare earth doped glasses identified that the Raman signal intensity can be enhanced through rare earth doping. Moreover, Raman signal intensity enhancement contributes to the SNR improvement of Raman based DTS

systems. Temperature dependant studies carried out on different rare earth doped glasses identified its suitability for O&G DTS applications. Tb doped glasses depicted more temperature sensitivity compared to other rare earth doped glasses analysed. The sample analysis of rare earth glasses synthesised using the low temperature sol-gel and high temperature melt-quench processes identified that rare earth signatures are more prominent in sol-gel glasses. Hence, the new insights obtained through the different investigations carried out in this chapter can be used for the development of a novel multimodal sensor with improved SNR, enhanced sensitivity and distributed sensing capability. The integrated sensor configuration consisting of rare earth doped PCF-FBG significantly improves the multimodal sensor functionalities exploiting the features of FBG, photoluminescence, Raman and microstructuring.

6.7 References

[1] Amira Z, Bouyahi M, Ezzedine T. Measurement of temperature through Raman scattering. *Procedia Computer Science.* 2015; 73:350-357.

[2] Ukil A, Braendle H, Krippner P. Distributed temperature sensing: review of technology and applications. *IEEE Sensors Journal.* 2012; 12(5):885-892.

[3] Pradhan HS, Sahu PK. *A survey on the performances of distributed fiber-optic sensors. International Conference on Microwave, Optical and Communication Engineering, ICMOCE, IEEE.* 2015; 243-246.

[4] Bao X, Chen L. Recent progress in distributed fiber optic sensors. *Sensors.* 2012; 12(7):8601-8639.

[5] Barrias A, Casas JR, Villalba S. A review of distributed optical fiber sensors for civil engineering applications. *Sensors.* 2016; 16(5):748.

[6] Miah K, Potter D. A review of hybrid fiber-optic distributed simultaneous vibration and temperature sensing technology and its geophysical applications. *Sensors.* 2017; 17(11):2511.

[7] Campanella CE, Ai G, Ukil A. Distributed fiber optics techniques for gas network monitoring. *International Conference on Industrial Technology, ICIT, IEEE.* 2016; 646-651.

[8] Ferraro JR. *Introductory raman spectroscopy.* Academic Press; 2003.

[9] Miah K, Potter D. A review of hybrid fiber-optic distributed simultaneous vibration and temperature sensing technology and its geophysical applications. *Sensors.* 2017; 17(11):2511.

[10] Shen YR, Bloembergen N. Theory of stimulated Brillouin and Raman scattering. *Physical Review.* 1965; 137(6A):A1787.

[11] Singh SP, Gangwar R, Singh N. Nonlinear scattering effects in optical fibers. *Progress In Electromagnetics Research.* 2007; 74:379-405.

[12] De Wolf I, Maes HE, Jones SK. Stress measurements in silicon devices through Raman spectroscopy: bridging the gap between theory and experiment. *Journal of Applied Physics.* 1996 May 1;79(9):7148-56.

[13] Khimich N, Berdichevskii G, Poddenezhnyi E, Golubkov V, Boiko A, Ken'Ko V, et al. Sol-gel synthesis of an optical silica glass doped with rare-earth elements. *Glass Physics and Chemistry.* 2007; 33(2):152-155.

[14] Malashkevich G, Poddenezhny E, Melnichenko I, Boiko A. Optical centers of cerium in silica glasses obtained by the sol-gel process. *Journal of Non-Crystalline Solids.* 1995; 188(1-2):107-117.

[15] Chiodini N, Fasoli M, Martini M, Morazzoni F, Rosetta E, Scotti R, et al. Rare-earth doped sol-gel silicate glasses for scintillator applications. *Radiation Effects and Defects in Solids.* 2003; 158(1-6):463-467.

[16] Alajtal AI. *Raman spectroscopic application for the analysis of organic compounds and minerals of astrobiological significance: the detection and discrimination of organic compounds and mineral analogues in pure and mixed samples of astrobiological significance using raman spectroscopy, XRD and scanning electron microscopy,* Doctoral dissertation, University of Bradford*;* 2010.

[17] Yadav AK, Singh P. A review of the structures of oxide glasses by Raman spectroscopy. *RSC Advances.* 2015; 5(83):67583-67609.

[18] Yung S, Chiang H, Lai Y, Wu F, Fu C, Lee Y. Thermal, optical and structural properties of Tb doped zinc aluminum phosphate glasses. *Ceramics International.* 2015; 41(1):877-888.

[19] Liu Q, Johnston B, Gross S, Withford M, Steel M. A parametric study of laser induced-effects in terbium-doped borosilicate glasses: prospects for compact magneto-optic devices. *Optical Materials Express.* 2013; 3(12):2096-2111.

[20] Elisa M, Sava B, Vasiliu I, Monteiro R, Iordanescu C, Feraru I, et al. Investigations on optical, structural and thermal properties of phosphate glasses containing terbium ions. *IOP Conference Series: Materials Science and Engineering*: IOP Publishing; 2013. p. 012025.

[21] Pucker G, Parolin S, Moser E, Montagna M, Ferrari M, Del Longo L. Raman and luminescence studies of Tb3 doped monolithic silica xerogels. *Spectrochimica Acta Part A: Molecular and Biomolecular Spectroscopy.* 1998; 54(13):2133-2142.

[22] Armellini C, Ferrari M, Montagna M, Pucker G, Bernard C, Monteil A. Terbium (III) doped silica-xerogels: effect of aluminium (III) co-doping. *Journal of Non-Crystalline Solids.* 1999; 245(1-3):115-121.

7. THE PROPOSED MULTIMODAL FIBRE OPTIC SENSOR CONFIGURATION FOR O&G APPLICATIONS

7.1 Introduction

For the condition monitoring of critical parameters like pressure, temperature, vibration, strain, etc., the oil industry is intently looking for multi-point or distributed multimodal sensors. Multimodal sensors provide flexible sensing solutions, enables miniaturisation of the sensors, adds new functionalities with improved measurement capabilities for sensing various important parameters. This chapter will present a novel multimodal fibre optic sensor configuration capable of sensing multiple parameters from different locations. The various investigations carried out in Chapters 3-6 suggests an integrated fibre optic sensor configuration, combining features of LCPCF, FBG and rare earth doping; extracting their molecular, atomic and vibro-rotational characteristics for sensing multiple modalities in the oil industry.

The main limitation of existing fibre optic sensors is they use single wavelength region for probing the parameters. The highlight of the proposed multimodal sensor is that they operate in multiple wavelength regimes, adding scope for new functionalities and sensing capabilities. As discussed in Chapter 3, microstructured fibre improves the light confinement characteristics which in turn enhances the signal intensity from the multimodal sensor configuration. Further investigations carried out revealed that infusing liquid crystals into the PCF sensor aids in tuning of spectral bands from the communication window to NIR and visible wavelengths.

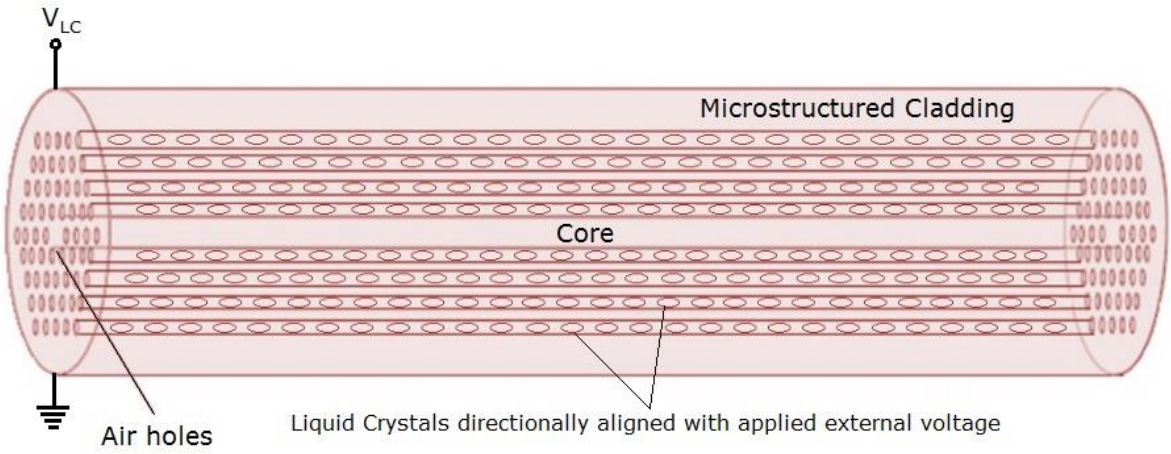

Figure 7.1: LCPCF with applied electrical voltage

Electro chemical change arising in the PCF by infusion of liquid crystals, results in a change in the effective refractive index of cladding and also tunes the optical bandgaps. Both application of electrical voltage for aligning the LC directors (Figure 7.1) and subsequent refractive index changes play a key role in the shift of different spectral bands. Bandgap tuning enables the LCPCF sensor to operate within the photonic bands having peak sensitivities. Liquid crystals can be infiltrated into the PCF holes via capillary effects, a technique known as vacuum assisted LC infiltration is commonly used.

Doping the core of microstructured fibres with rare earth elements further enhances the light confinement characteristics and also invokes photoluminescence and Raman spectroscopic signatures when probed with suitable laser excitations. The specialised features of LCPCF can be effectively utilised in the proposed sensor configuration for tuning the light confinement wavelengths to suit the photoluminescence and Raman spectral regions of the rare earth doped sensors.

Furthermore, integrating FBGs into the sensor configuration enables multi-point multimodal sensing capabilities. The integrated sensor combination is expected to overcome the limitations of existing fibre optic sensors with regards to SNR,

sensing range and multimodal sensing capability. The new sensor configuration operating in multiple wavelength regimes in a multiplexed fashion is capable of multi-parameter sensing.

7.2 Proposed multimodal fibre optic sensor for O&G industry

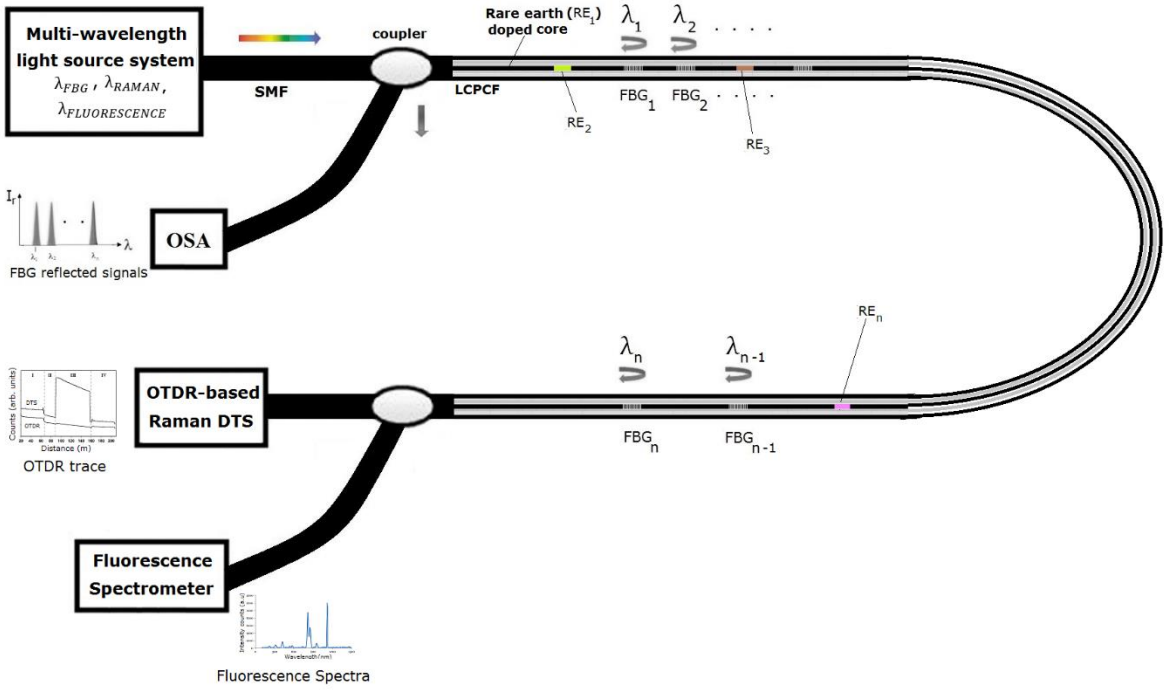

Figure 7.2: Proposed multimodal fibre optic sensor configuration

A multi-wavelength time multiplexed multi-sensing platform is proposed for O&G sensing applications for monitoring different parameters like temperature, strain, chemicals, etc. The proposed multimodal fibre optic sensing system is illustrated in Figure 7.2. In time-division multiplexing (TDM) scheme, the sensors are sequentially addressed by using a pulsed input signal so that the "time of flight" of the optical pulses allows individual sensor signals to be distinguished [1].

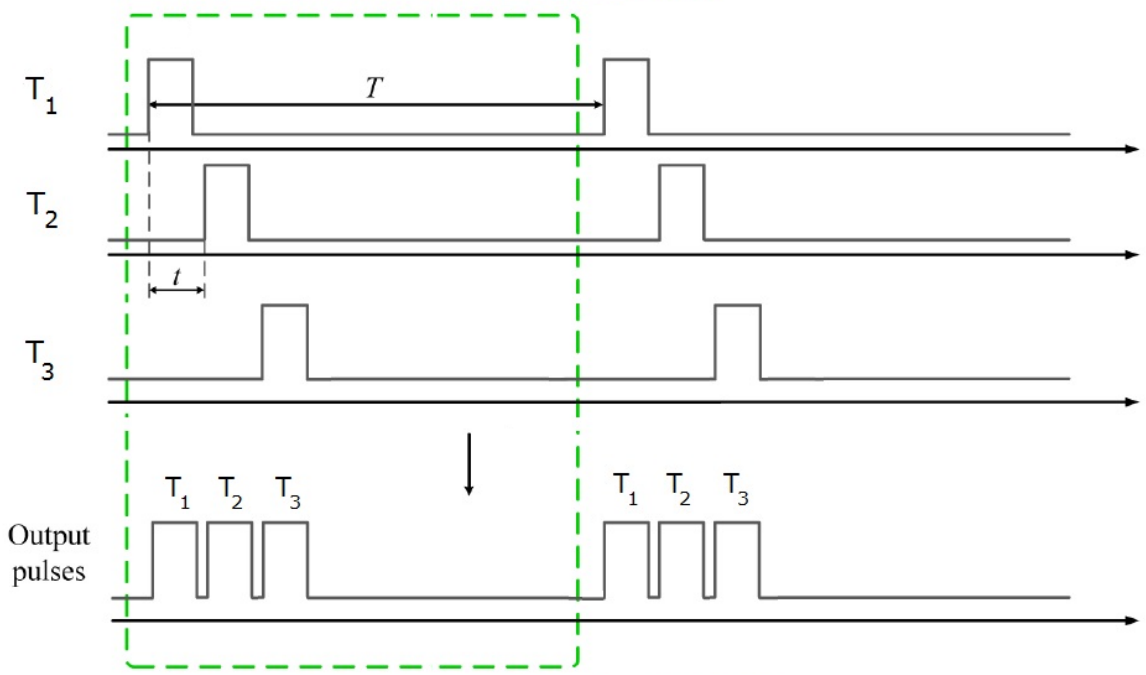

Figure 7.3: Timing diagram

The timing diagram of the pulses in the proposed sensing system is shown in Figure 7.3. A 3-time window TDM array is used, where the term T_i $(i = 1,2\ and\ 3)$ represents the i-th time window. For instance, during the 1st time window (time, T_1) the 1st laser pulse is sampled, and the corresponding sensing information is retrieved. Basically, for each sensing technique (FBG, Raman and photoluminescence) a time slot is assigned for its interrogation or sensing activities to be carried out.

The multimodal sensor is interrogated using different optical pulses having different frequencies or wavelength. The multi-wavelength light source system shown in Figure 7.2, consists of specific laser light sources (for different photoluminescence and Raman excitations wavelengths) and a broad-band source (for the quasi-distributed FBG array) needed for probing the multimodal sensor configuration.

The multimodal fibre optic sensor configuration consists of multi-point or quasi-distributed FBG sensor array $\lambda_1, \lambda_2, \ldots, \lambda_n$ inscribed within the PCF. The quasi-

distributed FBG sensor array can detect strain at multiple points along the oil pipelines. Rare earth element (RE_1) doped within the core of the PCF throughout the length of the sensing fibre aids in Raman based DTS. The rare earth showing maximum temperature sensitivity (Tb) can be chosen for doping the core of the PCF and the Raman signals from the rare earth doped fibres will give higher intensity as well. Localised rare earth doped photoluminescence sensors can be introduced into the silica fibre using diffusion technique [2]. Rare earth doping can be incorporated into silica matrix through a femtosecond (fs) laser generated plasma assisted process [3]. The femtosecond laser ablation and deposition process technique have got additional advantages like enhanced refractive index and photoluminescence intensity [4]. Lumped photoluminescence sensors of different rare earth materials ($RE_2, RE_3, \ldots\ldots, RE_n$) gives different signature peaks and can be utilised for multi-point sensing.

Wideband fibre-optic couplers (2x1 combiners and 1x2 splitters) also known as multimodal couplers can be used for coupling the signals in the fibre optic multimodal sensor system.

At the receiver end, there are different detectors to receive the pulses from the various sensors. The reflected signal from the quasi-distributed FBG sensor array is detected at the OSA or any other suitable interrogator and the shift in centre Bragg wavelength ($\Delta\lambda_B$) is tracked and analysed for detecting any changes in strain value at multiple points.

Two basic techniques for measurement of distributed sensing are Optical Time Domain Reflectometry (OTDR) and Optical Frequency Domain Reflectometry (OFDR). The principle for OTDR is very simple and is like the time of flight measurement used for radar. Normally a narrow laser pulse generated is launched into the fibre and the backscattered signal is analysed. From the time

it takes the backscattered light to return to the detection unit it is possible to locate the location of the temperature event [5]. In OFDR, the system provides information on the measurand only when the backscatter detected during the entire measurement time is measured as a function of frequency in a complex fashion, and then subjected to Fourier transformation [6]. Therefore, OTDR technique is employed in the proposed multimodal sensor configuration and the OTDR trace is a graph plotted between distance from OTDR (or the time as it is directly related to distance) against intensity of the signal. OTDR detects optical events induced by any environmental changes and also locate and measure the events (say temperature change) at any position within the fibre optic sensor link. OTDR uses changes in backscatter light pulses to detect the events [7].

The photoluminescence signals from the lumped rare earth doped sensors can be analysed using a photoluminescence spectrometer. The photoluminescence signature peaks from the different rare earth doped sensors are spectrally spaced, so can be efficiently tracked in the spectrometer for any measurand induced intensity changes.

Furthermore, the loop or double ended configuration of the multimodal sensor configuration reduces the wavelength dependent losses compared to the single ended link [8].

7.3 Investigations on sensor integration

In this section, different fibre optic sensor combinations discussed in the previous chapters are experimentally investigated to understand various aspects of sensor integration for the development of the multimodal sensor configuration.

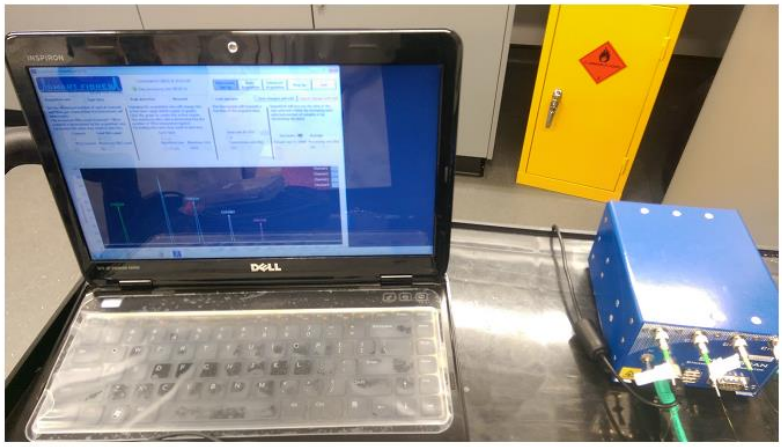

(a)

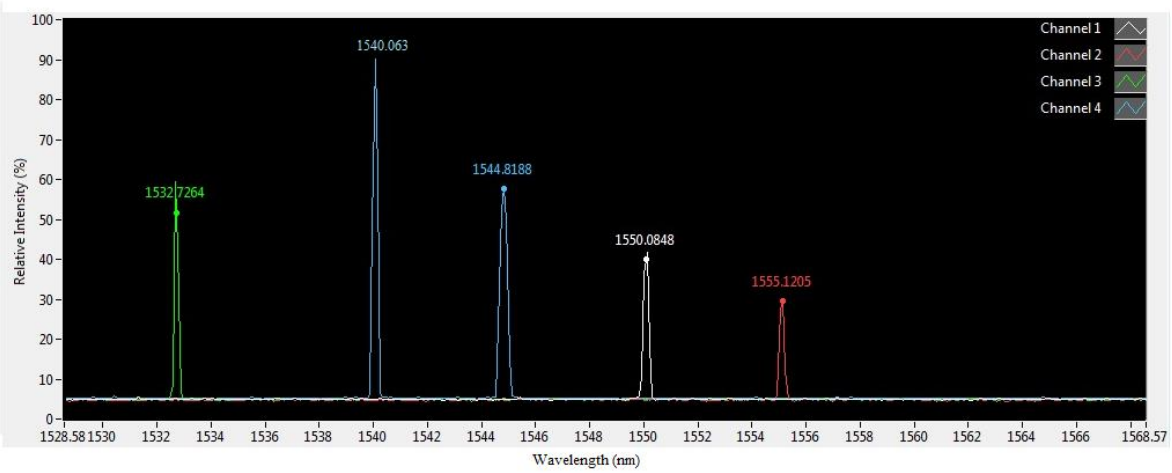

(b)

Figure 7.4: (a) Experimental setup used to evaluate quasi-distributed FBG sensing and (b) FBG reflected spectrum

The reflectivity from a quasi-distributed FBG sensor array consisting of 5 FBGs was analysed using the SmartScan multi-channel FBG interrogator shown in Figure 7.4 (a), having wavelength range 1528-1568 nm. Figure 7.4 (b) shows the obtained FBG reflected signals. The centre wavelengths of the 5 FBGs used for experimentation were around 1532, 1540, 1544, 1550 and 1555 nm respectively. Figure 7.5 shows the reflected spectrum from the quasi-distributed FBG sensor array which can be used for multi-point sensing.

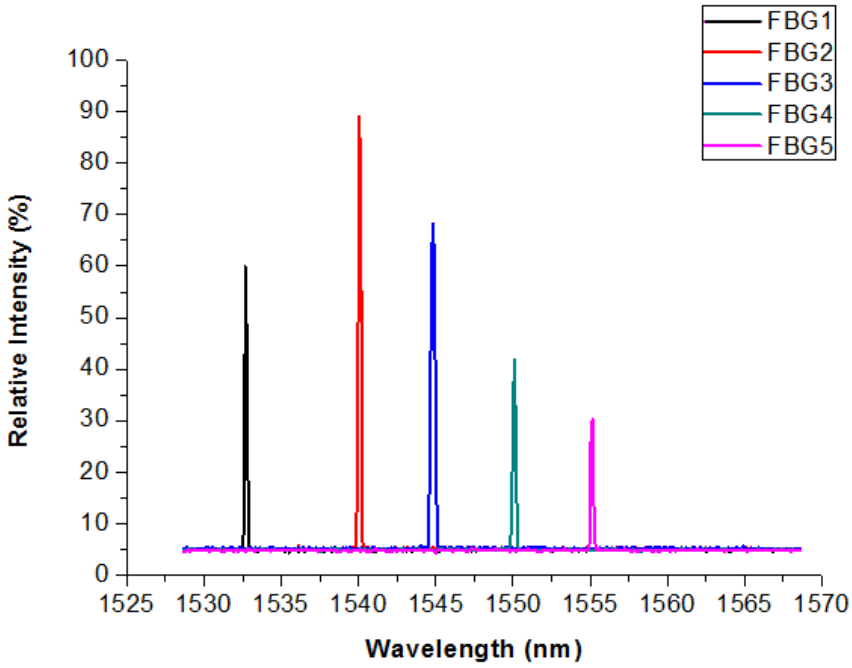

Figure 7.5: Reflected spectrum from the quasi-distributed FBG sensor

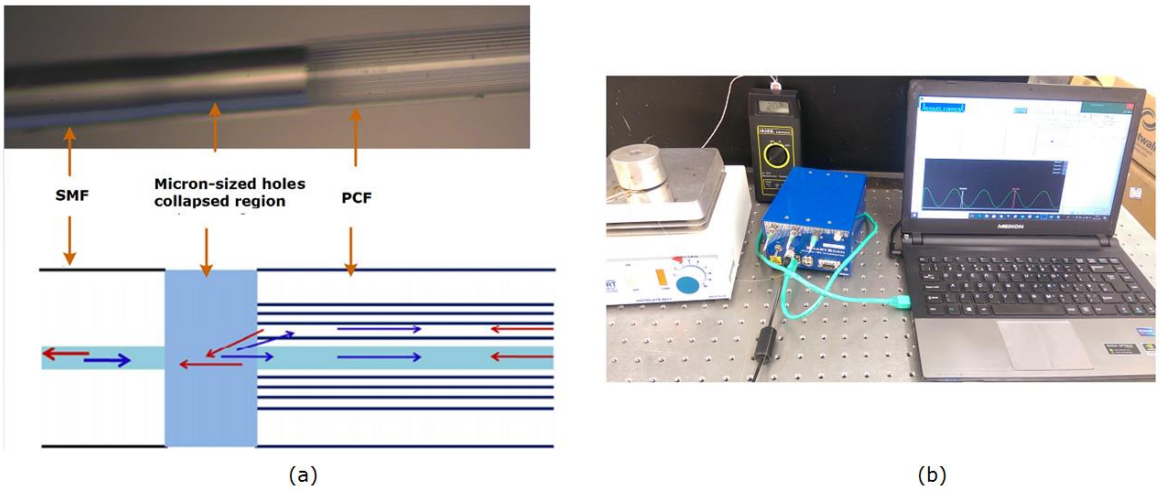

Figure 7.6: (a) Microscopic image of PCF-SMF fused region (along with the principle of modal interference) and (b) experimental setup to evaluate PCF-FBG integrated sensor configuration

Figure 7.6 (a) shows the microscopic image of the spliced PCF-FBG fibre, wherein it can be observed that the splicing has resulted in collapsing of the micron-sized holes resulting in the multimodal spectrum. Figure 7.6 (b) shows the experimental setup used to evaluate the PCF-FBG sensor configuration. Fujikura 70S fibre optic splicers were used for splicing the SMF and PCF. Using the single mode (SM) AUTO and muilti-mode (MM) AUTO options within the

splicing system (shown in Figure 7.7) and optimising the Rearc time, single mode and multimode operation can be realised in the PCF-FBG sensor configuration.

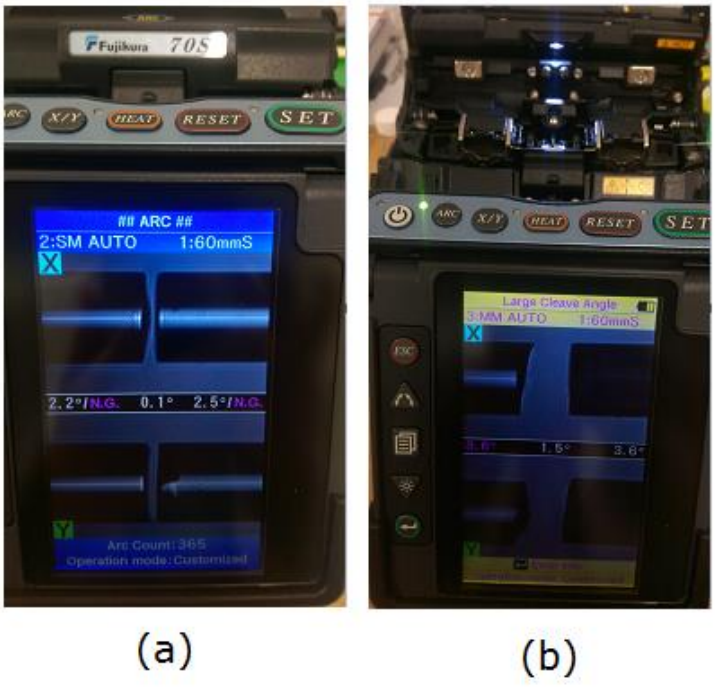

Figure 7.7: (a) SM AUTO splicing operation and (b) MM AUTO splicing operation for PCF-FBG integrated configuration

Figure 7.8 shows the wavelength spectrum obtained from the integrated PCF-FBG sensor configuration from the SmartScan system, giving the FBG peaks from the 2 FBGs within the SMF and the interference spectrum from the PCF-SMF collapsed region.

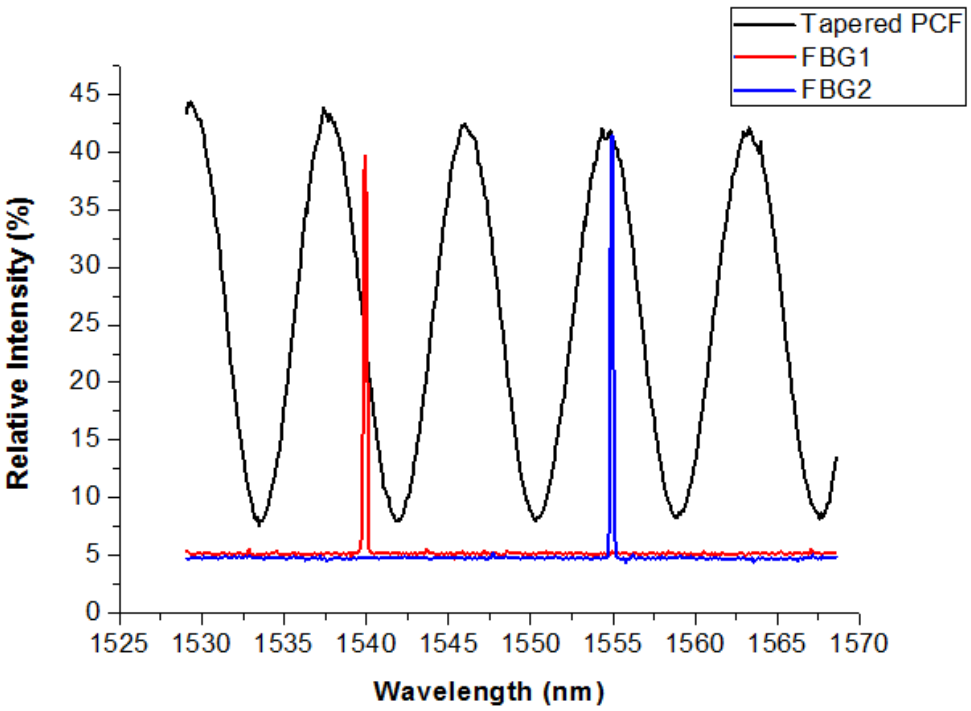

Figure 7.8: Wavelength spectrum from PCF-FBG integrated sensor configuration

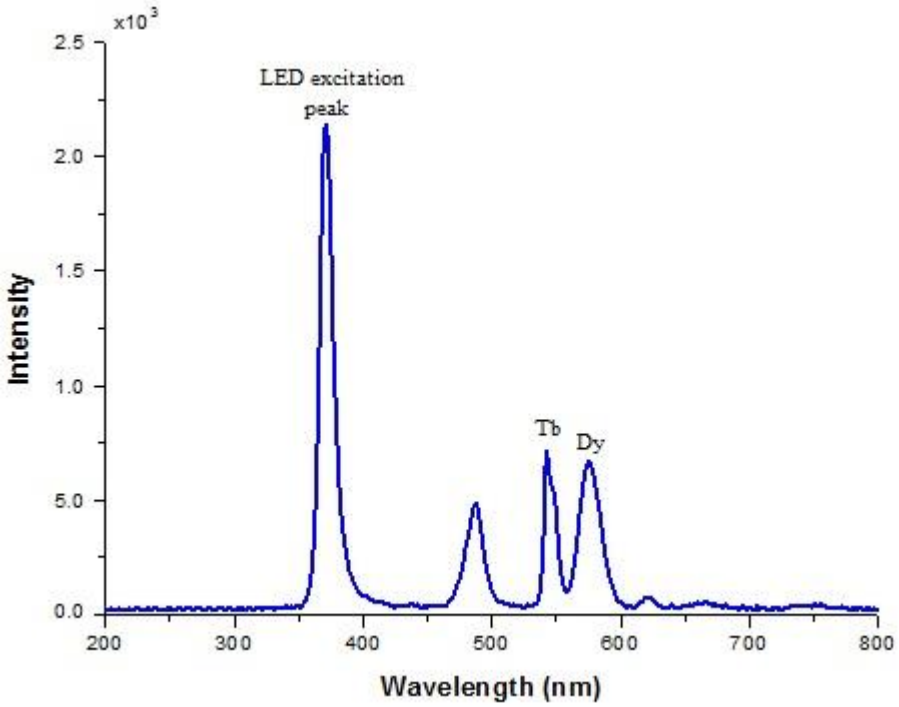

Figure 7.9: Photoluminescence spectrum from Tb-Dy dual waveguide

Figure 7.9 shows the output spectrum obtained from the dual waveguide when irradiated using 385 nm UV LED. 385 nm LED was chosen because, it was identified that both Tb and Dy samples had highest excitation peaks in this

range. As can be observed from the graph, the peak in the 385 nm region corresponds to the LED excitation peak and the peak around 544 nm and 575 nm corresponds to the Tb and Dy signature peaks. The peak around 485 nm is present in both Tb and Dy samples. These results show a strong potential and possibility for multi-point photoluminescence based fibre optic sensors.

7.4 Summary

This chapter discusses about the proposed novel multimodal fibre optic sensor configuration for O&G multi-parameter sensing applications. The proposed multi-wavelength time multiplexed fibre optic sensing systems are capable of multi-point strain sensing, distributed temperature sensing and key point chemical or temperature measurements. Quasi-distributed FBGs with multi-wavelength-based detection enhances the capabilities of the sensor combination, enabling sensing of critical parameter like strain at multiple points. Microstructuring and liquid crystal infiltrations of cladding holes enhances the signal intensity from the sensor configuration and also enables wavelength tunability required for the rare earth-based sensors. Rare earth doping of PCF core further enhances the signal intensity and generates Raman signatures useful for Raman based DTS systems. Furthermore, localised rare earth doping enables multi-point photoluminescence sensing of critical parameters like temperature or chemicals.

7.5 References

[1] Liao Y, Austin E, Nash PJ, Kingsley SA, Richardson DJ. Phase sensitivity characterization in fiber-optic sensor systems using amplifiers and TDM. *Journal of Lightwave Technology.* 2013; 31(10):1645-1653.

[2] Jose G, Fernandez T, Steenson P and Jha A. Multi-ion diffusion in silica glass using femtosecond pulsed laser deposition. *CLEO: Science and Innovations,* Optical Society of America. 2012; 3-6.

[3] Chandrappan J, Murray M, Petrik P, Agocs E, Zolnai Z, Tempez A, et al. Doping silica beyond limits with laser plasma for active photonic materials. *Optical Materials Express.* 2015; 5(12):2849-2861.

[4] Chandrappan J, Murray M, Kakkar T, Petrik P, Agocs E, Zolnai Z, et al. Target dependent femtosecond laser plasma implantation dynamics in enabling silica for high density erbium doping. *Scientific Reports.* 2015; 5:14037.

[5] Schenato L. A review of distributed fibre optic sensors for geo-hydrological applications. *Applied Sciences.* 2017; 7(9):896.

[6] Ghafoori-Shiraz H, Okoshi T. Fault location in optical fibers using optical frequency domain reflectometry. *Journal of Lightwave Technology.* 1986; 4(3):316-322.

[7] Bao X, Chen L. Recent progress in distributed fiber optic sensors. *Sensors.* 2012; 12(7):8601-8639.

[8] Shatarah IS, Olbrycht R. Distributed temperature sensing in optical fibers based on Raman scattering: Theory and applications. *Measurement Automation Monitoring.* 2017; 63.

8. CONCLUSION AND FUTURE SCOPE

8.1 Conclusions

Sensing is a challenging, but vital task in the O&G industry as the explorations are moving into deeper zones. Hence, the oil industry needs reliable multimodal remote sensors for sensing critical down-hole parameters like temperature, pressure, chemicals, etc., and the condition monitoring of their valuable assets and installations. The sensing requirements of O&G industry for improved sensing in deeper zones includes, increased transmission length, improved spatial coverage and integration of multiple sensors with multimodal sensing capability; which imposes problems like signal attenuation, crosstalks and cross sensitivities. Current O&G sensing techniques which are mostly based on electrical sensors, have got limited capability to operate efficiently in extreme environmental conditions like ultra-high temperatures and pressures. The signals from traditional electrical sensors are affected by electromagnetic interference (EMI) in harsh environmental conditions, which deteriorates the performance of the sensor. Compared to electrical sensors, fibre optic sensors offer superior performance, making them the best sensing solution for in-well applications.

A new multimodal fibre optic sensing methodology has been identified through the literature review carried out, which suits different sensing requirements of oil industry. Various computational and experimental investigations have been carried out to understand the feasibility of the identified methodology for long distance, multi-point, multi-parameter sensing.

Mathematical modelling and simulation of the new fibre optic sensor configuration have been carried out to investigate the influence of various core-

cladding structural modifications, liquid crystal material infiltrations and rare earth material doping, to increase the signal intensity from the multimodal sensor configuration for the improvement of overall SNR. COMSOL Multiphysics simulations indicated that structural and material modifications of the PCF have got significant effects on waveguide light propagation characteristics like confinement wavelengths, leakage losses, etc. Theoretical studies carried out using MATLAB software helped in understanding the FBG reflectivity-bandwidth characteristics, for tuning the number of sensors that can be accommodated within the same sensing fibre and enhancing the reflected signal for improved SNR. Experimental studies carried out identified a new approach of FBG sensor positioning, to improve its strain sensitivity for structural health monitoring (SHM) of O&G structures.

Different rare earth doped glass materials (Tb, Dy, Yb, Er, Ce and Ho) have been fabricated and characterised to examine its suitability for O&G multimodal sensing applications. The effect of different doping concentrations and different source excitations have been studied to understand its influence on the photoluminescence signal. It was identified that photoluminescence signal intensity enhances with rare earth concentration up to an optimum value and it can be further improved by choosing an excitation source matching its maximum absorption. Photoluminescence temperature studies carried out on the rare earth doped glasses identified its suitability for O&G high temperature field conditions.

Raman spectroscopic investigations carried out on the fabricated rare earth doped glasses identified its suitability for O&G distributed fibre optic temperature sensing. Furthermore, it was also observed that Raman and photoluminescence

signal intensity enhances with rare earth doping, which may contribute to the SNR of the multimodal fibre optic sensor.

The proposed multimodal fibre optic sensor consisting of rare earth doped PCF-FBG configuration, operating in multiple wavelength regimes in a multiplexed fashion, is capable of overcoming the limitations of existing sensors with regards to SNR, sensing range and multi-parameter sensing capability.

8.2 Future scope

The investigations reported in this thesis on the development of a novel multimodal fibre optic sensor, opens-up many new future research work possibilities. The different technologies utilised in the proposed multimodal sensor configuration like rare earth doping must be further investigated, to take advantage of its other in-built properties. The amplification capabilities of rare earths need to be studied, for long distance O&G remote sensing applications.

The possibility of doping multiple rare earths at the same location of the optical fibre needs to be evaluated. Fabrication of multi-doped rare earth sensors using new doping techniques like diffusion of rare earth ions, needs to be investigated for multimodal sensing. Fabrication of the new rare earth doped specialised PCF and the experimental study of the integrated multimodal sensor configuration must be carried out.

Further Raman spectroscopic investigations on the Raman signal intensity and temperature sensitivity need to be carried out using different laser excitations on the melt-quench glasses. Photoluminescence studies of the melt quench glass corresponding to different excitations and also lifetime investigations need to be carried out. Integration of photoluminescence lifetime techniques within

the proposed multimodal fibre optic sensor configuration, further enhances its SNR owing to its automatic background reduction capabilities.

Demonstration of sensing various physical parameters using the new sensor system needs to be investigated. Further studies need to be carried out on the data-driven Artificial Intelligence (AI) based approaches, to utilise it for noise reduction of the high volume O&G sensing data.

APPENDIX

I. Finite Element Model (FEM)

The FEM, also referred to as finite element analysis is a numerical technique for finding approximate solutions of Partial Differential Equations (PDE) as well as of integral equations.

The underlying methodology of FEM is that a complicated domain can be sub-divided into a series of smaller regions in which the differential equations are approximately solved.

The analysis of the modeled optical fibre/waveguide is based on Maxwell's equations, which governs the wave propagation in the PCF [1].

$$\nabla \times E = -\frac{\partial B}{\partial t}$$

$$\nabla \times H = J + \frac{\partial D}{\partial t}$$

$$\nabla \cdot B = 0$$

$$\nabla \cdot D = \rho$$

where E and H are the electric field and magnetic field strength respectively, D and B are the electric and magnetic flux densities respectively, J is the current density and ρ is the charge density. $J = 0$ and $\rho = 0$ as only non-magnetic, non-conductive materials are considered.

II. FBG reflectivity curve shift with micro-displacement strain

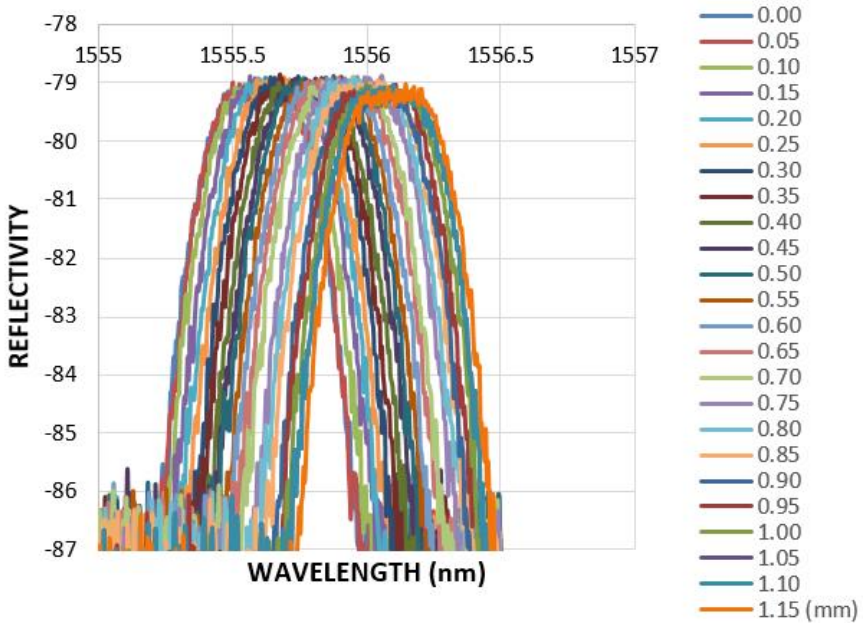

III. Stress Strain relations of Cantilever Beam

For a cantilever beam [2],

$$\text{Stress, } \boldsymbol{\sigma} = \frac{\boldsymbol{F}}{\boldsymbol{A}}$$

where, F is axial force and A is the cross sectional area.

$$\text{Strain, } \varepsilon = \frac{\Delta L}{L}$$

where, $\Delta \boldsymbol{L}$ is the change in length and $\boldsymbol{L}$ is the original length.

Bending stress (MPa) is given by the equation is [2]:

$$\boldsymbol{\sigma} = \frac{\boldsymbol{My}}{\boldsymbol{I}}$$

where, M is the calculated bending moment (N/m), y is the vertical distance away from neutral axis (m), I is the moment of inertia around neutral axis (m^4).

Young's Modulus (E) is the ratio of stress and strain. It is known as the limit of proportionality for a material and is a constant value.

$$E = \frac{\sigma}{\varepsilon} = \frac{\frac{F}{A}}{\frac{\Delta L}{L}}$$

In conclusion, stress is proportional to load and strain is proportional to deformation.

The second moment of area (I) is the measure of a beam's: stiffness with respect to the cross section and its ability to resist bending.

For a solid rectangular cross section, I is given by [2],

$$I = \frac{bh^3}{12}$$

where, b is the breadth of cross sectional area (m) and h is the height of cross sectional area (m).

The deflection of a cantilever beam at a specific point of application of force is given by [3]:

$$\delta = \frac{FL^3}{3EI}$$

where, δ is the deflection (mm), F is applied force (N), L is length of the beam, E is the Young's Modulus (MPa) and I is the second moment of area (m^4).

IV. Theoretical Analysis of Cantilever Beam

Strain analysis of different cantilever beams under applied load was carried out. This work was carried out as a part of student project and the cantilever theoretical investigations was performed by Jade Summer under my supervision [4]. The strain was calculated at various positions along the 300 mm cantilever beams of different shapes. The load was applied by 2 mm displacement at the

free end of the cantilever. Figure A shows the strain at various positions along the beam (where 0 mm represents the free end) for different cantilever beam shapes such as circular, I-beam, T-beam, rectangular and square. All the beam shapes show higher strain at the fixed end. The strain experienced by applied load was maximum for T shape and lowest for the rectangular shape. The obtained results further depend on the type of material and dimensions. All the cantilever beams used to analyse strain effect of different shapes were made of Stainless Steel.

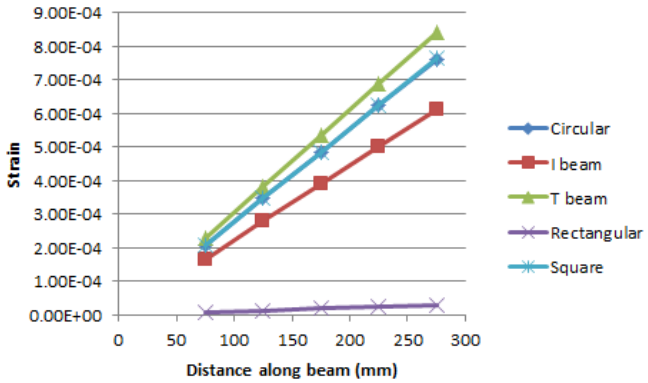

Figure A: Strain at various positions along the beam for different cantilever shapes.

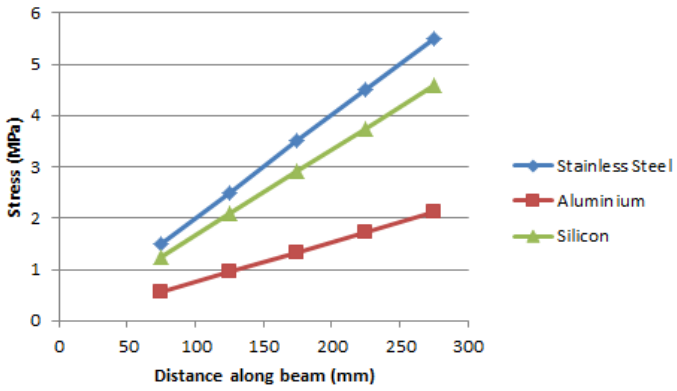

Figure B: Stress at various position on a rectangular cantilever beam for different materials.

Further, the effect of material was investigated on the same rectangular cantilever beam. Stainless steel, aluminium and silicon materials were used to analyse the stress at various positions along the beam caused by the applied

force (2 mm displacement) as shown in Figure B. The higher stress value observed for the stainless steel can be attributed to high Young's modulus. All the three cantilever beams have shown the high-stress value at the fixed end of the cantilever.

Effect of varying the beam thickness was investigated for the same stainless steel rectangular cantilever beam. The thickness of the rectangular beam was increased from 1 mm to 4 mm which leads to increase in the strain at all the positions along the beam as shown in Figure C. The observed increase can be attributed to the increase in the second moment of area due to increased cross section value.

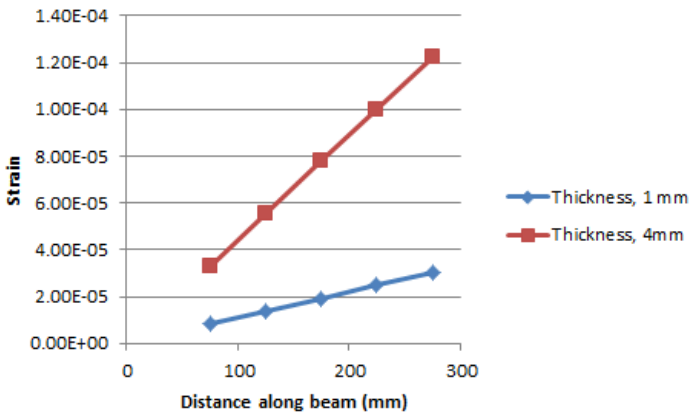

Figure C: Strain at various positions along the rectangular cantilever beam

Effect of application of force at different positions were investigated and the strain was measured along the rectangular cantilever beam corresponding to each position. The force was applied by 2 mm displacement at 50 mm interval along the length starting from 300 mm (free end). The strain measured was increased as the position of the applied force was moved towards the fixed end. The strain was increased gradually closer to the fixed end while a small increase was observed at the free end, as shown in Figure D. When the applied displacement was 50 mm and 100 mm away from the fixed end, strain values

close to the fixed end increased considerably compared to other strain results. These observed high strain values might be the result of slight deformation experienced by the material.

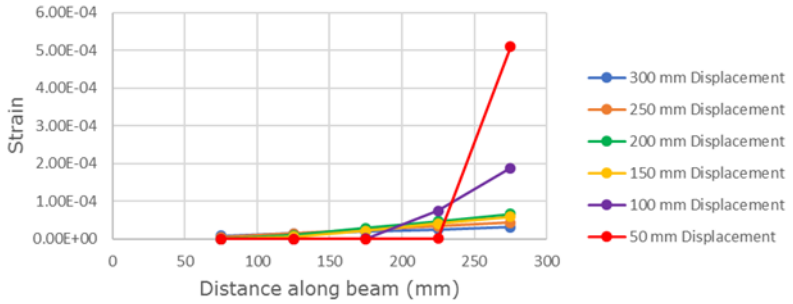

Figure D: Strain along the rectangular cantilever beam for the displacement applied at different positions

V. References

[1] Franco MA, Hattori HT, Sircilli F, Passaro A, Abe NM. Finite element analysis of photonic crystal fibers. Proceedings of the 2001 SBMO/IEEE MTT-S International Microwave and Optoelectronics Conference. 2001; 1:5-7.

[2] Bansal R. *A textbook of strength of materials.* : Laxmi Publications; 2010.

[3] Zhang Y, Ren Q, Zhao Y. Modelling analysis of surface stress on a rectangular cantilever beam. *Journal of Physics D: Applied Physics.* 2004; 37(15):2140.

[4] Johny J, Summers J, Bhavsar K, Joseph GP, Fung WK and Prabhu R. Theoretical investigation of positional influence of FBG sensors for structural health monitoring of offshore structures. *OCEANS 2017-Aberdeen*: IEEE. 2017; 1-5.